



# The Konus-Wind Catalog of Gamma-Ray Bursts with Known Redshifts. I. Bursts Detected in the Triggered Mode

A. Tsvetkova<sup>1</sup> , D. Frederiks<sup>1</sup> , S. Golenetskii<sup>1</sup>, A. Lysenko<sup>1</sup> , P. Oleynik<sup>1</sup>, V. Pal'shin<sup>2</sup>, D. Svinkin<sup>1</sup> , M. Ulanov<sup>1</sup> ,  
T. Cline<sup>3,5</sup>, K. Hurley<sup>4</sup> , and R. Aptekar<sup>1</sup>

<sup>1</sup> Ioffe Institute, Politekhnicheskaya 26, St. Petersburg 194021, Russia; [tsvetkova@mail.ioffe.ru](mailto:tsvetkova@mail.ioffe.ru)

<sup>2</sup> Vedeneva 2-31, St. Petersburg, Russia

<sup>3</sup> NASA Goddard Space Flight Center, Greenbelt, MD 20771, USA

<sup>4</sup> Space Sciences Laboratory, University of California, 7 Gauss Way, Berkeley, CA 94720-7450, USA

Received 2017 September 17; revised 2017 October 11; accepted 2017 October 17; published 2017 November 28

## Abstract

In this catalog, we present the results of a systematic study of gamma-ray bursts (GRBs) with reliable redshift estimates detected in the triggered mode of the Konus-Wind (KW) experiment during the period from 1997 February to 2016 June. The sample consists of 150 GRBs (including 12 short/hard bursts) and represents the largest set of cosmological GRBs studied to date over a broad energy band. From the temporal and spectral analyses of the sample, we provide the burst durations, the spectral lags, the results of spectral fits with two model functions, the total energy fluences, and the peak energy fluxes. Based on the GRB redshifts, which span the range  $0.1 \leq z \leq 5$ , we estimate the rest-frame, isotropic-equivalent energy, and peak luminosity. For 32 GRBs with reasonably constrained jet breaks, we provide the collimation-corrected values of the energetics. We consider the behavior of the rest-frame GRB parameters in the hardness–duration and hardness–intensity planes, and confirm the “Amati” and “Yonetoku” relations for Type II GRBs. The correction for the jet collimation does not improve these correlations for the KW sample. We discuss the influence of instrumental selection effects on the GRB parameter distributions and estimate the KW GRB detection horizon, which extends to  $z \sim 16.6$ , stressing the importance of GRBs as probes of the early universe. Accounting for the instrumental bias, we estimate the KW GRB luminosity evolution, luminosity and isotropic-energy functions, and the evolution of the GRB formation rate, which are in general agreement with those obtained in previous studies.

**Key words:** catalogs – gamma-ray burst: general – methods: data analysis

**Supporting material:** machine-readable tables

## 1. Introduction

Although decades have passed since the discovery of gamma-ray bursts (GRBs), many aspects of this astrophysical phenomenon remain unknown. The major breakthrough was achieved 20 years ago, when the first redshift was measured for the GRB 970508 (Metzger et al. 1997) and the cosmological nature of GRB sources was firmly established.

GRB redshifts are usually measured from the emission lines, the absorption features of the host galaxies imposed on the afterglow continuum, or photometrically. However, there are other approaches to estimate redshifts, e.g., the “pseudo-redshift” (pseudo- $z$ ) technique based on the spectral properties of GRB prompt high energy emission (Atteia 2003) or searching for a minimum on the intrinsic hydrogen column density versus redshift plane (see, e.g., Ghisellini et al. 1999). Considering only spectroscopic and photometric redshifts there were  $\sim 450$  GRBs with reliably measured redshifts by the middle of 2016. As of 2016, the GRB redshifts fill a range from spectroscopic  $z = 0.0087$  (GRB 980425; Foley et al. 2006) to photometric  $z = 9.4$  (GRB 090429B; Cucchiara et al. 2011) or NIR spectroscopic  $z = 8.1$  (GRB 090423; Salvaterra et al. 2009); however, they are expected to occur and be detectable out to redshifts greater than  $z \approx 10$  and possibly up to  $z \approx 15$ –20 (Lamb & Reichart 2001).

The explosion energetics is one of the key parameters for understanding the GRB progenitors and the GRB central

engine physics. Knowing a GRB redshift one can estimate the isotropic equivalent gamma-ray energy ( $E_{\text{iso}}$ ) as a substitute for the energy released by the central engine. Huge isotropic energy releases up to  $E_{\text{iso}} \lesssim 10^{55}$  erg (e.g., GRB 080916C has  $E_{\text{iso}} = 8.8 \times 10^{54}$  erg at  $z = 4.35$ ; Abdo et al. 2009; Greiner et al. 2009) were first explained for the GRB 970508 (Waxman et al. 1998) by taking into account jet beaming: correction for the jet collimation decreases the energy release and peak luminosity of GRBs by orders of magnitude. The hypothesis that GRBs are non-spherical explosions implies that, when the tightly collimated relativistic fireball is decelerated by the circumburst medium (CBM) down to the Lorentz factor  $\Gamma \sim 1/\theta_{\text{jet}}$  (where  $\theta_{\text{jet}}$  is the jet opening angle), an achromatic break (jet break) should appear, in the form of a sudden steepening in the GRB afterglow light curve, at a characteristic time  $t_{\text{jet}}$ . Knowing  $t_{\text{jet}}$ , the jet opening angle can be estimated (Rhoads 1997; Sari et al. 1999) and the collimation-corrected GRB energy calculated. With typical collimation angles of a few degrees, the true energy release from most GRBs is  $\sim 10^{51}$  erg, on par with that of a supernova (Frail et al. 2001).

The Konus-Wind (hereafter KW; Aptekar et al. 1995) experiment has operated since 1994 November and plays an important role in the GRB studies thanks to its unique set of characteristics: the spacecraft orbits in interplanetary space that provides an exceptionally stable background and continuous coverage of the full sky by two omnidirectional NaI detectors, high temporal resolution, and the wide energy range of the detectors ( $\sim 10$  keV–10 MeV, nominally). KW has

<sup>5</sup> Emeritus.

triggered  $\sim 4350$  times on a variety of transient events, including  $\sim 2700$  GRBs, up to 2016 June; thus KW has been detecting GRBs at a rate of  $\sim 120$  events per year. Being a part of the Interplanetary Network (IPN), KW is enabling GRB localizations to be constrained by triangulation (see, e.g., Pal’shin et al. 2013 and Hurley et al. 2013 for details).

Thanks to the wide energy range, the GRB spectral cutoff energy (parameterized as  $E_p$ , the maximum of  $EF_E$  spectrum) can be derived directly from the KW data and the GRB energetics can be estimated using fewer extrapolations. Coupled with well-measured redshifts, the accurate estimates of these parameters provide an excellent testing ground for widely discussed correlations between rest-frame spectral hardness and energetics, e.g., the “Amati” (Amati et al. 2002), “Yonetoku” (Yonetoku et al. 2004) or “Ghirlanda” (Ghirlanda et al. 2004) relations. This could facilitate using GRBs as standard candles (see, e.g., Atteia 1997 or Friedman & Bloom 2005) and probing cosmological parameters with GRBs (see, e.g., Cohen & Piran 1997 or Diaferio et al. 2011).

Here, we present a complete sample of GRBs with reliably measured redshifts that triggered KW from 1997 February to 2016 June. The sample consists of 150 bursts and represents the largest set of GRBs with known redshifts detected by a single instrument over a wide energy range. The KW bursts observed in the waiting mode will be presented in a forthcoming catalog (A. Tsvetkova et al. 2017, in preparation). We start this catalog with a brief description of the KW instrument in Section 2. The burst sample is described in Section 3. In Section 4 we present the temporal and spectral analyses of the sample, and the derived observer- and rest-frame energetics. In Section 5 we discuss the derived prompt emission parameters, the KW-specific instrumental biases, and the rest-frame properties of the KW GRBs.

All the errors quoted in this catalog are at the 68% confidence level (CL) and are of a statistical nature only. Throughout the paper, we assume the standard  $\Lambda$ CDM model:  $H_0 = 67.3 \text{ km s}^{-1} \text{ Mpc}^{-1}$ ,  $\Omega_\Lambda = 0.685$ , and  $\Omega_M = 0.315$  (Planck Collaboration et al. 2014). We also adopt the conventional notation  $Q_k = Q/10^k$ .

## 2. Instrumentation

KW is a gamma-ray spectrometer designed to study temporal and spectral characteristics of GRBs, solar flares, soft gamma repeater bursts, and other transient phenomena over a wide energy range from 13 keV to 10 MeV, nominally (i.e., at launch; see the end of this section). It consists of two identical omnidirectional NaI(Tl) detectors, mounted on opposite faces of the rotationally stabilized *Wind* spacecraft. One detector (S1) points toward the south ecliptic pole, thereby observing the south ecliptic hemisphere; the other (S2) observes the north ecliptic hemisphere. Each detector has an effective area of  $\sim 80\text{--}160 \text{ cm}^2$ , depending on the photon energy and incident angle.

In interplanetary space far outside the Earth’s magnetosphere, KW has the advantages over Earth-orbiting GRB monitors of continuous coverage, uninterrupted by Earth occultation, and a steady background, undistorted by passages through Earth’s trapped radiation, and subject only to occasional solar particle events. The *Wind* distance from Earth as a function of time is presented in Pal’shin et al. (2013); it ranges up to 5.5 lt-s.

The instrument has two operational modes: waiting and triggered. While in the waiting mode, the count rates are recorded in three energy windows G1 (13–50 keV), G2 (50–200 keV), and G3 (200–760 keV) with 2.944 s time resolution. When the count rate in the G2 window exceeds a  $\approx 9\sigma$  threshold above the background on one of two fixed timescales  $\Delta T_{\text{trig}}$ , 1 s or 140 ms, the instrument switches into the triggered mode, for which the waiting-mode data are also available up to  $T_0 + 250$  s. In the triggered mode, the count rates in the three energy windows are recorded with time resolutions varying from 2 ms up to 256 ms. These time histories, with a total duration of  $\sim 230$  s, also include 0.512 s of pre-trigger history. Spectral measurements are carried out, starting from the trigger time  $T_0$ , in two overlapping energy intervals, PHA1 (13–760 keV) and PHA2 (160 keV–10 MeV), with 64 spectra being recorded for each interval over a 63-channel, pseudo-logarithmic, energy scale. The first four spectra are measured with a fixed accumulation time of 64 ms in order to study short bursts. For the subsequent 52 spectra, an adaptive system determines the accumulation times, which may vary from 0.256 to 8.192 s depending on the current count rate in the G2 window. The last 8 spectra are obtained for 8.192 s each. As a result the minimum duration of spectral measurements is 79.104 s, and the maximum is 491.776 s (which is  $\sim 260$  s longer than the time history duration). After the triggered-mode measurements are finished, KW switches into the data-readout mode for  $\sim 1$  hr and no measurements are available for this time interval.

For all the bursts, we used a standard KW dead time (DT) correction procedure for light curves (with a DT of a few  $\mu\text{s}$ ) and spectra (with a DT of  $\sim 42 \mu\text{s}$ ). The detector response matrix (DRM), which is a function only of the burst angle relative to the instrument axis, was computed using the GEANT4 package (Agostinelli et al. 2003). The detailed description of the instrument response calculation is presented in Terekhov et al. (1998). The latest version of the DRM contains responses calculated for 264 photon energies between 5 keV and 30 MeV on a quasi-logarithmic scale for incident angles from  $0^\circ$  to  $100^\circ$  with a step of  $5^\circ$ . The energy scale is calibrated in flight using the 1460 keV line of  $^{40}\text{K}$  and the 511 keV  $e^+e^-$  annihilation line. The gain of the detectors has slowly decreased during the long period of operation. The instrumental control of the gain became non-functional in 1997 and the spectral range changed to 25 keV–18 MeV for the S1 detector and to 20 keV–15 MeV for the S2 detector, from the original 13 keV–10 MeV; the G1, G2, G3, PHA1, and PHA2 energy bounds shifted accordingly.

The consistency of the KW spectral parameters and those obtained in other GRB experiments was verified by a cross-calibration with *Swift*-BAT and *Suzaku*-WAM (Sakamoto et al. 2011b), and in joint spectral fits with *Fermi*-GBM (e.g., Lipunov et al. 2016). It was shown that the difference in the spectrum normalization between KW and these instruments is  $\lesssim 20\%$  in joint fits. A more detailed discussion of the KW instrumental issues can be found in Svinkin et al. (2016b), hereafter S16.

## 3. The Burst Sample

The sample contains 150 GRBs with reliable redshift estimates detected by KW in the triggered mode from the beginning of the afterglow era in 1997 to the middle of 2016. The general information about these bursts is presented in

**Table 1**  
General Information

Burst Name	Trigger Time	Geocenter Time	Type	Local. instr.	Local. References	Other <sup>c</sup> obs.	Det.	Inc. angle (deg)	z	z type <sup>d</sup>	z References
GRB 970228	02:58:01.317	02:58:01.263	II	BeppoSAX	(1)	3	S1	79.1	0.695	s	(2)
GRB 970828	17:44:42.357	17:44:42.157	II	RXTEASM	(3)	...	S2	7.1	0.9578 <sup>a</sup>	s	(4)
GRB 971214	23:20:52.214	23:20:51.043	II	BeppoSAX	(1)	1 3	S2	33.9	3.418	s	(5)
GRB 990123	09:47:14.151	09:47:15.040	II	BeppoSAX	(1)	1 3	S2	29.9	1.6004	s	(6)
GRB 990506	11:23:30.813	11:23:31.274	II	BeppoSAX	(1)	1 3	S1	65.1	1.30658 <sup>a</sup>	s	(7)
GRB 990510	08:49:10.059	08:49:10.052	II	BeppoSAX	(1)	1 3	S1	28.7	1.6187	s	(8)
GRB 990705	16:01:26.864	16:01:26.352	II	BeppoSAX	(1)	3	S1	7.1	0.8424	s	(9)
GRB 990712	16:43:06.123	16:43:03.763	II	BeppoSAX	(1)	3	S1	33.2	0.4331	s	(8)
GRB 991208	04:36:53.263	04:36:53.224	II	IPN	(10)	...	S2	23.0	0.7055	s	(11)
GRB 991216	16:07:18.085	16:07:18.535	II	BeppoSAX	(1)	1 3	S1	78.1	1.02	s	(12)
GRB 000131	14:59:15.102	14:59:14.388	II	IPN	(13)	...	S1	14.7	4.5	s	(14)
GRB 000210	08:44:05.712	08:44:06.695	II	BeppoSAX	(1)	3	S1	41.6	0.8463 <sup>a</sup>	s	(15)
GRB 000301C	09:51:38.569	09:51:37.589	II	IPN+ASM	(16)	...	S2	40.1	2.0335	s	(17)
GRB 000418	09:53:09.906	09:53:08.258	II	IPN	(18)	...	S2	69.1	1.1181	s	(7)
GRB 000911	07:15:25.914	07:15:28.816	II	IPN	(19)	...	S1	84.3	1.0585	s	(20)
GRB 000926	23:49:33.661	23:49:32.447	II	IPN	(21)	...	S2	16.3	2.0369	s	(22)
GRB 010222	07:23:11.652	07:23:12.337	II	BeppoSAX	(1)	3	S2	34.5	1.4768	s	(23)
GRB 010921	05:15:57.151	05:15:56.112	II	BeppoSAX	(1)	2 3	S2	44.6	0.45	s	(24)
GRB 011121	18:47:13.457	18:47:13.448	II	BeppoSAX	(1)	3	S1	25.7	0.36	s	(25)
GRB 020405	00:41:39.501	00:41:37.640	II	BeppoSAX	(1)	3	S1	71.9	0.6898	s	(26)
GRB 020813	02:44:40.651	02:44:40.139	II	HETE-2	(27)	2	S1	91.6	1.254	s	(28)
GRB 020819B <sup>e</sup>	14:57:39.766	14:57:38.125	II	HETE-2	(27)	2	S2	81.0	0.411 <sup>a</sup>	s	(29)
GRB 021211	11:18:35.206	11:18:34.494	II	HETE-2	(30)	2	S1	76.9	1.004	s	(31)
GRB 030329	11:37:29.254	11:37:26.378	II	HETE-2	(27)	2	S2	77.5	0.16854	s	(32)
GRB 040924	11:52:15.280	11:52:12.600	II	HETE-2	(33)	2	S2	87.0	0.859	s	(34)
GRB 041006	12:18:43.030	12:18:39.061	II	HETE-2	(35)	2	S2	94.3	0.716	s	(36)
GRB 050401	14:20:11.344	14:20:09.710	II	SwiftBAT	(37)	4	S2	66.2	2.8992 <sup>b</sup>	s	(38)
GRB 050525A	00:02:56.704	00:02:53.543	II	SwiftBAT	(37)	4	S2	40.5	0.606	s	(39)
GRB 050603	06:29:00.767	06:29:02.176	II	SwiftBAT	(37)	4	S1	51.6	2.821	s	(40)
GRB 050820A <sup>f</sup>	06:39:14.512	06:39:10.966	II	SwiftBAT	(37)	4	S2	63.2	2.6147	s	(41)
GRB 050922C	19:55:54.480	19:55:50.299	II	SwiftBAT	(37)	2 4	S2	82.7	2.198	s	(42)
GRB 051008	16:33:20.762	16:33:23.339	II	SwiftBAT	(37)	4	S2	43.1	2.77 <sup>a</sup> g	p	(43)
GRB 051022	13:08:25.298	13:08:21.749	II	HETE-2	(27)	2	S2	71.7	0.8	s	(44)
GRB 051109A	01:12:22.541	01:12:21.735	II	SwiftBAT	(37)	4	S2	41.5	2.346	s	(45)
GRB 051221A	01:51:12.976	01:51:15.938	I	SwiftBAT	(37)	4	S2	62.3	0.5465	s	(46)
GRB 060121	22:25:00.890	22:24:56.407	II <sup>h</sup>	HETE-2	(47)	2	S2	62.1	4.6 <sup>j</sup>	p	(48)
GRB 060124	16:04:13.894	16:04:10.869	II	SwiftBAT	(37)	4	S2	43.4	2.3000	s	(49)
GRB 060502A	03:03:33.119	03:03:32.793	II	SwiftBAT	(37)	4	S2	11.4	1.5026	s	(49)
GRB 060614	12:43:51.590	12:43:47.332	II <sup>j</sup>	SwiftBAT	(37)	4	S1	54.4	0.1254	s	(50)
GRB 060814	23:02:34.447	23:02:34.295	II	SwiftBAT	(37)	4	S2	55.3	1.9229 <sup>a</sup>	s	(51)
GRB 060912A	13:55:57.788	13:55:54.482	II	SwiftBAT	(37)	4	S2	72.9	0.937	s	(52)
GRB 061006	16:45:26.896	16:45:27.817	I <sup>k</sup>	SwiftBAT	(37)	4	S1	13.9	0.4377	s	(53)
GRB 061007	10:08:09.344	10:08:07.767	II	SwiftBAT	(37)	4	S1	27.0	1.2622	s	(49)
GRB 061021	15:39:08.304	15:39:09.770	II	SwiftBAT	(37)	4	S1	56.4	0.3453	s	(54)
GRB 061121	15:23:32.445	15:23:30.905	II	SwiftBAT	(37)	4	S1	65.2	1.3145	s	(49)
GRB 061201	15:58:34.558	15:58:36.886	I	SwiftBAT	(37)	4	S1	33.4	0.111	s	(55)
GRB 061222A	03:30:14.682	03:30:13.937	II	SwiftBAT	(37)	4	S2	47.6	2.088 <sup>a</sup>	s	(56)
GRB 070125	07:20:50.853	07:20:45.664	II	IPN+BAT	(57)	...	S2	80.0	1.547	s	(58)
GRB 070328	03:53:49.993	03:53:52.064	II	SwiftBAT	(37)	4	S1	35.6	2.0627	s	(54)
GRB 070508	04:18:22.779	04:18:20.346	II	SwiftBAT	(37)	4	S1	32.9	0.82 <sup>b</sup>	s	(59)
GRB 070521	06:51:31.587	06:51:28.779	II	SwiftBAT	(37)	4	S2	39.9	1.7 <sup>a</sup> l	p	(60)
GRB 070714B	04:59:25.178	04:59:29.705	I	SwiftBAT	(37)	4	S1	97.9	0.923	s	(61)
GRB 071003	07:40:55.120	07:40:53.830	II	SwiftBAT	(37)	4	S2	59.6	1.60435	s	(62)
GRB 071010B	20:45:48.490	20:45:49.125	II	SwiftBAT	(37)	4	S2	58.6	0.947	s	(63)
GRB 071020	07:02:26.637	07:02:24.778	II	SwiftBAT	(37)	4	S2	78.0	2.1462	s	(49)
GRB 071112C	18:33:02.583	18:32:58.044	II	SwiftBAT	(64)	4	S1	102.4	0.8227	s	(49)
GRB 071117	14:50:04.535	14:50:06.512	II	SwiftBAT	(37)	4	S1	41.8	1.3308	s	(49)
GRB 071227	20:13:48.722	20:13:47.668	I	SwiftBAT	(37)	4	S1	18.3	0.384	s	(65)
GRB 080319B	06:12:50.339	06:12:47.321	II	SwiftBAT	(37)	4	S2	42.3	0.9382	s	(49)
GRB 080319C	12:25:57.938	12:25:57.035	II	SwiftBAT	(37)	4	S2	12.3	1.9492 <sup>b</sup>	s	(49)
GRB 080411	21:15:32.496	21:15:32.853	II	SwiftBAT	(37)	4	S1	18.6	1.0301	s	(49)
GRB 080413A	02:54:23.605	02:54:21.182	II	SwiftBAT	(37)	4	S2	95.1	2.433	s	(49)
GRB 080413B	08:51:11.831	08:51:12.288	II	SwiftBAT	(37)	4	S2	96.0	1.1014	s	(49)
GRB 080514B	09:55:58.672	09:55:57.137	II	SuperAGILE/IPN	(66)	4	S2	75.4	1.8	p	(67)
GRB 080602	01:31:26.229	01:31:28.289	II	SwiftBAT	(37)	4	S1	74.0	1.8204	s	(54)
GRB 080603B	19:38:12.383	19:38:14.633	II	SwiftBAT	(37)	4	S2	32.6	2.6892	s	(49)
GRB 080605	23:48:02.336	23:47:57.581	II	SwiftBAT	(37)	4	S2	62.8	1.6403 <sup>b</sup>	s	(49)
GRB 080607	06:07:23.336	06:07:22.085	II	SwiftBAT	(37)	4	S2	69.5	3.0363 <sup>b</sup>	s	(68)
GRB 080721	10:25:10.927	10:25:07.575	II	SwiftBAT	(37)	4	S2	85.0	2.591	s	(69)
GRB 080916C	00:12:44.632	00:12:46.223	II	FermiLAT	(70)	5 6	S1	17.1	4.35 <sup>m</sup>	p	(71)
GRB 080916A	09:45:21.715	09:45:19.813	II	SwiftBAT	(37)	4 5	S1	47.0	0.6887	s	(49)

**Table 1**  
(Continued)

Burst Name	Trigger Time	Geocenter Time	Type	Local. instr.	Local. References	Other <sup>c</sup> obs.	Det.	Inc. angle (deg)	z	z type <sup>d</sup>	z References
GRB 081121	20:35:31.435	20:35:30.430	II	SwiftBAT	(37)	4 5	S1	5.9	2.512	s	(72)
GRB 081203A	13:51:30.368	13:51:31.069	II	SwiftBAT	(37)	4	S2	15.6	2.05	s	(73)
GRB 081221	16:21:14.915	16:21:13.479	II	SwiftBAT	(37)	4 5	S1	61.3	2.26	s	(74)
GRB 081222	04:54:02.534	04:54:01.179	II	SwiftBAT	(37)	4 5	S1	50.1	2.77	s	(75)
GRB 090102	02:55:36.283	02:55:32.211	II	SwiftBAT	(37)	4 5	S2	76.2	1.547	s	(76)
GRB 090201	17:47:00.275	17:46:58.787	II	SwiftBAT	(37)	4	S1	20.0	2.1000	s	(54)
GRB 090323	00:02:54.632	00:02:50.491	II	FermiLAT	(70)	5 6	S2	70.1	3.6	s	(77)
GRB 090328	09:36:49.486	09:36:50.556	II	FermiLAT	(70)	5 6	S1	24.6	0.736	s	(78)
GRB 090424	14:12:11.725	14:12:08.925	II	SwiftBAT	(37)	4 5	S2	70.8	0.544	s	(79)
GRB 090510	00:23:01.547	00:23:00.536	I	SwiftBAT	(37)	4 5 6	S1	75.4	0.903	s	(80)
GRB 090618	08:28:24.974	08:28:26.755	II	SwiftBAT	(37)	4 5	S2	13.6	0.54	s	(81)
GRB 090709A	07:38:34.965	07:38:34.873	II	SwiftBAT	(37)	4	S2	10.5	1.8 <sup>a n</sup>	p	(60)
GRB 090715B	21:03:19.008	21:03:18.138	II	SwiftBAT	(37)	4	S2	23.9	3.00	s	(82)
GRB 090812	06:02:38.942	06:02:35.958	II	SwiftBAT	(37)	4	S1	83.0	2.452	s	(83)
GRB 090926A	04:20:28.683	04:20:27.945	II	FermiLAT	(70)	5 6	S1	36.0	2.1062	s	(84)
GRB 091003	04:35:43.801	04:35:45.946	II	FermiLAT	(70)	5 6	S2	31.3	0.8969	s	(85)
GRB 091020	21:36:44.860	21:36:45.632	II	SwiftBAT	(64)	4 5	S2	46.1	1.71	s	(86)
GRB 091117A	17:44:29.513	17:44:25.673	I	SwiftBAT	(87)	4	S1	62.4	0.096	s	(88)
GRB 091127	23:25:49.449	23:25:45.602	II	SwiftBAT	(64)	4 5	S1	58.5	0.49034	s	(89)
GRB 100206A	13:30:06.775	13:30:05.433	I	SwiftBAT	(64)	4 5	S1	85.7	0.41	s	(90)
GRB 100414A	02:20:27.289	02:20:23.328	II	FermiLAT	(70)	4 5 6	S2	77.2	1.368	s	(91)
GRB 100606A	19:12:43.712	19:12:42.046	II	SwiftBAT	(64)	4	S1	35.6	1.5545	s	(54)
GRB 100621A	03:03:33.352	03:03:30.209	II	SwiftBAT	(64)	4	S1	57.4	0.542	s	(92)
GRB 100728A	02:18:20.008	02:18:24.502	II	SwiftBAT	(64)	4 5 6	S1	51.3	1.567	s	(93)
GRB 100814A	03:50:11.288	03:50:09.556	II	SwiftBAT	(64)	4 5	S1	64.7	1.44	s	(94)
GRB 100816A	00:37:53.983	00:37:51.215	II	SwiftBAT	(64)	4 5	S2	62.5	0.8049	s	(95)
GRB 100906A	13:49:30.732	13:49:28.387	II	SwiftBAT	(64)	4 5	S2	49.5	1.727	s	(96)
GRB 101213A	10:49:18.472	10:49:22.676	II	SwiftBAT	(64)	4 5	S2	48.2	0.414	s	(97)
GRB 101219A	02:31:34.716	02:31:29.786	I	SwiftBAT	(64)	4	S1	64.9	0.718	s	(98)
GRB 110213A	05:17:28.893	05:17:28.492	II	SwiftBAT	(64)	4 5	S2	58.8	1.46	s	(99)
GRB 110422A	15:41:42.948	15:41:45.300	II	SwiftBAT	(64)	4	S2	37.7	1.77	s	(100)
GRB 110503A	17:35:41.862	17:35:43.747	II	SwiftBAT	(64)	4	S2	56.9	1.613	s	(101)
GRB 110715A	13:13:55.304	13:13:51.418	II	SwiftBAT	(64)	4	S1	64.5	0.82	s	(102)
GRB 110731A	11:09:34.604	11:09:30.409	II	SwiftBAT	(64)	4 5 6	S1	84.6	2.83	s	(103)
GRB 110918A	21:27:02.856	21:26:58.937	II	IPN	(104)	...	S1	52.3	0.984	s	(105)
GRB 111008A	22:13:01.676	22:12:58.248	II	SwiftBAT	(64)	4	S1	38.1	5.0	s	(106)
GRB 111228A	15:45:36.171	15:45:34.790	II	SwiftBAT	(64)	4 5	S2	84.3	0.7156	s	(107)
GRB 120119A	04:04:34.872	04:04:31.459	II	SwiftBAT	(64)	4 5	S1	61.0	1.728	s	(108)
GRB 120624B	22:20:06.904	22:20:06.153	II	SwiftBAT	(64)	4 5 6	S2	85.4	2.1974	s	(109)
GRB 120711A	02:45:55.810	02:45:55.657	II	INTEGRAL	(110)	5 6	S1	4.8	1.405	s	(111)
GRB 120716A	17:05:07.357	17:05:04.087	II	IPN	(112)	5	S2	64.0	2.486	s	(113)
GRB 120804A	00:54:15.749	00:54:14.794	II	SwiftBAT	(64)	4	S2	99.2	1.3	p	(114)
GRB 121128A	05:05:53.703	05:05:53.474	II	SwiftBAT	(64)	4 5	S2	19.1	2.2	s	(115)
GRB 130408A	21:51:41.194	21:51:38.956	II	SwiftBAT	(64)	4	S1	43.0	3.758	s	(116)
GRB 130427A	07:47:09.501	07:47:06.468	II	SwiftBAT	(64)	4 5 6	S2	67.4	0.3399	s	(117)
GRB 130505A	08:22:27.038	08:22:26.527	II	SwiftBAT	(64)	4	S1	91.0	2.27	s	(118)
GRB 130518A	13:54:57.501	13:55:01.478	II	SwiftBAT	(64)	4 5 6	S2	45.9	2.488	s	(119)
GRB 130603B	15:49:16.448	15:49:14.164	I	SwiftBAT	(64)	4	S2	77.4	0.3565	s	(120)
GRB 130701A	04:17:42.161	04:17:43.592	II	SwiftBAT	(64)	4	S2	56.2	1.155	s	(121)
GRB 130831A	13:04:22.044	13:04:17.913	II	SwiftBAT	(64)	4	S2	62.7	0.4791	s	(122)
GRB 130907A	21:39:15.997	21:39:19.051	II	SwiftBAT	(64)	4	S2	35.0	1.238	s	(123)
GRB 131030A	20:56:17.811	20:56:13.932	II	SwiftBAT	(64)	4	S1	90.9	1.293	s	(124)
GRB 131105A	02:05:27.233	02:05:26.001	II	SwiftBAT	(64)	4 5	S1	8.8	1.686	s	(125)
GRB 131108A	20:41:52.947	20:41:55.851	II	FermiLAT	(126)	5 6	S2	89.9	2.40	s	(127)
GRB 131231A	04:45:32.361	04:45:31.276	II	FermiLAT	(128)	5 6	S1	84.1	0.6439	s	(129)
GRB 140213A	19:21:33.011	19:21:33.067	II	SwiftBAT	(64)	4 5	S1	8.4	1.2076	s	(130)
GRB 140419A	04:06:51.110	04:06:50.972	II	SwiftBAT	(64)	4	S2	63.7	3.956	s	(131)
GRB 140506A	21:07:39.098	21:07:37.801	II	SwiftBAT	(64)	4 5	S1	57.8	0.889	s	(132)
GRB 140508A	03:03:58.423	03:03:57.067	II	SwiftBAT	(64)	5	S2	24.6	1.027	s	(133)
GRB 140512A	19:31:50.769	19:31:49.555	II	SwiftBAT	(64)	4 5	S2	82.9	0.725	s	(134)
GRB 140606B	03:11:50.769	03:11:52.293	II	SwiftBAT	(64)	5	S2	46.8	0.384	s	(135)
GRB 140801A	18:59:54.769	18:59:54.138	II	FermiGBM	(136)	5	S2	81.2	1.320	s	(136)
GRB 140808A	00:53:59.264	00:54:01.038	II	FermiGBM	(137)	5	S2	31.6	3.293	s	(138)
GRB 141220A	06:02:51.666	06:02:52.662	II	SwiftBAT	(64)	4 5	S2	54.8	1.3195	s	(139)
GRB 150206A	14:31:20.265	14:31:22.868	II	SwiftBAT	(64)	4	S1	31.8	2.087	s	(140)
GRB 150314A	04:54:51.727	04:54:50.924	II	SwiftBAT	(64)	4 5 6	S2	46.9	1.758	s	(141)
GRB 150323A	02:51:22.369	02:51:20.908	II	SwiftBAT	(64)	4	S2	64.3	0.593	s	(142)
GRB 150403A	21:54:12.693	21:54:13.255	II	SwiftBAT	(64)	4 5 6	S1	47.3	2.06	s	(143)
GRB 150424A	07:43:01.073	07:42:57.738	I	SwiftBAT	(64)	4	S1	54.8	0.30 <sup>b</sup>	s	(144)
GRB 150514A	18:35:05.130	18:35:05.725	II	FermiLAT	(145)	5 6	S1	8.7	0.807	s	(146)
GRB 150821A	09:44:34.166	09:44:31.096	II	SwiftBAT	(64)	4 5	S1	44.7	0.755	s	(147)



**Table 1**  
(Continued)

Burst Name	Trigger Time	Geocenter Time	Type	Local. instr.	Local. References	Other <sup>c</sup> obs.	Det.	Inc. angle (deg)	$z$	$z$ type <sup>d</sup>	$z$ References
GRB 151021A	01:28:56.535	01:28:52.888	II	SwiftBAT	(64)	4	S1	67.9	2.330	s	(148)
GRB 151027A	03:58:24.154	03:58:24.488	II	SwiftBAT	(64)	4 5	S2	5.3	0.81	s	(149)
GRB 160131A	08:20:44.577	08:20:43.817	II	SwiftBAT	(64)	4	S1	60.1	0.972	s	(150)
GRB 160410A	05:09:52.644	05:09:48.172	I <sup>p</sup>	SwiftBAT	(64)	4	S1	82.0	1.717	s	(151)
GRB 160509A	08:58:46.696	08:58:48.075	II	FermiLAT	(152)	5 6	S2	15.8	1.17	s	(153)
GRB 160623A	04:59:37.594	04:59:36.336	II	FermiLAT	(154)	5 6	S2	34.5	0.367	s	(155)
GRB 160625B	22:40:19.875	22:40:18.938	II	FermiLAT	(156)	4 5 6	S2	65.1	1.406	s	(157)
GRB 160629A	22:19:45.314	22:19:46.474	II	INTEGRAL	(158)	5	S2	27.6	3.332	s	(159)

**Notes.**

<sup>a</sup> “Dark” burst according to the classification presented in the redshift reference paper.

<sup>b</sup> “Dark” burst according to Fynbo et al. (2009).

<sup>c</sup> Prompt emission observation(s): 1, *CGRO-BATSE*; 2, *HETE-2*; 3, *BeppoSAX-GRBM*; 4, *Swift-BAT*; 5, 6, *Fermi-LAT*.

<sup>d</sup> Redshift types are s, spectroscopic and p, photometric.

<sup>e</sup> Although this burst is referred to as GRB 020819 in all related GCN circulars and in some other publications, this is the second GRB observed by KW on 2002 August 19.

<sup>f</sup> This burst was initially referred to as GRB 050820, but, after the detection of GRB 050820B on the same day, it was renamed to GRB 050820A.

<sup>g</sup> The redshift at 95% confidence level is  $z = 2.77^{+0.15}_{-0.20}$ .

<sup>h</sup> Although GRB 060121 is a short-duration burst, it was classified as the Type II (see, e.g., Zhang et al. 2009 or S16 for details).

<sup>i</sup> The redshift study of GRB 060121 (de Ugarte Postigo et al. 2006) revealed two probability peaks. The main one (with a 63% likelihood) places the burst at  $z = 4.6 \pm 0.5$ . A secondary peak (with a 35% likelihood) would imply that the afterglow lies at a  $z = 1.7 \pm 0.4$ .

<sup>j</sup> The type of GRB 060614 is uncertain: an SN-less, long-duration burst (Della Valle et al. 2006; Gal-Yam et al. 2006; Gehrels et al. 2006; Fynbo et al. 2006) is suggested to be a Type I burst based on its host galaxy low specific star-forming rate (Zhang et al. 2009), while in the KW data this GRB was classified as a Type II burst based on duration and hardness only (see S16 for details).

<sup>k</sup> This burst is a short burst with extended emission (EE) according to Sakamoto et al. (2011a) and S16.

<sup>l</sup> The 95% confidence redshift range is  $1.37 < z < 2.20$ .

<sup>m</sup> The redshift at the  $2\sigma$  confidence level is  $z = 4.35 \pm 0.15$ .

<sup>n</sup> A rather wide 95% confidence range  $1.14 < z < 2.34$  is reported for this estimate.

<sup>o</sup> Since there is an ambiguity with the host galaxy identification, this redshift may not correspond to the burst. See the text (Section 3) for details.

<sup>p</sup> Although this GRB cannot be unambiguously assigned into the Type I population, we classify it as Type I. See the text (Section 3) for details.

**References.** (1) Frontera et al. (2009), (2) Bloom et al. (2001a), (3) Remillard et al. (1997), (4) Djorgovski et al. (2001), (5) Kulkarni et al. (1998), (6) Kulkarni et al. (1999), (7) Bloom et al. (2003a), (8) Vreeswijk et al. (2001), (9) Le Floch et al. (2002), (10) Hurley (1999), (11) Djorgovski et al. (1999), (12) Vreeswijk et al. (2006), (13) Kippen (2000), (14) Andersen et al. (2000), (15) Piro et al. (2002), (16) Smith et al. (2000), (17) Castro et al. (2000a), (18) Hurley et al. (2000a), (19) Hurley et al. (2000b), (20) Price et al. (2002a), (21) Hurley et al. (2000c), (22) Castro et al. (2000b), (23) Castro et al. (2001), (24) Price et al. (2002b), (25) Infante et al. (2001), (26) Masetti et al. (2002), (27) Table of *HETE* Burst Data (2006), (28) Barth et al. (2003), (29) Levesque et al. (2010), (30) Crew et al. (2002), (31) Della Valle et al. (2003), (32) Bloom et al. (2003b), (33) Fenimore et al. (2004), (34) Wiersema et al. (2004), (35) Galassi et al. (2004), (36) Price et al. (2004), (37) Sakamoto et al. (2011a), (38) Watson et al. (2006), (39) Foley et al. (2005), (40) Berger & Becker (2005), (41) Fox et al. (2008), (42) Jakobsson et al. (2006), (43) Volnova et al. (2014), (44) Gal-Yam et al. (2005), (45) Quimby et al. (2005), (46) Soderberg et al. (2006), (47) Prigozhin et al. (2006), (48) de Ugarte Postigo et al. (2006), (49) Fynbo et al. (2009), (50) Della Valle et al. (2006), (51) Krühler et al. (2012), (52) Levan et al. (2007), (53) Berger et al. (2007a), (54) Krühler et al. (2015), (55) Stratta et al. (2007), (56) Perley et al. (2009), (57) Hurley & Cline (2007), (58) Cenko et al. (2008), (59) Jakobsson et al. (2007), (60) Perley et al. (2013), (61) Graham et al. (2009), (62) Perley et al. (2008), (63) Stern et al. (2007), (64) Swift GRB Table (2016), (65) Berger et al. (2007b), (66) Rapisarda et al. (2008), (67) Rossi et al. (2008), (68) Prochaska et al. (2009), (69) Starling et al. (2009), (70) Fermi-LAT Collaboration (2013), (71) Greiner et al. (2009), (72) Berger & Rauch (2008), (73) Kuin et al. (2009), (74) Salvaterra et al. (2012), (75) Cucchiara et al. (2008), (76) de Ugarte Postigo et al. (2009b), (77) Chornock et al. (2009a), (78) Cenko et al. (2009a), (79) Chornock et al. (2009b), (80) Rau et al. (2009), (81) Cenko et al. (2009b), (82) Wiersema et al. (2009), (83) de Ugarte Postigo et al. (2009a), (84) Malesani et al. (2009), (85) Cucchiara et al. (2009), (86) Xu et al. (2009), (87) Sakamoto et al. (2009), (88) Chornock & Berger (2009), (89) Thoene et al. (2009), (90) Cenko et al. (2010), (91) Cucchiara & Fox (2010), (92) Milvang-Jensen et al. (2010), (93) Kruehler et al. (2013), (94) O’Meara et al. (2010), (95) Tanvir et al. (2010b), (96) Tanvir et al. (2010c), (97) Chornock & Berger (2011a), (98) Chornock & Berger (2011b), (99) Milne & Cenko (2011), (100) de Ugarte Postigo et al. (2011a), (101) de Ugarte Postigo et al. (2011b), (102) Piranomonte et al. (2011), (103) Tanvir et al. (2011), (104) Hurley et al. (2011), (105) de Ugarte Postigo et al. (2011c), (106) Sparre et al. (2014), (107) Palazzi et al. (2011), (108) Cucchiara & Prochaska (2012), (109) de Ugarte Postigo et al. (2013a), (110) IBAS: Results (2012), (111) Tanvir et al. (2012b), (112) Hurley et al. (2012), (113) D’Elia et al. (2012), (114) Berger et al. (2013), (115) Tanvir et al. (2012a), (116) Hjorth et al. (2013), (117) Flores et al. (2013), (118) Tanvir et al. (2013), (119) Cucchiara & Cenko (2013), (120) de Ugarte Postigo et al. (2014c), (121) Xu et al. (2013a), (122) Cucchiara & Perley (2013), (123) de Ugarte Postigo et al. (2013c), (124) Xu et al. (2013b), (125) Xu et al. (2013c), (126) Racusin et al. (2013), (127) de Ugarte Postigo et al. (2013b), (128) Sonbas et al. (2013), (129) Cucchiara (2014), (130) Schulze et al. (2014), (131) Tanvir et al. (2014), (132) Fynbo et al. (2014), (133) Wiersema et al. (2014), (134) de Ugarte Postigo et al. (2014a), (135) Perley et al. (2014), (136) Lipunov et al. (2016), (137) FERMIGBRST—*Fermi*-GBM Burst Catalog (von Kienlin et al. 2014; Gruber et al. 2014; Narayana Bhat et al. 2016), (138) Singer et al. (2015), (139) de Ugarte Postigo et al. (2014b), (140) Kruehler et al. (2015), (141) de Ugarte Postigo et al. (2015a), (142) Perley & Cenko (2015), (143) Pugliese et al. (2015), (144) Castro-Tirado et al. (2015), (145) Kocevski & Arimoto (2015), (146) de Ugarte Postigo et al. (2015c), (147) D’Elia et al. (2015), (148) de Ugarte Postigo et al. (2015b), (149) Perley et al. (2015), (150) de Ugarte Postigo et al. (2016), (151) Selsing et al. (2016), (152) Longo et al. (2016), (153) Tanvir et al. (2016), (154) Vianello et al. (2016), (155) Malesani et al. (2016), (156) Dirirsa et al. (2016), (157) Xu et al. (2016), (158) Gotz et al. (2016), (159) Castro-Tirado et al. (2016).

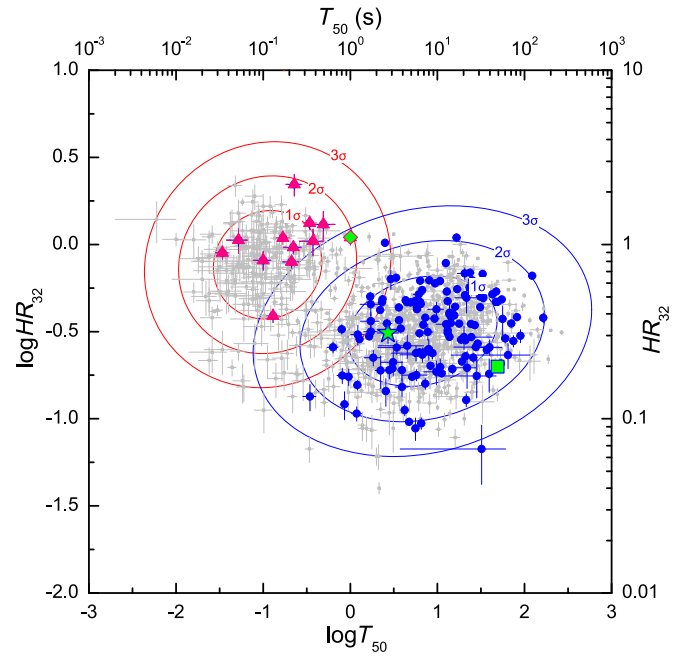
(This table is available in machine-readable form.)

Table 1. The first three columns contain the GRB name as provided in the Gamma-ray Burst Coordinates Network circulars,<sup>6</sup> the KW trigger time  $T_0$ , and the KW trigger time corrected for the burst front propagation from *Wind* to the Earth center (the geocenter time).

The “Type” column specifies the burst “physical” classification: Type I, the merger origin (Blinnikov et al. 1984; Paczynski 1986; Eichler et al. 1989; Paczynski 1991; Narayan et al. 1992), typically short/hard bursts, and Type II, the collapsar origin (Woosley 1993; Paczyński 1998; MacFadyen & Woosley 1999; Woosley & Bloom 2006), typically long/soft GRBs; see, e.g., Zhang et al. (2009) for more information on this classification scheme. According to the KW Type I/II criteria (S16), 11 GRBs from the sample can be confidently classified as Type I and 137 GRBs as Type II. Although  $T_{50} \approx 1.0$  s for GRB 160410A exceeds 0.6 s, a threshold used by S16 to distinguish between “short” and “long” KW GRBs, this burst may be classified as Type I based on its position in the hardness–duration distribution of a large sample of KW bright GRBs (Figure 1), and also on its short  $T_{90} \approx 1.6$  s (see Section 4.1 for definitions of  $T_{50}$  and  $T_{90}$ ). The physical classification of GRB 060614 is unclear: an SN-less, long-duration burst (Della Valle et al. 2006; Fynbo et al. 2006; Gal-Yam et al. 2006; Gehrels et al. 2006) was suggested to be Type I based on a low specific star-forming rate of its host galaxy (Zhang et al. 2009); conversely, from the KW prompt-emission analysis this GRB was classified by S16 as Type II, that we will use in this paper. Thus, of 150 GRBs in the sample, we designate 138 GRBs as Type II and 12 (or 8% of the sample) as Type I.

The next column indicates the mission/instrument that provided the most accurate GRB localization from prompt emission observations, thus enabling further identification of the source. Among 150 bursts in this catalog, 103 (or  $\sim 2/3$ ) are *Swift*-BAT GRBs, 13 were localized by *BeppoSAX*, 14 by *Fermi* (LAT and/or GBM), 8 by *HETE-2*, 2 by *INTEGRAL*-IBIS/ISGRI, and 2 by *RXTE*-ASM; for 10 GRBs, the best “prompt” localization was obtained with the help of triangulation by the IPN (Hurley et al. EAS Pub Ser., 61, 459, 2013). The “Other obs.” column provides the information on the burst prompt emission detections by other missions with spectrometric capabilities in hard X-ray and  $\gamma$ -ray domains. The statistics of these detections are as follows: *CGRO*-BATSE—5, *HETE-2*—10, *BeppoSAX*-GRBM—13, *Swift*-BAT—102, *Fermi*-GBM—52, and *Fermi*-LAT—21. The “Det.” and “Inc. angle” columns specify the KW triggered detector and the angle between the GRB direction and the detector axis (the incident angle).

The rightmost three columns of Table 1 contain the redshift data. For a number of GRBs there are several independent redshift estimates available, of which we gave a preference to spectroscopic over photometric redshifts, if available; also, results from refereed papers, which presented a detailed spectral analysis, were given higher priority over earlier GCN circulars. The redshift study of GRB 060121 (de Ugarte Postigo et al. 2006) revealed two probability peaks. The main one (which we chose for this catalog, with a 63% likelihood) places the burst at  $z = 4.6 \pm 0.5$ . A secondary peak (with a 35% likelihood) would imply that the source lies at  $z = 1.7 \pm 0.4$ . The redshift estimate we use for GRB 150424A ( $z = 0.3$ , Castro-Tirado et al. 2015) is based on the observation of a galaxy  $5''$  (22.5 kpc



**Figure 1.** Hardness-duration distribution of GRBs with known redshifts detected by KW in the triggered mode (Type I: red triangles; Type II: blue circles; GRB 160410A: green diamond; GRB 060614: green star, initial pulse, and green square, the whole burst). The distribution of 1143 KW bright GRBs (S16) is shown in the background. This distribution is fitted by a sum of two Gaussian distributions and the contours denote  $1\sigma$ ,  $2\sigma$ , and  $3\sigma$  confidence regions for each Gaussian distribution.

at this  $z$ ) away from the afterglow position reported by Perley & McConnell (2015). We note, however, that Tanvir et al. (2015) found a fainter potential host galaxy with a likely redshift of  $z > 0.7$  underlying the GRB position.

Figure 2 shows KW GRB redshift distributions along with those for the pre-*Swift*-era GRBs and all GRB redshifts measured to mid-2016. The KW GRB redshifts span the range  $0.1 \leq z \leq 5$  and have mean and median values of  $\sim 1.5$  and  $\sim 1.3$ , respectively. These statistics are comparable with those for the pre-*Swift* era GRBs, whose distribution peaks at  $z \sim 1$  (Berger et al. 2005), but they are significantly lower than the *Swift*-era values ( $\bar{z} \sim 2.3$ ; Coward et al. 2013). The fraction of the KW-detected GRBs is  $\sim 0.4$ – $0.5$  at  $z < 1$  and it gradually decreases with  $z$ ; for short/hard (Type I) bursts the fraction is  $\sim 0.5$ . The absence of high-redshift bursts ( $z > 5$ ) in the KW sample results from several instrument-specific biases discussed further in this paper.

## 4. Data Analysis and Results

### 4.1. Burst Durations and Spectral Lags

#### 4.1.1. Analysis

The total burst duration  $T_{100}$ , and the  $T_{90}$  and  $T_{50}$  durations (the time intervals that contain 5% to 95% and 25% to 75% of the total burst count fluence, respectively; see, e.g., Kouveliotou et al. 1993), were determined, in this work, using the counts in G2+G3 energy band ( $\sim 80$ – $1200$  keV at present). The soft energy band G1 was excluded from the analysis for a number of reasons, i.e., (1) the major fraction of the GRB spectra have the peak energy of the  $E_{\text{FE}}$  spectrum  $E_p > 100$  keV and hence photons responsible for the burst energy are detected mostly in the G2 and G3 bands; (2) the KW

<sup>6</sup> [http://gcn.gsfc.nasa.gov/gcn3\\_archive.html](http://gcn.gsfc.nasa.gov/gcn3_archive.html)

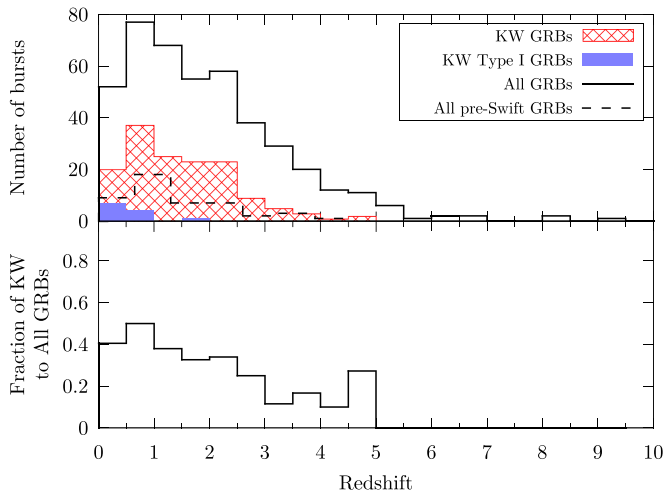


**Figure 2.** Redshift distributions for GRBs detected up to 2016 June.

background in G2 and G3 is very stable (in contrast to background in the soft energy range G1 ( $\sim 20$ – $80$  keV), which can exhibit significant variations due to solar activity and hard X-ray transients); (3) for some bursts, an emerging X-ray afterglow may be confused with the prompt emission in G1.

To compute the durations, a concatenation of waiting-mode and triggered-mode light curves was used. The burst’s start and end times were determined at  $5\sigma$  excess above background on timescales from 2 ms to 2.944 s in the interval from  $T_0 - 200$  s to  $T_0 + 240$  s (the end of the KW triggered mode record). In some cases, e.g., for GRB 020813, which partly overlaps in time with a solar flare, the search interval was narrowed to exclude the non-GRB event. The background was approximated by a constant, using, typically, the interval from  $T_0 - 1200$  s to  $T_0 - 200$  s.

The spectral lag ( $\tau_{\text{lag}}$ ) is a quantitative measure of spectral evolution often seen in long GRBs, when the emission in a soft detector band peaks later or has a longer decay relative to a hard band; a positive  $\tau_{\text{lag}}$  corresponds to the delay of the softer emission. To derive spectral lags we used a cross-correlation method similar to that described in Band (1997) and Norris et al. (2000). The cross-correlation function (CCF) was computed between three pairs of KW energy channels: G2–G1, G3–G1, and G2–G3. For each pair of channels (Gi, Gj) the peak of fourth-degree polynomial fit for the CCF was taken as  $\tau_{\text{lagGiGj}}$ . The  $\tau_{\text{lag}}$  error was estimated via the bootstrap approach. To ensure the robustness of the analysis, only bursts featuring a single emission episode, with start and end times being within the triggered mode record, were selected for the spectral lag calculations.

#### 4.1.2. Results

Table 2 summarizes the results of our temporal and lag analyses. The first column contains the GRB name (see Table 1). Next, the values of  $T_{100}$ ,  $T_{90}$ , and  $T_{50}$  are listed along with the corresponding start times  $t_0$ ,  $t_5$ , and  $t_{25}$  given relative to the trigger time  $T_0$ . For GRB 081203A, which was detected during the data output of GRB 081203B, no high-resolution light curves are available and, thus, only a rough estimate of  $T_{100}$  is provided. While for weak KW GRBs,  $T_{100}$

and  $T_{90}$  are nearly similar measures of duration (Figure 3), for brighter bursts,  $T_{100}$  becomes more sensitive to the existence of weak precursors or extended tails. This behavior is particularly apparent for such remarkable events as the “naked-eye” GRB 080319B (Racusin et al. 2008); the ultra-luminous GRB 110918A (Frederiks et al. 2013); the nearby, ultra-bright GRB 130427A (Maselli et al. 2014); and two recent highly energetic events, GRB 160623A (Frederiks et al. 2016) and GRB 160625B (Svinkin et al. 2016a; Zhang et al. 2016). The latter burst features a precursor separated from the main episode by a long interval of quiescence and the four former bursts are characterized by slowly decaying tails of hard X-ray emission that were bright enough to be detected in the KW G2 band for hundreds of seconds.

The last three columns of Table 2 present the spectral lags  $\tau_{\text{lagG2G1}}$ ,  $\tau_{\text{lagG3G1}}$ , and  $\tau_{\text{lagG3G2}}$ . For the 58 GRBs selected for the spectral lag analysis, the numbers of lags calculated are as follows:  $\tau_{\text{lagG2G1}}$  (G2–G1)—55,  $\tau_{\text{lagG3G1}}$  (G3–G1)—32, and  $\tau_{\text{lagG3G2}}$  (G3–G2)—38. The missing lag values are not constrained; this may be due to a weak detection in one or both analyzed channels, or to a significant difference in a pulse shape between them.

Figure 4 presents the  $T_{50}$ ,  $T_{90}$ , and  $T_{100}$  observer- and rest-frame distributions. The rest-frame quantities are the corresponding observer-frame values scaled by the time dilation factor  $1/(1+z)$ . We note that the observer-frame energy band G2+G3, in which the durations are calculated, corresponds to multiple energy bands in the source-frame thus introducing a variable energy-dependant factor which must be accounted for when analyzing the rest-frame durations. The same considerations apply to the spectral lags.

## 4.2. Energy Spectra

### 4.2.1. Analysis

For each burst from our sample, two time intervals were selected for spectral analysis: time-averaged fits were performed over the interval closest to  $T_{100}$  (hereafter the TI spectrum); the peak spectrum corresponds to the time when the peak count rate (PCR) is reached. The peak spectrum accumulation time may vary from burst to burst depending on the GRB intensity and the presence of significant spectral evolution. For 38 bursts with poor count statistics, the TI and the peak spectra are measured over the same interval.

More than a dozen bursts from the sample show two or more emission episodes separated by periods of quiescence. In the majority of cases, all emission episodes were included to the TI spectrum. KW triggered on weak precursors of GRB 120716A and GRB 160625B. To maintain a reasonable signal-to-noise ratio, only the main episodes of these bursts contributed to the spectral analysis presented in this paper.

The spectral analysis was performed using XSPEC version 12.9.0 (Arnaud 1996). The raw count rate spectra were rebinned to have a minimum of 20 counts per channel to ensure Gaussian-distributed count statistics and fitted using the  $\chi^2$  statistic. Each spectrum was fitted by two spectral models. The first model is the Band function (hereafter BAND; Band et al. 1993):

**Table 2**  
Durations and Spectral Lags

Burst Name	$t_0$ (s)	$T_{100}$ (s)	$t_5$ (s)	$T_{90}$ (s)	$t_{25}$ (s)	$T_{50}$ (s)	$\tau_{\text{lagG2G1}}$ (s)	$\tau_{\text{lagG3G1}}$ (s)	$\tau_{\text{lagG3G2}}$ (s)
GRB 970228	−0.456	56.584	−0.002 ± 0.024	53.442 ± 2.891	0.592 ± 0.048	39.280 ± 2.556	...	...	...
GRB 970828	−4.248	94.936	0.864 ± 0.112	66.208 ± 2.781	7.680 ± 0.161	17.792 ± 0.310	...	...	...
GRB 971214	−9.060	16.564	−9.060 ± 2.082	15.892 ± 2.133	−3.172 ± 2.951	6.724 ± 2.970	...	...	...
GRB 990123	−17.312	111.200	1.600 ± 0.161	62.016 ± 1.179	7.904 ± 0.072	26.336 ± 0.757	0.681 ± 0.091	0.619 ± 0.099	0.165 ± 0.050
GRB 990506	−0.390	164.742	1.952 ± 0.041	128.608 ± 0.654	12.032 ± 0.088	83.392 ± 2.565	...	...	...
GRB 990510	−0.320	69.568	0.688 ± 0.186	55.888 ± 8.108	38.976 ± 1.735	5.760 ± 1.745	...	...	...
GRB 990705	−1.698	67.746	1.648 ± 0.066	33.232 ± 1.120	7.488 ± 0.096	14.720 ± 0.211	0.053 ± 0.016	0.103 ± 0.063	0.016 ± 0.014
GRB 990712	−1.637	18.821	−1.637 ± 0.862	16.629 ± 1.777	0.784 ± 0.173	10.784 ± 0.470	...	...	...
GRB 991208	−0.148	76.436	0.688 ± 0.016	63.056 ± 0.481	5.136 ± 1.562	53.680 ± 1.567	...	...	...
GRB 991216	−17.477	44.629	0.672 ± 0.032	14.528 ± 0.140	3.264 ± 0.025	4.704 ± 0.154	...	...	...
GRB 000131	−77.719	105.735	−74.775 ± 2.944	96.471 ± 3.125	−18.839 ± 12.138	27.719 ± 12.280	...	...	...

**Note.** A positive value of the spectral lag  $\tau_{\text{lag}}$  corresponds to a delay of the soft photons.

(This table is available in its entirety in machine-readable form.)



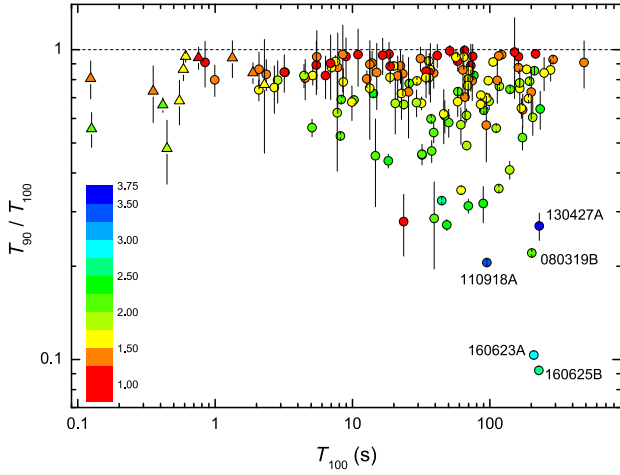


**Figure 3.**  $T_{90}$  to  $T_{100}$  ratio plotted vs.  $T_{100}$ . Type I and Type II GRBs are shown with triangles and circles, respectively. The color of each data point represents the log of the burst's trigger significance ( $\sigma$ ).

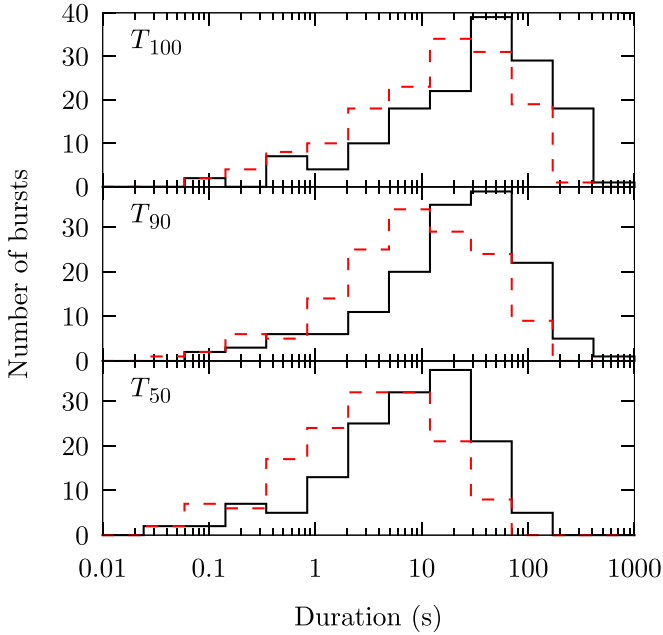


**Figure 4.** Distributions of  $T_{100}$  (top),  $T_{90}$  (middle), and  $T_{50}$  (bottom) in the observer- and cosmological rest frames (black solid and red dashed lines, respectively).

exponentially cutoff power-law (CPL), parameterized as  $E_p$ :

$$f(E) \propto E^\alpha \exp\left(-\frac{E(2 + \alpha)}{E_p}\right). \quad (2)$$

In the only case where both “curved” models result in ill-constrained fits (GRB 080413B), a simple power-law (PL) function was used:  $f(E) \propto E^\alpha$ . All the spectral models were normalized to the energy flux ( $F$ ) in the 10 keV–10 MeV range (observer frame). The fits were performed in the energy range from  $\sim 20$  keV to the upper limit of 0.5–15 MeV, depending on the presence of statistically significant GRB emission in the MeV band and, also, on the stability of the background in the upper spectral channels, which are affected, for some GRBs, by solar particles. The parameter errors were estimated using the XSPEC command ERROR based on the change in fit statistic ( $\Delta\chi^2 = 1$ ) which corresponds to the 68% CL.

For each spectrum, we present the results for the models whose parameters are constrained (hereafter, GOOD models). The best-fit spectral model (the BEST model) was chosen based on the difference in  $\chi^2$  between the CPL and the BAND fits. The criterion for accepting a model with a single additional parameter is a change in  $\chi^2$  of at least 6 ( $\Delta\chi^2 \equiv \chi_{\text{CPL}}^2 - \chi_{\text{BAND}}^2 > 6$ ). This criterion is widely accepted for choosing between nested spectral models in GRB studies (see, e.g., Sakamoto et al. 2008; Krimm et al. 2009; Goldstein et al. 2012) and corresponds to an  $F$  test chance improvement probability of  $\sim 0.015$  for a reasonably good quality of fit (the reduced chi-squared, i.e., the chi-squared per degree of freedom (d.o.f.),  $\chi_r^2 \sim 1$ ). It should be noted that in the KW GCN circulars a different approach is used for the best-fit model selection: BAND is preferred over CPL in the case of the constrained fit, and not dependent on  $\Delta\chi^2$ .

#### 4.2.2. Results

The 10 columns in Table 3 contain the following information: (1) the GRB name (see Table 1); (2) the spectrum type, where “i” indicates that the spectrum is TI, “p” means that the spectrum is peak; (3) and (4) contain the spectrum start time  $t_{\text{start}}$  (relative to  $T_0$ ) and its accumulation time  $\Delta T$ ; (5) GOOD models for each spectrum ( $\dagger$  indicates the BEST model); (6)–(8)  $\alpha$ ,  $\beta$ , and  $E_p$ ; (9)  $F$  (normalization); (10)  $\chi^2/\text{d.o.f.}$  along with the null hypothesis probability given in brackets. In cases where the lower limit for  $\beta$  is not constrained, the value of  $(\beta_{\text{min}} - \beta)$  is provided instead,

$$f(E) \propto \begin{cases} E^\alpha \exp\left(-\frac{E(2 + \alpha)}{E_p}\right), & E < (\alpha - \beta) \frac{E_p}{2 + \alpha} \\ E^\beta \left[(\alpha - \beta) \frac{E_p}{(2 + \alpha)}\right]^{(\alpha - \beta)} \exp(\beta - \alpha), & E \geq (\alpha - \beta) \frac{E_p}{2 + \alpha}, \end{cases} \quad (1)$$

where  $\alpha$  is the low-energy photon index and  $\beta$  is the high-energy photon index. The second spectral model is an

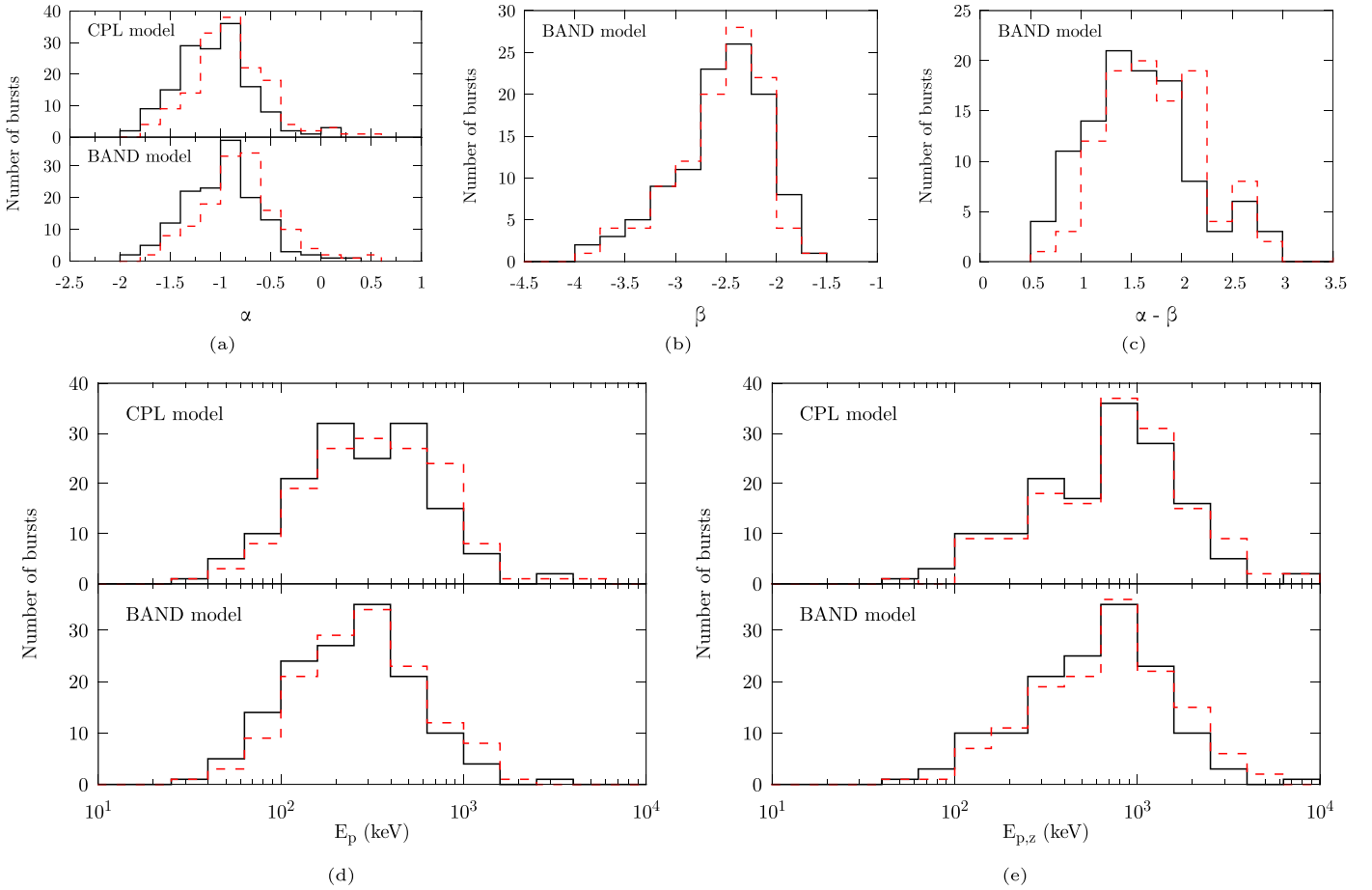
where  $\beta_{\text{min}} = -10$  is the lower limit for the fits. For the best-fit values of  $\beta < -4$ , only the upper limits on  $\beta$  are given.

**Table 3**  
Spectral Parameters

Burst Name	Spec. Type	$t_{\text{start}}$ (s)	$\Delta T$ (s)	Model	$\alpha$	$\beta$	$E_p$ (keV)	$F$ ( $10^{-6}$ erg cm $^{-2}$ s $^{-1}$ )	$\chi^2/\text{d.o.f.}$ (Prob.)
GRB 970228	i	0.000	8.448	CPL <sup>a</sup>	$-1.27^{+0.24}_{-0.22}$	...	$165^{+39}_{-25}$	$0.53^{+0.06}_{-0.05}$	44.9/56 (0.86)
	i			Band	$-1.24^{+0.31}_{-0.22}$	$-2.82^{+0.60}_{-7.18}$	$159^{+38}_{-36}$	$0.60^{+0.06}_{-0.06}$	44.5/55 (0.84)
	p	0.000	0.256	CPL <sup>a</sup>	$-0.81^{+0.32}_{-0.27}$	...	$309^{+102}_{-60}$	$3.38^{+0.42}_{-0.40}$	13.3/24 (0.96)
	p			Band	$-0.76^{+0.49}_{-0.29}$	$-2.64^{+0.70}_{-7.36}$	$286^{+102}_{-105}$	$4.14^{+0.47}_{-0.47}$	13.0/23 (0.95)
GRB 970828	i	0.000	70.656	CPL	$-0.86^{+0.04}_{-0.04}$	...	$346^{+19}_{-17}$	$0.89^{+0.03}_{-0.03}$	72.6/66 (0.27)
	i			Band <sup>a</sup>	$-0.73^{+0.06}_{-0.06}$	$-2.18^{+0.11}_{-0.15}$	$271^{+24}_{-22}$	$1.33^{+0.05}_{-0.05}$	63.5/65 (0.53)
	p	17.920	5.120	CPL	$-0.91^{+0.05}_{-0.05}$	...	$355^{+29}_{-25}$	$2.20^{+0.10}_{-0.10}$	68.6/79 (0.79)
	p			Band <sup>a</sup>	$-0.78^{+0.08}_{-0.07}$	$-2.18^{+0.12}_{-0.15}$	$271^{+31}_{-28}$	$3.23^{+0.27}_{-0.26}$	57.6/78 (0.96)
GRB 971214	i	0.000	8.448	CPL <sup>a</sup>	$-0.50^{+0.19}_{-0.17}$	...	$179^{+20}_{-16}$	$0.39^{+0.03}_{-0.03}$	72.2/78 (0.66)
	i			Band	$-0.32^{+0.26}_{-0.22}$	$-2.39^{+0.23}_{-0.35}$	$154^{+20}_{-19}$	$0.58^{+0.11}_{-0.09}$	67.8/77 (0.77)

**Note.**<sup>a</sup> Indicates the BEST model for the spectrum.

(This table is available in its entirety in machine-readable form.)

**Figure 5.** Distributions of spectral parameters  $\alpha$ ,  $\beta$ ,  $E_p$ , and  $E_{p,z} = (1+z)E_p$  for GOOD models. All the panels display the comparison between the TI spectral parameters (solid black lines) and the peak spectral parameters (dashed red lines). Panels (a), (d), and (e) also display the comparison between CPL and BAND spectral parameters.

Although KW high-resolution spectra do not cover the pre-trigger emission, for about two-thirds of GRBs in our sample the TI spectra include  $\geq 90\%$  of the burst counts (and only for six bursts this fraction is  $< 50\%$ ). A major fraction of the GRB 090812 counts, about one-half of the short GRB 100206A counts, and a significant fraction of the short GRB 070714B counts were accumulated before the trigger. For these bursts, we performed

the spectral analysis using both multichannel spectra and the three-channel spectra constructed from light-curve data. Together, these spectra cover the burst  $T_{100}$  interval.

Figure 5 shows the distributions of spectral parameters. The CPL model's  $\alpha$  for both TI and peak spectra are distributed around  $\alpha \approx -1$ . For the BAND model,  $\alpha$  for the TI and peak spectra are distributed around  $\approx -1$  and  $\approx -0.85$ , respectively.

The high-energy photon indices  $\beta$  for the TI and peak spectra are distributed around  $\approx -2.5$  and  $\approx -2.35$ , respectively. We found BAND to be the BEST model for 54 TI and 51 peak spectra. The remaining spectra (with the exception of GRB 080413B) were best fitted by CPL.  $E_p$  for the BEST model varies from  $\approx 40$  keV to  $\approx 3.5$  MeV (GRB 090510). The TI spectrum  $E_p$  ( $E_{p,i}$ ) distributions for both spectral models peak around 250 keV, while the peak spectrum  $E_p$  ( $E_{p,p}$ ) distributions peak around 300 keV. The corresponding rest-frame peak energies,  $E_{p,i,z} = (1+z)E_{p,i}$  and  $E_{p,p,z} = (1+z)E_{p,p}$ , vary from  $\approx 50$  keV to  $\approx 6.7$  MeV (GRB 090510).

### 4.3. Burst Energetics

#### 4.3.1. Fluences and Peak Fluxes

The energy fluences ( $S$ ) and the peak energy fluxes ( $F_{\text{peak}}$ ) were derived using the 10 keV–10 MeV energy fluxes of the BEST models for TI and peak spectra, respectively (Section 4.2). Since the TI spectrum accumulation interval typically differs from the  $T_{100}$  interval, a correction that accounts for the emission outside the TI spectrum was introduced when calculating  $S$ . Three timescales  $\Delta T_{\text{peak}}$  were used when calculating  $F_{\text{peak}}$ : together with two commonly utilized ones (1024 and 64 ms), we introduce the “rest-frame 64 ms” scale  $((1+z) \cdot 64 \text{ ms})$ ; the latter were used to estimate the rest-frame peak luminosity  $L_{\text{iso}}$ . To obtain  $F_{\text{peak}}$ , the model energy flux of the peak spectrum was multiplied by the ratio of the PCR on the  $\Delta T_{\text{peak}}$  scale to the average count rate in the spectral accumulation interval. Typically, the corrections were made using counts in the G2+G3 light curve; the G1+G2, G2 only, and G1+G2+G3 combinations were also considered depending on the emission hardness and intensity.

#### 4.3.2. $k$ -correction and Rest-frame Energetics

The cosmological rest-frame energetics, the isotropic-equivalent energy release  $E_{\text{iso}}$  and the isotropic-equivalent peak luminosity  $L_{\text{iso}}$ , can be calculated, with the proper  $k$ -correction, as  $E_{\text{iso}} = \frac{4\pi D_L^2}{1+z} \times S \times k$  and  $L_{\text{iso}} = 4\pi D_L^2 \times F_{\text{peak}} \times k$ ; where  $D_L$  is the luminosity distance. The  $k$ -correction to the rest-frame (see, e.g., Bloom et al. 2001b or Kovács et al. 2011 for details) is formulated in terms of spectral model energy flux  $F$  as

$$k = \frac{F[E_1/(1+z), E_2/(1+z)]}{F[e_1, e_2]},$$

where  $[e_1 = 10 \text{ keV}, e_2 = 10 \text{ MeV}]$  is our flux calculation band in the observer frame, and  $[E_1, E_2]$  is the rest-frame “bolometric” energy band. For  $E_1$ , we accept 1 keV and for  $E_2$ , we calculate  $(1+z) \cdot e_2 = (1+z) \cdot 10 \text{ MeV}$ . The latter value is higher than the widely used rest-frame limit of 10 MeV, since the upper boundary of the KW energy range is rather high ( $>10 \text{ MeV}$ ) and choosing  $E_2 = 10 \text{ MeV}$  would narrow the energy band of our observations.

#### 4.3.3. Collimation-corrected Energetics

Knowing  $t_{\text{jet}}$ , one can estimate the collimation-corrected energy released in gamma-rays  $E_\gamma = E_{\text{iso}}(1 - \cos \theta_{\text{jet}})$  and the collimation-corrected peak luminosity  $L_\gamma = L_{\text{iso}}(1 - \cos \theta_{\text{jet}})$ , where  $\theta_{\text{jet}}$  is the jet opening angle and  $(1 - \cos \theta_{\text{jet}})$  is the collimation factor.

In the case of a CBM with constant number density  $n$ , hereafter HM,  $\theta_{\text{jet}}$  is given by Sari et al. (1999):

$$\theta_{\text{jet, HM}} = \frac{1}{6} \left( \frac{t_{\text{jet}}}{1+z} \right)^{3/8} \left( \frac{n\eta_\gamma}{E_{\text{iso},52}} \right)^{1/8}, \quad (3)$$

where  $\eta_\gamma$  is the radiative efficiency of the prompt phase,  $E_{\text{iso},52}$  is the prompt emitted energy in units of  $10^{52} \text{ erg}$ , and  $t_{\text{jet}}$  is measured in days. For calculations, we adopted canonical values  $\eta_\gamma = 0.2$  and  $n = 1 \text{ cm}^{-3}$  (Frail et al. 2001).

In the case of a stellar-wind-like CBM with  $n(r) \propto r^{-2}$ , hereafter WM, the jet opening angle according to Li & Chevalier (2003) is

$$\theta_{\text{jet, WM}} = 0.2016 \left( \frac{t_{\text{jet}}}{1+z} \right)^{1/4} \left( \frac{\eta_\gamma A_*}{E_{\text{iso},52}} \right)^{1/4}, \quad (4)$$

where  $A_* = (\dot{M}_w / (4\pi v_w)) / (5 \times 10^{11} \text{ g cm}^{-1})$  is the wind parameter,  $\dot{M}_w$  is the mass-loss rate due to the wind, and  $v_w$  is the wind velocity;  $A_* \sim 1$  is typical for a Wolf–Rayet star. Following Ghirlanda et al. (2007), we assume  $A_* = 1$  for all bursts with WM neglecting the unknown uncertainty of this parameter.

In this work, we only consider jet breaks that were detected either in optical/IR afterglow light curves or in two spectral bands simultaneously (e.g., in X-ray and in radio). Among  $\sim 60$  jet breaks reported for KW GRBs in the literature, 32 meet this criterion (including two for Type I bursts, GRB 051221A and GRB 030603B), and 23 of those GRBs have reasonable constraints on the CBM density profile (14 HM and 9 WM).

#### 4.3.4. Results

Table 4 summarizes observer-frame and non-collimated rest-frame energetics. The first two columns are the GRB name and  $z$ . The next seven columns present the observer-frame energetics:  $S$ ; peak fluxes on the three timescales ( $F_{\text{peak},1024}$  (1024 ms),  $F_{\text{peak},64}$  (64 ms), and  $F_{\text{peak},64,r} ((1+z) \cdot 64 \text{ ms})$ ), together with start times of the intervals when the PCR is reached ( $T_{\text{peak},1024}$ ,  $T_{\text{peak},64}$ , and  $T_{\text{peak},64,r}$ ). The next two columns contain  $E_{\text{iso}}$  and the peak isotropic luminosity,  $L_{\text{iso}}$ , calculated from  $F_{\text{peak},64,r}$ . The provided  $L_{\text{iso}}$  values may be adjusted to a different timescale  $\Delta T$  (64 or 1024 ms) as:

$$L_{\text{iso}}(\Delta T) = \frac{F_{\text{peak}}(\Delta T)}{F_{\text{peak},64,r}} L_{\text{iso}}.$$

The rightmost columns provide two additional characteristics useful when the sample selection effects are considered: the bolometric energy flux corresponding to the GRB detection threshold,  $F_{\text{lim}}$  (Section 5.3); and  $z_{\text{max}}$ , the GRB detection horizon described in Section 5.4.

In Figure 6, the distributions of  $S$ ,  $F_{\text{peak},64}$ ,  $E_{\text{iso}}$ , and  $L_{\text{iso}}$  are shown. The most fluent burst in this catalog is GRB 130427A ( $S = 2.86 \times 10^{-3} \text{ erg cm}^{-2}$ ). The brightest burst based on the peak energy flux is GRB 110918A ( $F_{\text{peak},64} = 9.02 \times 10^{-4} \text{ erg cm}^{-2} \text{ s}^{-1}$ ). The most energetic burst in terms of the isotropic energy is GRB 090323 ( $E_{\text{iso}} = 5.81 \times 10^{54} \text{ erg}$ ). The most luminous burst contained in this catalog is GRB 110918A ( $L_{\text{iso}} = 4.65 \times 10^{54} \text{ erg s}^{-1}$ ).

Table 5 summarizes the collimation-corrected energetics for 32 bursts with “reliable” jet break times. The first column is the burst

**Table 4**  
Burst Energetics

Burst Name	$z$	$S^b$	$T_{\text{peak},1024}^c$	$F_{\text{peak},1024}^d$	$T_{\text{peak},64}^c$	$F_{\text{peak},64}^d$	$T_{\text{peak},64,r}^c$	$F_{\text{peak},64,r}^d$	$E_{\text{iso}}^e$	$L_{\text{iso}}^f$	$F_{\text{lim}}^d$	$z_{\text{max}}$
GRB 970228	0.69	$8.07^{+0.49}_{-0.41}$	$-0.512^a$	$2.24^{+0.43}_{-0.34}$	0.106	$4.59^{+0.80}_{-0.78}$	0.118	$4.12^{+0.66}_{-0.64}$	$12.01 \pm 0.93$	$9.6 \pm 1.5$	0.92	1.32
GRB 970828	0.96	$101.8^{+3.5}_{-3.6}$	20.256	$4.30^{+0.46}_{-0.44}$	20.416	$6.16^{+0.88}_{-0.87}$	20.416	$6.11^{+0.71}_{-0.71}$	$262.2 \pm 9.1$	$30.9 \pm 3.6$	1.1	1.85
GRB 971214	3.42	$5.72^{+0.24}_{-0.22}$	2.752	$0.604^{+0.071}_{-0.068}$	5.664	$0.99^{+0.25}_{-0.25}$	-0.280	$0.69^{+0.12}_{-0.11}$	$146.3 \pm 6.1$	$78 \pm 13$	0.44	4.05
GRB 990123	1.60	$310.6^{+8.0}_{-7.8}$	5.872	$25.6^{+1.1}_{-1.1}$	6.048	$29.1^{+2.3}_{-2.3}$	5.984	$27.7^{+1.6}_{-1.6}$	$2133 \pm 54$	$490 \pm 29$	3.1	5.04
GRB 990506	1.31	$261.0^{+8.8}_{-8.8}$	87.040	$9.32^{+0.47}_{-0.46}$	90.048	$13.8^{+1.1}_{-1.1}$	87.360	$12.13^{+0.69}_{-0.68}$	$1255 \pm 43$	$134.2 \pm 7.6$	0.92	3.80
GRB 990510	1.62	$21.72^{+0.89}_{-0.82}$	44.160	$3.56^{+0.35}_{-0.33}$	44.224	$5.57^{+0.80}_{-0.78}$	44.544	$4.35^{+0.52}_{-0.50}$	$174.2 \pm 8.1$	$81.0 \pm 9.6$	0.76	3.37
GRB 990705	0.84	$109.0^{+3.8}_{-3.8}$	14.000	$4.80^{+0.44}_{-0.42}$	15.856	$8.92^{+0.96}_{-0.96}$	15.824	$8.36^{+0.76}_{-0.76}$	$218.1 \pm 7.7$	$30.7 \pm 2.8$	0.84	2.02
GRB 990712	0.43	$6.25^{+0.38}_{-0.33}$	10.880	$0.802^{+0.118}_{-0.087}$	11.456	$1.10^{+0.17}_{-0.17}$	11.504	$1.05^{+0.14}_{-0.14}$	$3.86 \pm 0.28$	$1.20 \pm 0.18$	1.1	0.50
GRB 991208	0.71	$154.9^{+2.9}_{-3.0}$	56.256	$18.59^{+0.55}_{-0.53}$	56.960	$22.0^{+1.1}_{-1.1}$	56.960	$21.88^{+0.87}_{-0.86}$	$233.4 \pm 4.6$	$53.2 \pm 2.1$	0.61	3.30
GRB 991216	1.02	$297.0^{+3.8}_{-3.7}$	3.840	$47.6^{+3.2}_{-3.1}$	4.032	$99.4^{+4.7}_{-4.7}$	3.952	$86.9^{+3.6}_{-3.6}$	$886 \pm 11$	$510 \pm 21$	1.6	5.73
GRB 000131	4.50	$45.3^{+1.3}_{-1.3}$	2.144	$3.09^{+0.27}_{-0.26}$	2.880	$5.68^{+0.63}_{-0.63}$	2.672	$3.99^{+0.28}_{-0.28}$	$1817 \pm 56$	$859 \pm 60$	0.67	8.48

**Notes.**

<sup>a</sup> Since the trigger mode light curve begins at  $T_0 - 0.512$  s, the corresponding peak energy flux may be underestimated due to the absence of high-res data before  $T_0 - 0.512$  s.

<sup>b</sup> In units of  $10^{-6}$  erg  $\text{cm}^{-2}$ .

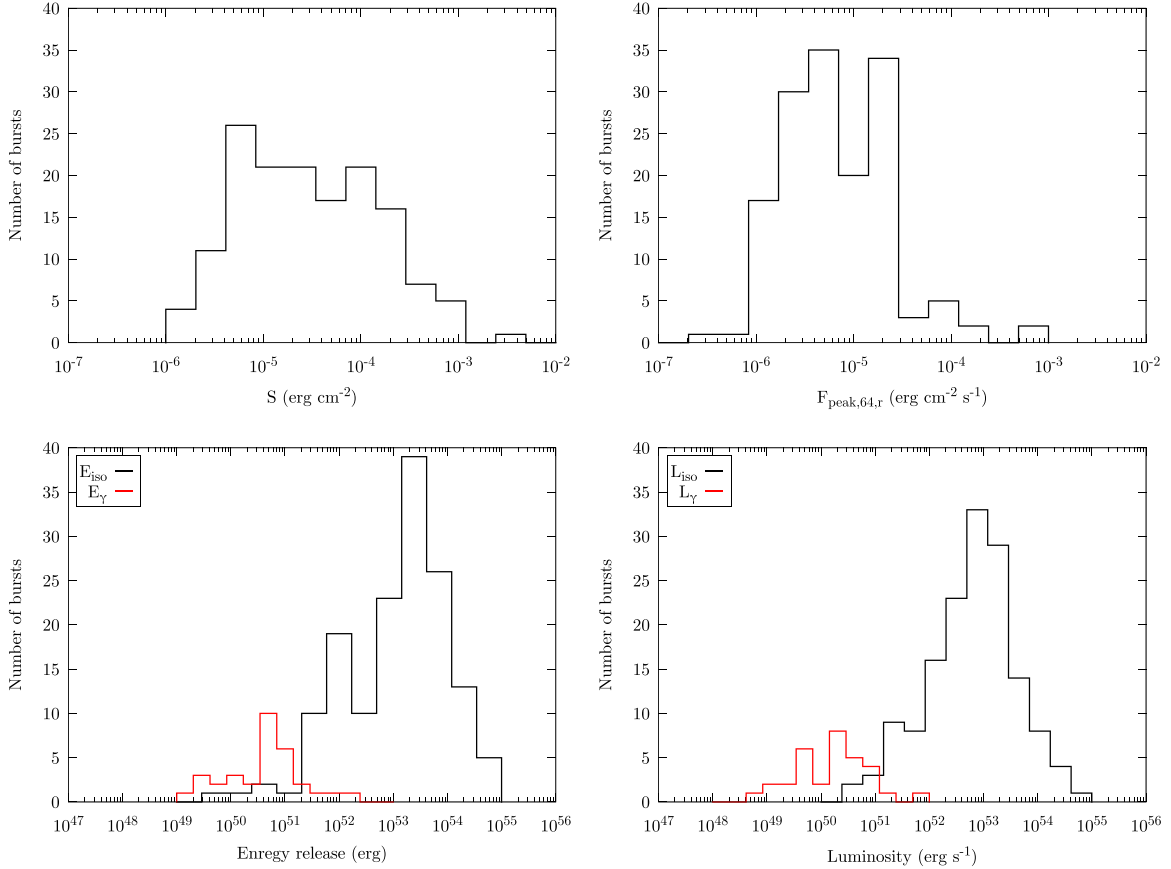
<sup>c</sup> The start time of the time interval when the peak count rate is reached, s.

<sup>d</sup> In units of  $10^{-6}$  erg  $\text{cm}^{-2} \text{s}^{-1}$ .

<sup>e</sup> In units of  $10^{51}$  erg.

<sup>f</sup> In units of  $10^{51}$  erg  $\text{s}^{-1}$ .

(This table is available in its entirety in machine-readable form.)

**Figure 6.** Distributions of GRB energetics:  $S$  (top left panel);  $F_{\text{peak}}$  (top right panel); isotropic and collimation-corrected energy releases  $E_{\text{iso}}$  and  $E_{\gamma}$  (bottom left panel), and peak luminosities  $L_{\text{iso}}$  and  $L_{\gamma}$  (bottom right panel).

name. The next three columns specify  $t_{\text{jet}}$ , the CBM environment implied (HM or WM), and references to them. The next two columns contain the derived  $\theta_{\text{jet}}$  and the corresponding

collimation factor, and the last two columns present  $E_{\gamma}$  and  $L_{\gamma}$ . For bursts with no reasonable constraint on the CBM profile the results are given for both HM and WM.



**Table 5**  
Collimation-corrected Parameters

Burst Name	$t_{\text{jet}}$ (days)	CBM	References <sup>a</sup>	$\theta_{\text{jet}}$ (deg)	Collimation factor ( $\times 10^{-3}$ )	$E_{\gamma}$ ( $10^{49}$ erg)	$L_{\gamma}$ ( $10^{49}$ erg s $^{-1}$ )
GRB 990123	$2.06^{+0.83}_{-0.83}$	WM	(1)	$1.91 \pm 0.19$	$0.55 \pm 0.12$	$118.10 \pm 24.10$	$27.16 \pm 5.74$
GRB 990510	$1.31^{+0.07}_{-0.07}$	HM	(1)	$4.21 \pm 0.09$	$2.70 \pm 0.11$	$47.07 \pm 3.20$	$21.90 \pm 0.95$
GRB 990705	1 <sup>b</sup>	HM <sup>c</sup>	(2)	$4.23 \pm 0.32$	$2.72 \pm 0.42$	$59.31 \pm 9.13$	$8.36 \pm 1.26$
GRB 990712	$1.61^{+0.19}_{-0.19}$	WM	(3)	$3.07 \pm 0.16$	$1.43 \pm 0.15$	$31.28 \pm 3.21$	$4.41 \pm 0.41$
		HM <sup>c</sup>		$9.20 \pm 0.42$	$12.90 \pm 1.19$	$4.96 \pm 0.68$	$1.54 \pm 0.28$
		WM		$10.10 \pm 0.35$	$15.50 \pm 1.09$	$5.98 \pm 0.60$	$1.85 \pm 0.34$
GRB 991216	$1.1^{+0.13}_{-0.13}$	WM	(1)	$2.16 \pm 0.06$	$0.71 \pm 0.04$	$63.13 \pm 3.88$	$36.32 \pm 2.68$
GRB 000301C	$7.3^{+0.5}_{-0.5}$	HM	(4)	$9.33 \pm 0.30$	$13.20 \pm 0.85$	$44.56 \pm 7.20$	$74.95 \pm 8.08$
GRB 000418	$7.85^{+2.71}_{-2.71}$	HM <sup>c</sup>	(1)	$9.62 \pm 1.25$	$14.10 \pm 3.87$	$134.50 \pm 44.78$	$53.39 \pm 16.34$
		WM		$6.09 \pm 0.53$	$5.65 \pm 1.03$	$54.04 \pm 12.13$	$21.44 \pm 4.70$
		WM		$3.07 \pm 0.06$	$1.43 \pm 0.06$	$39.83 \pm 2.46$	$16.24 \pm 2.05$
GRB 000926	$2.1^{+0.15}_{-0.15}$	WM	(1)	$3.07 \pm 0.06$	$0.54 \pm 0.03$	$57.63 \pm 3.81$	$12.56 \pm 1.17$
GRB 010222	$0.93^{+0.15}_{-0.06}$	WM	(5), (1)	$1.88 \pm 0.06$	$0.54 \pm 0.03$	$57.63 \pm 3.81$	$12.56 \pm 1.17$
GRB 010921	$35^{+5}_{-5}$	HM	(6)	$25.51 \pm 1.37$	$97.50 \pm 10.60$	$105.70 \pm 16.10$	$16.98 \pm 2.43$
GRB 011121	$1.54^{+0.22}_{-0.22}$	WM	(1)	$4.49 \pm 0.16$	$3.07 \pm 0.23$	$30.39 \pm 2.26$	$4.09 \pm 0.42$
GRB 020405	$2.4^{+0.45}_{-0.45}$	WM	(1)	$4.56 \pm 0.21$	$3.16 \pm 0.30$	$37.07 \pm 3.65$	$5.45 \pm 0.74$
GRB 020813	$0.77^{+0.25}_{-0.25}$	HM	(1)	$3.04 \pm 0.37$	$1.41 \pm 0.36$	$106.70 \pm 27.01$	$22.22 \pm 5.49$
GRB 030329	$0.69^{+0.08}_{-0.06}$	HM	(7)	$6.02 \pm 0.23$	$5.51 \pm 0.43$	$9.11 \pm 0.87$	$1.23 \pm 0.10$
GRB 041006	$0.23^{+0.04}_{-0.04}$	WM	(1)	$5.13 \pm 0.23$	$4.00 \pm 0.37$	$2.75 \pm 0.26$	$2.15 \pm 0.42$
GRB 050401	$1.5^{+0.5}_{-0.5}$	HM <sup>c</sup>	(8)	$3.38 \pm 0.42$	$1.74 \pm 0.46$	$80.59 \pm 21.26$	$36.98 \pm 10.05$
		WM		$2.33 \pm 0.20$	$0.83 \pm 0.14$	$38.38 \pm 6.78$	$17.61 \pm 3.45$
		HM <sup>c</sup>		$2.83 \pm 0.06$	$1.22 \pm 0.05$	$3.43 \pm 0.17$	$2.33 \pm 0.10$
GRB 050525A	$0.152^{+0.008}_{-0.008}$	WM	(9)	$3.31 \pm 0.05$	$1.67 \pm 0.05$	$4.68 \pm 0.16$	$3.18 \pm 0.19$
GRB 050820A	$18^{+2}_{-2}$	HM	(10)	$7.99 \pm 0.33$	$9.70 \pm 0.83$	$1005.00 \pm 95.19$	$133.80 \pm 12.13$
GRB 051221A	5 <sup>b</sup>	HM	(11)	$14.04 \pm 1.06$	$29.90 \pm 4.66$	$9.20 \pm 1.51$	$67.56 \pm 10.47$
GRB 060614	$1.31^{+0.03}_{-0.03}$	HM	(12)	$9.72 \pm 0.11$	$14.30 \pm 0.32$	$3.89 \pm 0.31$	$0.42 \pm 0.02$
GRB 061121	1.16 <sup>b</sup>	HM	(13)	$3.94 \pm 0.30$	$2.36 \pm 0.37$	$71.67 \pm 11.46$	$53.35 \pm 8.32$
GRB 070125	3.78 <sup>b</sup>	HM	(14)	$4.94 \pm 0.37$	$3.71 \pm 0.58$	$474.00 \pm 74.85$	$108.20 \pm 16.58$
GRB 071010B	$3.44^{+0.39}_{-0.39}$	HM <sup>c</sup>	(15)	$9.22 \pm 0.41$	$12.90 \pm 1.16$	$18.72 \pm 2.71$	$8.55 \pm 1.06$
		WM		$8.12 \pm 0.30$	$10.00 \pm 0.74$	$14.50 \pm 1.61$	$6.62 \pm 1.22$
		WM		$3.41 \pm 0.07$	$1.77 \pm 0.08$	$278.10 \pm 12.20$	$21.00 \pm 1.30$
GRB 080319B	$11.6^{+1}_{-1}$	WM	(16), (12)	$10.73 \pm 4.13$	$17.50 \pm 16.00$	$190.20 \pm 149.00$	$59.56 \pm 46.09$
GRB 090328	$9^{+11.6}_{-0.11}$	HM	(17), (12)	$3.42 \pm 0.28$	$1.78 \pm 0.31$	$45.04 \pm 8.08$	$4.74 \pm 0.79$
GRB 090618	$0.5^{+0.11}_{-0.11}$	HM	(18)	$6.20 \pm 0.47$	$5.85 \pm 0.91$	$1234.00 \pm 188.70$	$549.80 \pm 82.86$
GRB 090926A	$10^{+2}_{-2}$	HM	(17), (12)	$4.46 \pm 0.09$	$3.02 \pm 0.13$	$4.82 \pm 0.63$	$3.45 \pm 0.29$
GRB 091127	$0.39^{+0.02}_{-0.02}$	HM <sup>c</sup>	(19)	$4.92 \pm 0.10$	$3.68 \pm 0.15$	$5.87 \pm 0.63$	$4.20 \pm 0.74$
		WM		$3.80 \pm 0.19$	$2.20 \pm 0.23$	$46.80 \pm 5.07$	$42.85 \pm 4.31$
		WM		$2.87 \pm 0.10$	$1.26 \pm 0.09$	$26.71 \pm 1.93$	$24.46 \pm 2.28$
GRB 110503A	$1.06^{+0.14}_{-0.14}$	HM <sup>c</sup>	(20)	$2.91 \pm 0.13$	$1.29 \pm 0.12$	$114.80 \pm 10.09$	$35.64 \pm 3.11$
GRB 130427A	$0.43^{+0.05}_{-0.05}$	HM	(21)	$6.43 \pm 0.23$	$6.29 \pm 0.46$	$1.23 \pm 0.10$	$18.79 \pm 1.37$
GRB 130603B	$0.47^{+0.02}_{-0.06}$	HM <sup>c</sup>	(22)	$8.90 \pm 0.24$	$12.00 \pm 0.66$	$2.36 \pm 0.13$	$36.00 \pm 3.00$
		WM		$6.08 \pm 0.36$	$5.63 \pm 0.68$	$18.60 \pm 2.74$	$4.41 \pm 0.73$
GRB 151027A	2.3 <sup>b</sup>	WM	(23)				

#### Notes.

<sup>a</sup> In cases where two references are given, the first one corresponds to the  $t_{\text{jet}}$  estimate and the second one corresponds to the preferred CBM.

<sup>b</sup> When no  $t_{\text{jet}}$  uncertainty is available from the literature, we take the sample-mean  $\sim 0.2 \cdot t_{\text{jet}}$  as a 68%  $t_{\text{jet}}$  error for the calculations.

<sup>c</sup> In cases where no preferred CBM density profile is available from the literature, we provide the estimates for both HM and WM.

**References.** (1) Zeh et al. (2006), (2) Masetti et al. (2000), (3) Björnsson et al. (2001), (4) Berger et al. (2000), (5) Galama et al. (2003), (6) Price et al. (2003), (7) Resmi et al. (2005), (8) Ghirlanda et al. (2007), (9) Blustin et al. (2006), (10) Cenko et al. (2006), (11) Soderberg et al. (2006), (12) Schulze et al. (2011), (13) Page et al. (2007), (14) Chandra et al. (2008), (15) Kann et al. (2007), (16) Tanvir et al. (2010a), (17) Cenko et al. (2011), (18) Cano et al. (2011), (19) Filgas et al. (2011), (20) Kann et al. (2011), (21) Maselli et al. (2014), (22) Fong et al. (2014), (23) Nappo et al. (2017).

(This table is available in its entirety in machine-readable form.)

The jet opening angles vary from  $1^{\circ}9$  to  $25^{\circ}5$  and the corresponding collimation factors from  $5.5 \times 10^{-4}$  to 0.098. The brightest KW GRB in terms of both  $E_{\gamma}$  and  $L_{\gamma}$  is GRB 090926A ( $E_{\gamma} \simeq 1.23 \times 10^{52}$  erg,  $L_{\gamma} \simeq 5.50 \times 10^{51}$  erg s $^{-1}$ ,  $\theta_{\text{jet}} \simeq 6^{\circ}20$ ). The distributions of  $E_{\gamma}$  and  $L_{\gamma}$  are shown in Figure 6 and Table 6 provides descriptive statistics of the GRB parameters estimated in Section 4.

## 5. Discussion

### 5.1. This Catalog versus Previously Reported KW Results

Preliminary results on the KW detections of bursts with known redshifts have been reported in more than 100 GCN circulars and the more detailed KW GRB analyses were presented in multiple refereed publications. Although the

**Table 6**  
Parameter Statistics

Parameter Name	Min Value	Max Value	Mean Value	Median Value
Redshift	0.096	5	1.50	1.32
$T_{100}$ (s)	0.124	484.858	67.689	37.312
$T_{90}$ (s)	0.070	440.826	46.557	21.664
$T_{50}$ (s)	0.034	167.290	16.959	7.616
$T_{100,z}$ (s)	0.088	170.884	29.476	13.974
$T_{90,z}$ (s)	0.052	121.954	19.447	9.677
$T_{50,z}$ (s)	0.025	49.733	7.220	3.002
$\tau_{\text{lagG2G1}}$ (ms)	0.6	2495	292	150
$\tau_{\text{lagG3G1}}$ (ms)	4.8	5106	543	343
$\tau_{\text{lagG3G2}}$ (ms)	2.1	765	176	132
$\tau_{\text{lagG2G1,z}}$ (ms)	0.4	1290	143	68
$\tau_{\text{lagG3G1,z}}$ (ms)	3.7	2630	257	133
$\tau_{\text{lagG3G2,z}}$ (ms)	1.4	388	85	68
$E_{p,i}$ (keV), Type I GRBs	468	3516	953	640
$E_{p,p}$ (keV) Type I GRBs	468	3386	966	671
$E_{p,i,z}$ (keV) Type I GRBs	658	6691	1637	988
$E_{p,p,z}$ (keV) Type I GRBs	658	6444	1647	991
$E_{p,i}$ (keV) Type II GRBs	37	1083	298	238
$E_{p,p}$ (keV) Type II GRBs	37	1511	360	271
$E_{p,i,z}$ (keV) Type II GRBs	54	2703	775	661
$E_{p,p,z}$ (keV) Type II GRBs	53	5137	931	752
$S$ (erg cm $^{-2}$ )	$1.13 \times 10^{-6}$	$2.86 \times 10^{-3}$	$1.07 \times 10^{-4}$	$2.51 \times 10^{-5}$
$F_{\text{peak},1024}$ (erg cm $^{-2}$ s $^{-1}$ )	$5.56 \times 10^{-7}$	$5.08 \times 10^{-4}$	$1.42 \times 10^{-5}$	$3.45 \times 10^{-6}$
$F_{\text{peak},64}$ (erg cm $^{-2}$ s $^{-1}$ )	$9.51 \times 10^{-7}$	$9.02 \times 10^{-4}$	$2.55 \times 10^{-5}$	$6.19 \times 10^{-6}$
$F_{\text{peak},64,r}$ (erg cm $^{-2}$ s $^{-1}$ )	$6.89 \times 10^{-7}$	$8.71 \times 10^{-4}$	$2.33 \times 10^{-5}$	$5.41 \times 10^{-6}$
$E_{\text{iso}}$ (erg)	$4.18 \times 10^{49}$	$5.81 \times 10^{54}$	$5.55 \times 10^{53}$	$1.93 \times 10^{53}$
$L_{\text{iso}}$ (erg s $^{-1}$ )	$2.94 \times 10^{50}$	$4.65 \times 10^{54}$	$2.55 \times 10^{53}$	$8.32 \times 10^{52}$
Collimation factor	$5.4 \times 10^{-4}$	$3.0 \times 10^{-2}$	$6.5 \times 10^{-3}$	$3.2 \times 10^{-3}$
$E_{\gamma}$ (erg)	$1.70 \times 10^{49}$	$1.23 \times 10^{52}$	$1.04 \times 10^{51}$	$3.98 \times 10^{50}$
$L_{\gamma}$ (erg s $^{-1}$ )	$4.22 \times 10^{48}$	$5.50 \times 10^{51}$	$4.39 \times 10^{50}$	$1.62 \times 10^{50}$

latter results are, with a few exceptions, statistically consistent with those reported here, the main advantage of this catalog, in comparison to the previous work, is in the use of the unified, systematic approach to re-analyse all 150 bursts in the sample. Particularly, GRB durations were calculated in the G2+G3 band that is less affected by the hard X-ray background variations; this also allows one to separate the hard GRB prompt emission from the emerging X-ray afterglow. The spectral analysis presented here gains an advantage from the most recent and accurate KW DRM; it also relies on a standard procedure for the TI spectrum interval selection based on  $T_{100}$ . The burst energetics,  $S$  and  $F_{\text{peak}}$  are estimated, in this work, based on the BEST spectral models for TI and peak spectra, which also improves the flux calculation uncertainties. Finally, the reported rest-frame energetics rely on the  $k$ -correction procedure that utilizes the full spectral band of the instrument, and they are estimated using a common set of cosmology parameters. To summarize, the results presented in this catalog form a consistent set of observer- and rest-frame GRB parameters useful for further systematic studies.

## 5.2. Observer-frame Spectral Parameters

### 5.2.1. The Sample Statistics and Comparison of KW with BATSE and GBM Bursts

Although this catalog covers only a limited subset of the KW-detected GRBs ( $\approx 7.5\%$  for the time span covered), a discussion of the derived spectral parameter distributions may be useful for the sample characterization.

Among 138 TI spectra of long (Type II) GRBs, 83 are best fit with the CPL model, 54 with the BAND function, and for one GRB both “curved” models failed. Similar fractions of the BEST models were obtained for the peak spectra: 86 CPL, 51 BAND, and one PL. We found the peak spectra to be harder, in terms of  $E_p$ , as compared to the TI spectra for  $>80\%$  of the Type II GRBs, consistent with the well-known GRB hardness–intensity correlation (or “Golenetskii” relation; Golenetskii et al. 1983). Median values for the BEST model  $E_p$  are 297 keV and 357 keV for the TI and the peak spectra, respectively. The corresponding median  $\alpha$  values are  $-1.00$  and  $-0.87$ , and the median  $\beta$  values are  $-2.45$  and  $-2.33$ .

The case where both “curved” models result in ill-constrained fits is the relatively weak GRB 080413B. For this burst, the KW PL slope is  $-2.00 \pm 0.1$  ( $\chi^2 = 49/61$  d.o.f.), suggesting a low

$E_p$  value. This PL slope is consistent with that derived with *Swift*-BAT/*Suzaku*-WAM joint fit ( $-1.92 \pm 0.06$ ; Krimm et al. 2009). The best spectral model for this GRB reported by Krimm et al. (2009) is the Band function with  $\alpha \simeq -1.24$ ,  $\beta \simeq -2.77$ , and  $E_p \simeq 67$  (and this model is also compatible with the KW data,  $\chi^2 = 53/62$  d.o.f.<sup>7</sup>), that yields  $E_{\text{iso}} = (2.09 \pm 0.28) \times 10^{52}$  erg. Thus, the KW  $E_{\text{iso}} = (3.33 \pm 0.61) \times 10^{52}$  erg derived for GRB 080413B from the PL fit is overestimated by a factor of  $\sim 1.6$  as compared to the more precise result of the joint BAT/WAM analysis.

Of 150 GRBs in the sample, 12 (or 8%) are classified as short/hard (Type I) bursts. This fraction is one-half that for all KW GRBs (S16), thus reflecting the complexity of their optical identifications and redshift measurements. All spectra of the Type I GRBs from this catalog are fitted best by the CPL function, with median  $\alpha = -0.53$  and median  $E_p = 640$  keV. These results are consistent with the BEST model and the spectral parameter statistics for 293 KW short GRBs given in S16.

We compared the BEST spectral parameter statistics for the whole sample with those for the BATSE 5B (Goldstein et al. 2013) and *Fermi*-GBM (Gruber et al. 2014) catalogs. We found the KW mean and median parameter values, for both spectral models and for both TI and peak spectra, consistent, within 68% confidence intervals, with the statistics given in these catalogs. Meanwhile, we noticed some systematic differences between the instruments, e.g., the KW spectra are typically harder, in terms of  $E_p$ , than BATSE and GBM ones. The same is true when comparing the low-energy spectral indices: the KW  $\alpha$  are, on average, shallower than those reported for BATSE and GBM. Finally, the typical KW  $\beta$  are shallower than the BATSE  $\beta$ , but they are steeper when compared to the typical GBM indices. These systematic differences may be explained by the different spectral ranges of the instruments: the KW upper spectral limit ( $\sim 10$ – $15$  MeV) is higher than that of BATSE ( $\sim 2$  MeV), thus allowing for high  $E_p$  to be constrained better. In turn, the broad range of the GBM BGO detectors (up to  $\sim 30$  MeV) may result, for the BAND spectra, in better constrained  $\beta$  and, simultaneously, smaller  $E_p$ , when compared to the typical KW parameters. The KW-GBM spectral cross-calibration over a large sample of simultaneously observed GRBs is currently underway that will provide a more detailed analysis of the instrumental effects that could be affecting the scientific results from the GRB prompt emission data.

It also should be noted that the mean  $E_p$  for the KW sample is beyond the *Swift*-BAT energy range (15–150 keV), thus emphasizing the importance of the KW detections of *Swift* GRBs.

### 5.2.2. Spectral Indices

The difference between low- and high-energy photon indices,  $(\alpha-\beta)$ , may be helpful when investigating GRB emission processes in the framework of the synchrotron shock model (SSM) through comparing the observational and theoretical values of  $(\alpha-\beta)$  to constrain the synchrotron cooling regime and infer the electron power-law index (Preece et al. 2002). The  $(\alpha-\beta)$  distribution for TI and peak spectra fitted with the BAND model is shown in Figure 5 (panel c). The fact that no obvious peak in the distributions is seen may

imply a diversity of electron power-law indices and/or different SSM cases at the burst sources. The median values of  $(\alpha-\beta)$  are 1.5 and 1.6 for the TI and the peak spectra, respectively. The peak spectrum distribution is slightly shifted toward the higher values in comparison with the TI spectrum one.

Additionally, we estimated the fraction of the bursts which violate the  $-2/3$  synchrotron “line-of-death” (see Preece et al. 1998 for details) and the  $-3/2$  synchrotron cooling limit. We found that the 68% confidence intervals (CIs) for the BEST model alpha lie completely above the  $-2/3$  synchrotron “line-of-death” for about 8% of the TI and 21% of the peak spectra; also, the 68% CIs lie completely below the  $-3/2$  synchrotron cooling limit for the 5% of the TI and 2% of the peak spectra.

### 5.3. Selection Effects

Selection effects are distortions or biases that usually occur when the observational sample is not representative of the true, underlying population. They play a crucial role for GRBs (Turpin et al. 2016; Dainotti & Del Vecchio 2017), which are particularly affected by the Malmquist bias effect that favors the brightest objects against faint objects at large distances, and these biases have to be taken into account when using GRBs as distance estimators, cosmological probes, and model discriminators.

For the sample of the KW triggered-mode GRBs with known redshifts, the selection effects fall into two categories: the KW-specific effects, caused by its trigger sensitivity to the burst prompt emission parameters; and the “external” biases arising in the process of localization and securing GRB redshifts, which are outside of the scope of this paper.

The KW triggered mode is activated when the count rate in the G2 window exceeds a  $\sim 9\sigma$  threshold above the background on one of two fixed timescales  $\Delta T_{\text{trig}}$ , 1 s (applicable, with a few exceptions, to Type II bursts in our sample) or 140 ms (the Type I bursts). Thus, the burst’s detection significance may be characterized by a PCR to background statistical uncertainty ratio (over the corresponding  $\Delta T_{\text{trig}}$ ). Although the KW trigger criterion cannot be easily translated into the GRB prompt emission characteristics (e.g., duration, rise-time, spectral shape, or energy flux), an investigation into how their combination may affect the trigger sensitivity to a specific burst may be done indirectly.

We estimated the energy flux sensitivity of the KW detectors following the methodology described in Band (2003). Figure 7 presents the limiting energy flux (10 keV–10 MeV) as a function of  $E_p$  for  $\Delta T_{\text{trig}} = 1$  s, for a burst incident angle  $60^\circ$ , and the S1 detector calibration as of mid-2015. As can be seen, the energy flux threshold under these assumptions is  $\approx 1 \times 10^{-6}$  erg cm $^{-2}$  s $^{-1}$  and there is a bias against the detection of soft-spectrum bursts with  $E_p \lesssim 70$ – $80$  keV, especially with CPL spectra, due to the instrumental selection. Meanwhile, the  $F - E_p$  diagram stresses the lack of bright ( $F \gtrsim 5 \times 10^{-6}$  erg cm $^{-2}$  s $^{-1}$ ) and soft ( $E_p \lesssim 100$  keV) GRBs, that should be easily detectable with KW. Since the lower boundary of this region is defined by GRBs with moderate-to-high detection significance, the instrumental biases do not affect the sample from this edge of the distribution. Thus, the apparent lack of soft/bright burst observations in the KW sample is likely due to an intrinsic GRB property (see Section 5.7 for more discussion).

<sup>7</sup> The statistic is estimated with fixed  $\alpha$ ,  $\beta$ , and  $E_p$ .

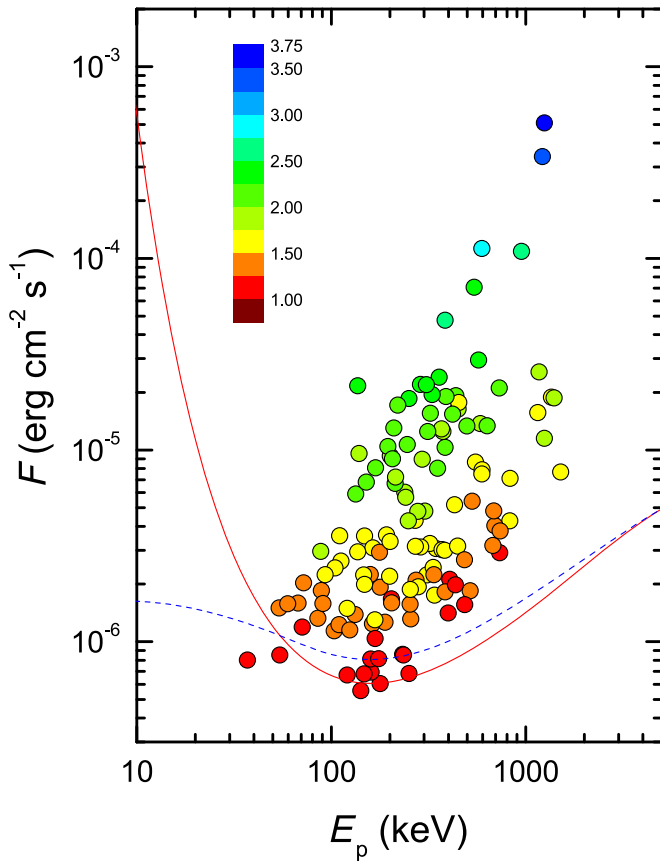


**Figure 7.** Dependence of the limiting KW energy flux (10 keV–10 MeV) on  $E_p$ . Calculated trigger sensitivities for CPL ( $\alpha = -1$ ) and Band ( $\alpha = -1$ ,  $\beta = -2.5$ ) spectra are plotted with solid red and dashed blue lines, respectively.  $F_{\text{peak},1024}$  (10 keV–10 MeV) vs.  $E_{p,p}$  for Type II bursts from the sample is shown by circles. The color of each data point represents the log of the burst’s trigger significance ( $\sigma$ ).

In a similar way, we calculated a limiting observer-frame energy flux for each GRB from the sample using its BEST-model spectral parameters, incident angle, and detector calibration. In order to make the results more helpful for the rest-frame energy calculations, we applied  $k$ -corrections (Section 4.3) to these values using the burst redshift. The resulting bolometric limiting fluxes,  $F_{\text{lim}}$ , are given in Table 4; the sample mean value of  $F_{\text{lim}}$  for the Type II GRBs is  $1.08 \times 10^{-6} \text{ erg cm}^{-2} \text{ s}^{-1}$ . We note that  $F_{\text{lim}}$  are calculated using the 1 s scale; when compared to peak fluxes determined on a different  $\Delta T$  they should be adjusted as:

$$F_{\text{lim}}(\Delta T) = \frac{F_{\text{peak}}(\Delta T)}{F_{\text{peak},1024}} F_{\text{lim}}.$$

Figure 8 shows the KW GRB distributions in the  $E_{\text{iso}}-z$ ,  $L_{\text{iso}}-z$ , and  $E_{p,z}-z$  diagrams. The region in the  $L_{\text{iso}}-z$  plane above the limit corresponding to  $F_{\text{lim}} \sim 1 \times 10^{-6} \text{ erg cm}^{-2} \text{ s}^{-1}$  may be considered free from the selection bias. In the  $E_{\text{iso}}-z$  plane, the selection-free region lies above the limit, corresponding to the bolometric fluence  $S_{\text{lim}} \sim 3 \times 10^{-6} \text{ erg cm}^{-2}$ . As mentioned above, the KW detector sensitivity drops rapidly as  $E_p$  approaches the lower boundary of the instrument’s band ( $\sim 20$ – $25 \text{ keV}$  as of 2015), and this results in a lack of bursts below  $E_{p,z,\text{lim}} \approx (1+z)^2 \cdot 25 \text{ keV}$  in the  $E_{p,z}-z$  plane; the additional factor  $(1+z)$  here is due to cosmological time dilation.

Finally, our sample does not exhibit any direct selection effects due to GRB duration. However, some bursts with very gradual rising slopes may not trigger the instrument despite being bright enough to do it in other circumstances. We estimate the number of such GRBs with known redshifts to be  $\lesssim 5$  (as of mid-2016); these bursts will be considered, along with other KW background-mode GRBs with known redshifts, in the second part of the catalog.

#### 5.4. KW GRB Detection Horizon

Knowing the maximum distance at which a particular GRB can be detected by the instrument (the GRB “horizon,”  $z_{\text{max}}$ ) may be useful in a number of applications, e.g., for deriving the  $V/V_{\text{max}}$  statistic (Schmidt et al. 1988) or for accounting for the instrumental bias when studying the “true” GRB energy distribution (Atteia et al. 2017).

A common approach to estimate the GRB horizon is to find a redshift  $z_{\text{max,L}}$ , at which the limiting isotropic luminosity  $L_{\text{iso,lim}} = 4\pi D_L^2 \times F_{\text{lim}}$ , defined by the limiting energy flux estimated for the whole sample (the “monolithic”  $F_{\text{lim}}$ ), starts to exceed the GRB  $L_{\text{iso}}$ . The KW trigger, however, is based on a simple photon-counting algorithm and not directly sensitive to the incident energy flux. Thus, the correctness of the described approach (hereafter the monolithic  $F_{\text{lim}}$  method), which doesn’t account for the burst-specific instrumental issues, such as trigger sensitivity to the GRB incident angle, its light-curve shape, and the shape of the energy spectrum, needs an additional confirmation.

When evaluating how GRB detectability by KW changes when the burst source is shifted from its redshift  $z$  to a more distant  $z'$ , at least three effects have to be accounted for. First, the solid angle factor, which reduces (assuming identical beaming) an incident bolometric photon flux  $P$  by  $(D_M(z)/D_M(z'))^2$ , where  $D_M$  is the transverse comoving distance. Second, the cosmological time dilation, which results in the light curve broadening and an additional decrease in  $P$  by a factor of  $(1+z')/(1+z)$ . Finally, the spectral cutoff, which is inherent to GRB spectra, is redshifted by the same factor, thus decreasing the fraction of  $P$  within the instrument trigger band (G2). We estimate the KW detection horizon as a redshift  $z' = z_{\text{max}}$ , at which the PCR in the G2 light curve drops below the trigger threshold ( $9\sigma$ ) on both KW trigger scales  $\Delta T_{\text{trig}}$  (140 ms and 1 s).  $\text{PCR}_{z'}(\Delta T_{\text{trig}})$  is calculated as

$$\text{PCR}_{z'}(\Delta T_{\text{trig}}) = a \times \text{PCR}_z(a \cdot \Delta T_{\text{trig}}) \times \frac{N_{\text{G2}}(\alpha, \beta, a \cdot E_{p,p})}{N_{\text{G2}}(\alpha, \beta, E_{p,p})} \times \left( \frac{D_M(z)}{D_M(z')} \right)^2, \quad (5)$$

where  $a = (1+z)/(1+z')$ ;  $\text{PCR}_z(a \cdot \Delta T_{\text{trig}})$  is the PCR reached in the observed G2 light curve on the modified timescale;  $N_{\text{G2}}(\alpha, \beta, E_{p,p})$  is the BEST spectral model count flux in G2 calculated using the DRM; and  $N_{\text{G2}}(\alpha, \beta, a \cdot E_{p,p})$  is the corresponding flux in the redshifted spectrum. The resulting values of  $z_{\text{max}}$  are given in Table 4 and shown in Figure 9. We found that for both Type I and Type II GRBs,  $z_{\text{max}}$  are distributed narrowly around the corresponding  $z_{\text{max,L}}$  values calculated assuming the bolometric  $F_{\text{lim}} = 1 \times 10^{-6} \text{ erg cm}^{-2} \text{ s}^{-1}$  with the mean and  $\sigma$  of the  $(1+z_{\text{max}})/(1+z_{\text{max,L}})$  distribution of 1.01 and 0.12, respectively. Although in some cases  $z_{\text{max,L}}$  calculated with the simple monolithic  $F_{\text{lim}}$  method may differ from the more precisely evaluated  $z_{\text{max}}$  by a factor of  $\sim 1.5$ , our



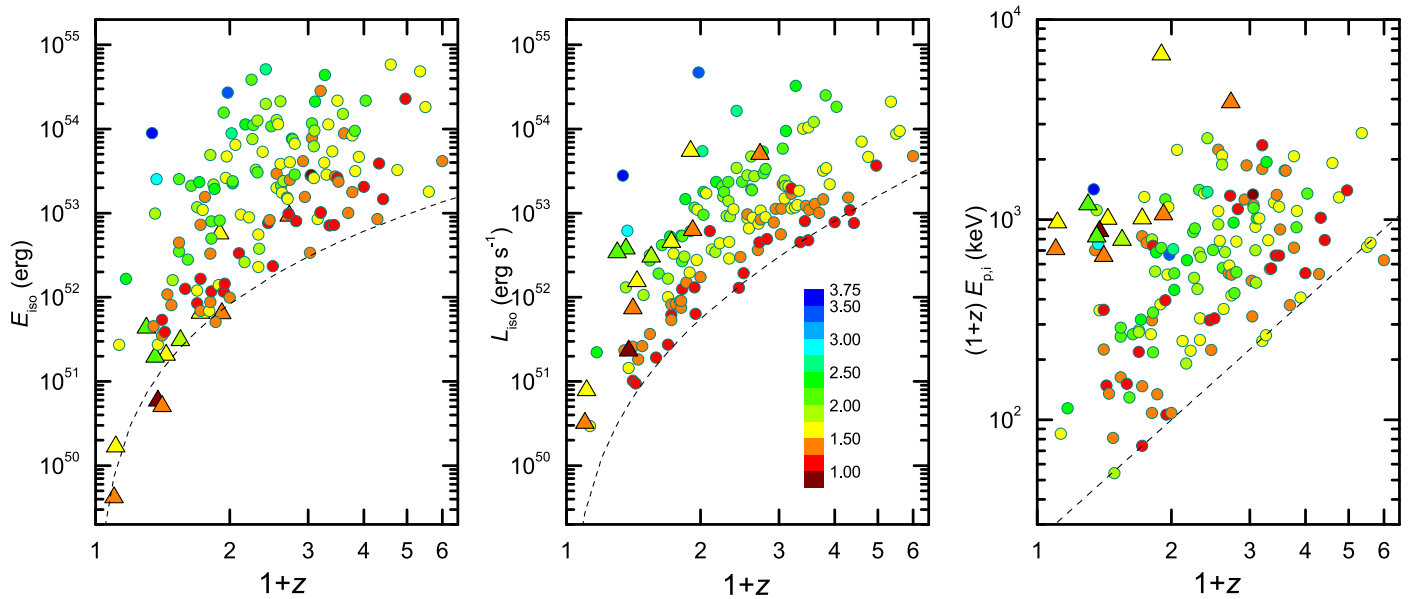


**Figure 8.** KW GRB  $E_{\text{iso}}$ ,  $L_{\text{iso}}$ , and  $E_{p,i,z}$  vs. redshift. The color of each data point (Type I: triangles, Type II: circles) represents the log of the burst’s trigger significance ( $\sigma$ ). The observer-frame limits (Section 5.3) are shown with dashed lines.

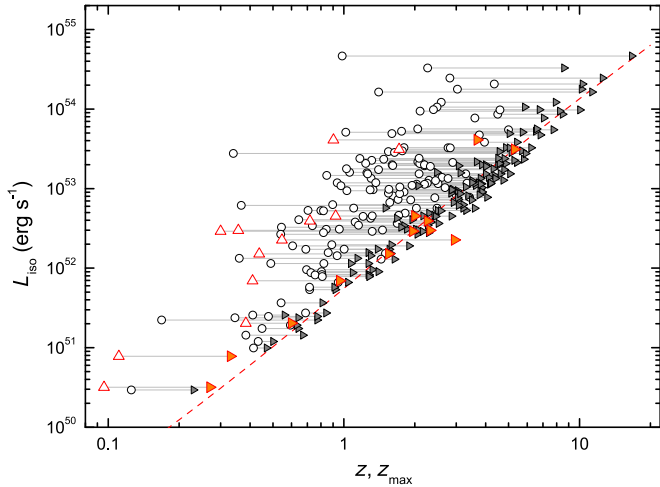


**Figure 9.** KW GRB detection horizons plotted in the  $L_{\text{iso}}-z$  plane. The solid lines connect GRBs from the sample (Type I: open triangles, Type II: open circles) and their detection horizons  $z_{\text{max}}$  (filled symbols) assuming identical beaming. The limiting redshift  $z_{\text{max},L}$  defined by  $F_{\text{lim}} = 1 \times 10^{-6} \text{ erg cm}^{-2} \text{ s}^{-1}$  is shown by the dashed line.

calculations support the general correctness of the former approach.

The most distant GRB horizon for the KW sample ( $z_{\text{max}} \approx 16.6$ ) is reached for the ultra-luminous GRB 110918A<sup>8</sup> at  $z = 0.981$  and the second-highest ( $z_{\text{max}} \approx 12.5$ ) is for GRB 050603 ( $z = 2.82$ ). At  $z \approx 16.6$ , the age of the universe amounts to only  $\sim 230$  Myr, i.e., a burst that occurred close to the end of the cosmic Dark Ages could still trigger the KW detectors, and a thorough temporal and spectral analysis in a wide observer-frame energy range could be performed. Among the KW Type I GRBs, the highest  $z_{\text{max}} \approx 5.3$  is for GRB 160410A ( $z = 1.72$ ).

<sup>8</sup> We found that  $z_{\text{max}} \approx 7.5$  previously reported for this GRB by Frederiks et al. (2013) was miscalculated due to use of  $D_L = (1+z)D_M$  instead of  $D_M$  in Equation (5). As a result, the  $\text{PCR}_{z'}$  was underestimated by a factor of  $a^2$ .

### 5.5. GRB Luminosity and Isotropic-energy Functions, GRB Formation Rate

Among various statistical parameters, the luminosity function as well as the cosmic formation rate of GRBs are particularly interesting. The luminosity function (LF) is a measure of the number of bursts per unit luminosity, that provides information on the energy release and emission mechanism of GRBs. The cosmic GRB formation rate (GRBFR) is a measure of the number of events per comoving volume and time, which can help us to understand the production of GRBs at various stages of the universe. While LF was originally used to study long-lasting and relatively stable astrophysical phenomena, such as stars and galaxies, the isotropic energy release function (EF, the number of bursts per unit  $E_{\text{iso}}$ ) can be more representative for transient phenomena, e.g., for GRBs. The GRB EF was constructed for the first time by Wu et al. (2012) using a sample of 95 bursts with measured redshifts. The KW sample presented in this catalog provides an excellent opportunity to test GRB LF, EF, and GRBFR on an independent data set.

Without loss of generality, the total LF  $\Phi(L_{\text{iso}}, z)$ <sup>9</sup> can be rewritten as  $\Phi(L_{\text{iso}}, z) = \rho(z)\phi(L_{\text{iso}}/g(z), \alpha_s)/g(z)$ , where  $\rho(z)$  is the GRB formation rate (GRBFR),  $\phi(L_{\text{iso}}/g(z))$  is the local LF,  $g(z)$  is the luminosity evolution that parameterizes the correlation between  $L$  and  $z$ , and  $\alpha_s$  is the shape of the LF, whose effect is commonly ignored as the shape of the LF does not change significantly with  $z$  (e.g., Yonetoku et al. 2004). Following Lloyd-Ronning et al. (2002), Yonetoku et al. (2004), Wu et al. (2012), and Yu et al. (2015) we chose the functional form of  $g(z) = (1+z)^6$  for the luminosity evolution. It should be noted that the isotropic luminosity evolution can be determined by either the evolution of the amount of energy per unit time emitted by the GRB progenitor or by the jet opening angle evolution (see, e.g., Lloyd-Ronning et al. (2002) for the discussion); we tested the KW sample for a correlation between the collimation factor and  $z$  and found the correlation

<sup>9</sup> Similar reasoning may be applied to the total EF  $\Psi(E_{\text{iso}}, z)$ .

negligible (the Spearman rank-order correlation coefficient  $\rho_S = -0.26$  (the corresponding  $p$  value  $P_{\rho_S} = 0.17$ ) for the subsample of 30 Type II bursts with known collimation factors).

The KW  $z-L_{\text{iso}}$  and  $z-E_{\text{iso}}$  samples suffer from selection effects due to the detection limit of the instrument (see Section 5.3 for details) that results in data truncation seen in Figure 8. To estimate LF, EF, and GRBFR for the sample of 137 KW Type II bursts we used the non-parametric Lynden-Bell  $C^-$  technique (Lynden-Bell 1971) further advanced by Efron & Petrosian (1992) (the EP method); the details of our calculations are described in the Appendix. The EP method is specifically designed to reconstruct the intrinsic distributions from the observed distributions, which accounts for the data truncations introduced by observational bias and includes the effects of the possible correlation between the two variables.

Applying the EP technique based on the individual (i.e., calculated for each burst independently) truncation limits to the  $z-L_{\text{iso}}$  plane, we found that the independence of the variables is rejected at  $\tau_0 \equiv \tau(\delta = 0) \sim 1.7$  (where  $\tau$  is a modified version of the Kendall statistic, see the Appendix), and the best luminosity evolution index is  $\delta_L = 1.7^{+0.9}_{-0.9}$  ( $1\sigma$  CL). Similar results were obtained using the “monolithic” truncation limit  $F_{\text{lim}} = 2 \times 10^{-6} \text{ erg cm}^{-2} \text{ s}^{-1}$ :  $\tau_0 \sim 1.2$  and  $\delta_L = 1.7^{+0.9}_{-1.1}$ .

Applying the same method to the  $z-E_{\text{iso}}$  plane and using the monolithic truncating fluence  $S_{\text{lim}} = 4.3 \times 10^{-6} \text{ erg cm}^{-2}$  (see the Appendix for the details of  $F_{\text{lim}}$  and  $S_{\text{lim}}$  selection), we found that the independence of the variables is rejected at  $\sim 1.6\sigma$ , and the best isotropic energy evolution index is  $\delta_E = 1.1^{+1.5}_{-0.7}$ . Thus, the estimated  $E_{\text{iso}}$  and  $L_{\text{iso}}$  evolutions are comparable. The evolution PL indices  $\delta_L$  and  $\delta_E$  derived here are shallower than those reported in the previous studies:  $\delta_L = 2.60^{+0.15}_{-0.20}$  (Yonetoku et al. 2004),  $\delta_L = 2.30^{+0.56}_{-0.51}$  (Wu et al. 2012),  $\delta_L = 2.43^{+0.41}_{-0.38}$  (Yu et al. 2015), and  $\delta_E = 1.80^{+0.36}_{-0.63}$  (Wu et al. 2012), albeit within errors.

After eliminating the luminosity and energy release evolution, we, following Lynden-Bell (1971), obtained the local cumulative LF and EF,  $\psi(L')$  and  $\psi(E')$ , where  $L' = L_{\text{iso}}/(1+z)^{\delta_L}$  and  $E' = E_{\text{iso}}/(1+z)^{\delta_E}$ . We approximated the variance of  $\psi(L')$  and  $\psi(E')$  by bootstrapping the initial sample and fitted the distributions with a broken power-law (BPL) function:

$$\psi(x) \propto \begin{cases} x^{\alpha_1}, & x \leq x_b, \\ x_b^{(\alpha_1 - \alpha_2)} x^{\alpha_2}, & x > x_b, \end{cases}$$

where  $\alpha_1$  and  $\alpha_2$  are the PL indices at the dim and bright distribution segments and  $x_b$  is the breakpoint of the distribution, and with the CPL function<sup>10</sup>:  $\psi(x) \propto x^\alpha \exp(-x/x_{\text{cut}})$ , where  $x_{\text{cut}}$  is the cutoff luminosity (or energy).

The fits were performed in log–log space using  $\chi^2$  minimization, the results are given in Table 7 and shown in Figure 10 (right panel). The derived BPL slopes of LF and EF are close to each other, both for the dim and bright segments, thus the shape of EF is similar to that of LF; also, these indices are roughly consistent with the LF and EF slopes obtained in Yonetoku et al. (2004) and Wu et al. (2012). The small reduced  $\chi^2$  obtained for both models do not allow us to reject any of them; however, when compared to BPL, the CPL fit to  $\psi(L')$  results in a considerably worse quality ( $\chi^2_{\text{CPL}} - \chi^2_{\text{BPL}} > 16$ ); with the PL slope  $\alpha \sim -0.6$

and the cutoff luminosity  $L'_{\text{cut}} \sim 2.3 \times 10^{54} \text{ erg s}^{-1}$ . Conversely, the cutoff PL fits  $\psi(E')$  better when compared to BPL ( $\chi^2_{\text{CPL}} - \chi^2_{\text{BPL}} \sim -5.5$ ); with  $\alpha \sim -0.35$  and the cutoff energy  $E'_{\text{cut}} \sim 2.3 \times 10^{54} \text{ erg}$ . The existence of a sharp cutoff of the isotropic energy distribution of KW and *Fermi*-GBM GRBs around  $\sim (1-3) \times 10^{54} \text{ erg}$  was suggested recently by Atteia et al. (2017).

The derived  $\psi(L')$  and  $\psi(E')$  correspond to the present-time GRB luminosity and energy distributions (at  $z = 0$ ) and hence the local LF and EF in the comoving frame are roughly estimated as  $\psi(L')(1+z)^{\delta_L}$  and  $\psi(E')(1+z)^{\delta_E}$ , correspondingly. Taking into account that the  $z-L_{\text{iso}}$  and  $z-E_{\text{iso}}$  evolutions are established at  $< 2\sigma$ , the LF and EF calculated without accounting for the evolution,  $\psi(L_{\text{iso}})$  and  $\psi(E_{\text{iso}})$ , may be of interest. We estimated these functions by setting  $\delta_L$  and  $\delta_E$  to zero, and found them very similar in shape to the present-time LF and EF (Figure 10). The results of the BPL and CPL fits to  $\psi(L_{\text{iso}})$  and  $\psi(E_{\text{iso}})$  are given in the last four lines of Table 7.

Finally, using the EP method, we estimated the cumulative GRB number distribution  $\psi(z)$  and the derived GRBFR per unit time per unit comoving volume  $\rho(z)$  (see the Appendix for the details). In Figure 11, we compare the star formation rate (SFR) data from the literature (Hopkins 2004; Hanish et al. 2006; Thompson et al. 2006; Li 2008; Bouwens et al. 2011) with GRBFRs derived from different  $z-L$  and  $z-E$  distributions. The GRBFR estimated from the evolution-corrected  $z-L'$  distribution exceeds the SFR at  $z < 1$  and nearly traces the SFR at higher redshifts; the same behavior is noted for the GRBFRs estimated using both the evolution-corrected  $z-E'$  and the non-corrected  $z-E_{\text{iso}}$  distributions. The low- $z$  GRBFR excess over SFR is in agreement with the results reported in Yu et al. (2015) and Petrosian et al. (2015). Meanwhile, the only GRBFR that traces the SFR in the whole KW GRB redshift range is the  $\rho(z)$  derived from the  $z-L_{\text{iso}}$  distribution (i.e., not accounting for the luminosity evolution). Such behavior is known, e.g., from Wu et al. (2012), albeit for the GRBFR estimated from the  $z-E_{\text{iso}}$  distribution.

### 5.6. Hardness-duration Distribution in the Observer and Rest Frames

Figure 12 shows  $E_{p,i}$  as a function of the burst durations  $T_{90}$  in the observer and rest frames. In the observer frame the KW Type I GRBs are typically harder and shorter than Type II bursts, which is consistent with the classification obtained from the hardness–duration distribution (Figure 1), and this tendency shows no dependence on the burst redshift.

In the cosmological rest frame, this pattern remains practically unchanged for GRBs at  $z \lesssim 1.7$  but it appears to be less distinct when the whole sample is considered. Although in the rest frame Type I GRBs are still shorter than Type II GRBs, their rest-frame  $E_p$ , clustered around 1 MeV, are superseded by those of a significant fraction of the Type II population. The notable exceptions here are GRB 090510 and GRB 160410A, whose rest-frame peak energies exceed those of even the highest- $z$  Type II GRBs. We note, however, that the derived rest-frame durations are affected by a variable energy-dependant factor (Section 4.1) and the KW rest-frame  $E_p$  are subject to the observational bias (Section 5.3) thus an interpretation of the rest-frame hardness–duration distribution should be done with care.

<sup>10</sup> The CPL function definition is different here from that in Section 4.2.

**Table 7**  
LF and EF Fits with BPL and Cutoff PL

Data	Evolution (PL Index)	Model	$\chi^2$ (d.o.f.)	$\alpha_1$	$\alpha_2$	log $x_{b,52}$ (log $x_{cut,52}$ )
$\psi(L')$	$\delta_L = 1.7$	BPL	2.05 (133)	$-0.47 \pm 0.06$	$-1.05 \pm 0.11$	$0.27 \pm 0.12$
$\psi(L')$	$\delta_L = 1.7$	CPL	18.5 (134)	$-0.60 \pm 0.04$	...	$2.10 \pm 0.15$
$\psi(E')$	$\delta_E = 1.1$	BPL	19.2 (126)	$-0.36 \pm 0.01$	$-1.28 \pm 0.11$	$1.30 \pm 0.04$
$\psi(E')$	$\delta_E = 1.1$	CPL	12.7 (127)	$-0.31 \pm 0.02$	...	$2.09 \pm 0.04$
$\psi(L_{iso})$	no evolution	BPL	2.32 (133)	$-0.48 \pm 0.06$	$-1.00 \pm 0.10$	$0.96 \pm 0.15$
$\psi(L_{iso})$	no evolution	CPL	8.90 (134)	$-0.54 \pm 0.04$	...	$2.58 \pm 0.11$
$\psi(E_{iso})$	no evolution	BPL	17.2 (126)	$-0.35 \pm 0.01$	$-1.29 \pm 0.12$	$1.80 \pm 0.05$
$\psi(E_{iso})$	no evolution	CPL	15.4 (127)	$-0.32 \pm 0.01$	...	$2.63 \pm 0.04$

### 5.7. Hardness–Intensity Correlations

Using the data described in the previous sections, we tested KW GRB characteristics against  $E_{p,i}-S$  and  $E_{p,p}-F_{peak}$  correlations in the observer frame, and  $E_{p,i,z}-E_{iso}$  (“Amati”) and  $E_{p,p,z}-L_{iso}$  (“Yonetoku”) correlations in the rest frame, along with their collimated versions  $E_{p,i,z}-E_\gamma$  and  $E_{p,p,z}-L_\gamma$ .

To probe the existence of correlations, we calculated the Spearman rank-order correlation coefficients ( $\rho_s$ ) and the associated null-hypothesis (chance) probabilities or  $p$  values ( $P_{\rho_s}$ ; Press et al. 1992). The null hypothesis is that no correlation exists; therefore, a small  $p$  value indicates a significant correlation. It was shown that the Nukers’ estimate is an unbiased slope estimator for the linear regression (Tremaine et al. 2002). The Nukers’ estimate is based on minimizing:

$$\chi^2 = \sum_{i=1}^N \frac{(y_i - ax_i - b)^2}{a^2\sigma_{xi}^2 + \sigma_{yi}^2 + \sigma_{int}^2},$$

where  $\sigma_{xi}^2$  and  $\sigma_{yi}^2$  are the measurement errors; thus both variables are treated symmetrically in terms of their errors and there is no need to choose dependent and independent variables. Although a correlation may be highly significant, the reduced statistic,  $\chi_r^2$ , may be  $\gg 1$  indicating that either the uncertainties are underestimated or there is an intrinsic dispersion in the correlation. To account for the intrinsic dispersion, an additional term,  $\sigma_{int}^2$ , is added to the denominator and, in this case,  $\chi_r^2$  is adjusted to ensure  $\chi_r^2 = 1$ . Therefore, we approximated a linear regression between log-energy and log  $E_p$  using two methods, without  $\sigma_{int}$  and with the intrinsic scatter.

Table 8 summarizes the correlation parameters we obtained for subsamples of Type I GRBs, Type II GRBs, and Type II GRBs with  $t_{jet}$  estimates. The first column presents the correlation. The next three columns provide the number of bursts in the fit sample,  $\rho_s$ , and  $P_{\rho_s}$ . The next columns specify the slopes ( $a$ ), the intercepts ( $b$ ), and  $\sigma_{int}$ . Since zeroing the intrinsic scatter yields  $\chi_r^2 \gg 1$  for all the subsamples (and that confirms the relevance of accounting for  $\sigma_{int}$ ), their values are of little interest and we do not present the fit statistics in the table.

For the subsamples of Type I and Type II KW GRBs, both the Amati and Yonetoku correlations improve considerably when moving from the observer frame to the GRB rest frame ( $\Delta\rho_s \gtrsim 0.1$ ), with only marginal changes in the slopes. We found the rest-frame correlations for Type II bursts to be the

most significant, with  $P_{\rho_s} < 2 \times 10^{-21}$ . The derived slopes of the Amati and Yonetoku relations for those GRBs are very close to each other, 0.469 ( $\rho_s = 0.70$ , 138 GRBs) and 0.494 ( $\rho_s = 0.73$ , 137 GRBs), respectively. These values are in agreement with the original results of Amati et al. (2002) and Yonetoku et al. 2004 and their further improvements (e.g., Nava et al. 2012). When accounting for the intrinsic scatter, these slopes change to a more gentle  $\sim 0.35$  (with  $\sigma_{int} \sim 0.24$ ).

As one can see in Figure 13, the lower boundaries of both the Amati and Yonetoku relations are defined by GRBs with moderate-to-high detection significance, so the instrumental biases do not affect the correlations from this edge of the distributions. Meanwhile, all outliers in the relations lie *above* the upper boundaries of the 90% prediction intervals (PIs) of the relations. Since these bursts were detected at lower significance, with the increased number of GRB redshift observations, one could expect a “smear” of the hardness–intensity correlations due to more hard-spectrum/less-energetic GRB detections. Thus, using the KW sample, we confirm a finding of Heussaff et al. (2013) that the lower right boundary of the Amati correlation (the lack of luminous soft GRBs) is an intrinsic GRB property, while the top left boundary may be due to selection effects. This conclusion may also be extended to the Yonetoku correlation.

The collimated versions of these relations were tested on the subsample of 30 Type II GRBs with reliable  $t_{jet}$  (last four lines of Table 8). We found that accounting for the jet collimation for the KW sample neither improves the significance of the correlations nor reduces the dispersion of the points around the best-fit relations. The slopes we obtained for the collimated Amati and Yonetoku relations are steeper compared to those of the non-collimated versions.

The  $E_{p,i,z}-E_{iso}$  and  $E_{p,p,z}-L_{iso}$  correlations for 12 Type I bursts are less significant when compared to those for Type II GRBs, and they are characterized by less steep slopes (0.364 and 0.396 for  $E_{p,i,z}-E_{iso}$  and  $E_{p,p,z}-L_{iso}$ , respectively). It should be noted, however, that the rest-frame  $E_{p,i}$  of Type I GRBs shows only a weak (if any) dependence on the burst energy below  $E_{iso} \sim 10^{52}$  erg (Figure 13), and the same is true for the  $E_{p,p,z}-L_{iso}$  relation at  $L_{iso} \lesssim 5 \times 10^{52}$  erg s $^{-1}$ . Above these limits the slopes of both relations for Type I GRBs are similar to those for Type II GRBs. As one can see from the figure, all KW Type I bursts are hard-spectrum/low-isotropic-energy outliers in the Amati relation for Type II GRBs. In the  $E_{p,p,z}-L_{iso}$  plane, this pattern is less distinct; at luminosities above  $L_{iso} \sim 10^{52}$  erg s $^{-1}$  the Type I bursts nearly follow the upper boundary of the Type II GRB Yonetoku relation. Finally,

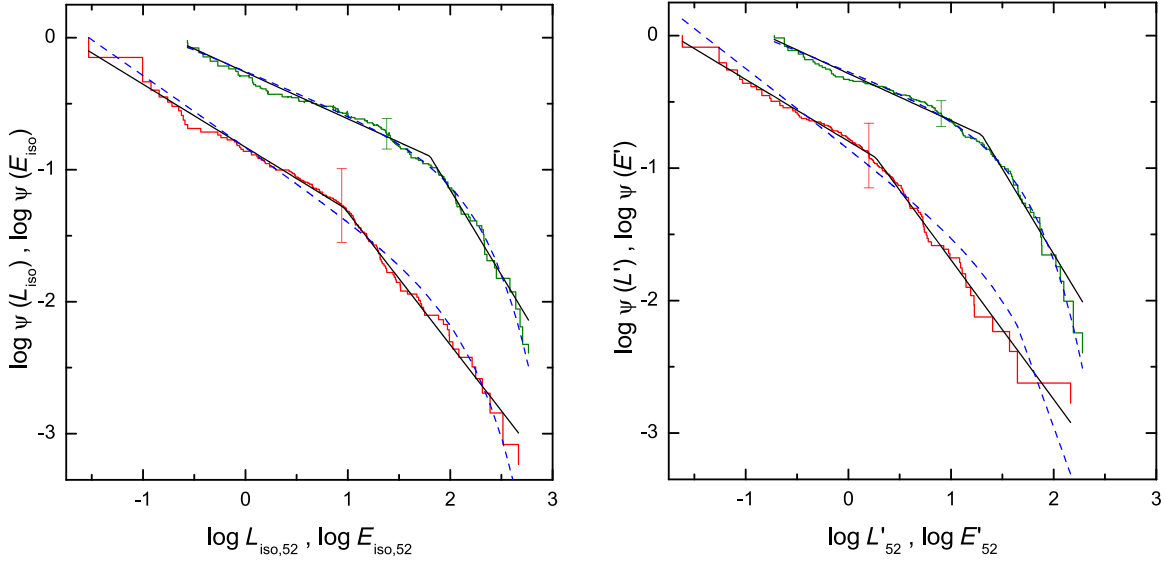


**Figure 10.** Cumulative GRB isotropic-luminosity and isotropic-energy functions. Left panel: LF (red stepped graph) and EF (green stepped graph) estimated under the assumption of no evolution of  $L_{\text{iso}}$  and  $E_{\text{iso}}$  with  $z$ ; the solid and dashed lines show the best BPL and CPL fits, respectively. Right panel: present-time LF and EF estimated accounting for the luminosity and energy evolutions:  $L' = L_{\text{iso}}/(1+z)^{1.7}$ ,  $E' = E_{\text{iso}}/(1+z)^{1.1}$ . The distributions are normalized to unity at the dimmest points and a typical error bar is shown for each distribution.

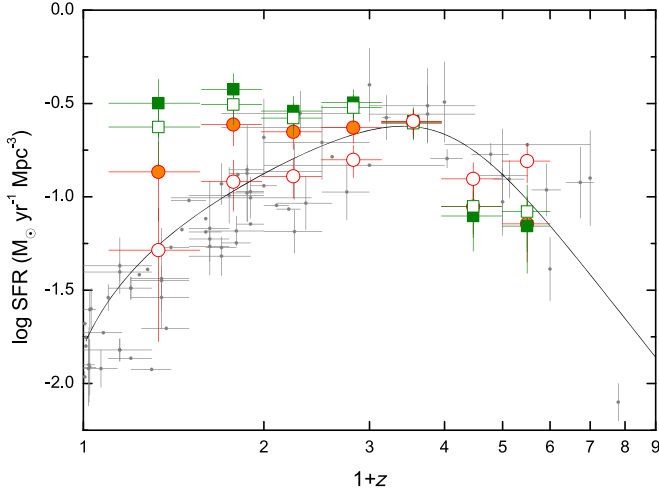


**Figure 11.** Comparison of the derived GRBFR and the SFR data from the literature. The GRBFR was calculated using four data sets:  $z-L_{\text{iso}}$  (no luminosity evolution, red open circles),  $z-L'$  ( $\delta_L = 1.7$ , red filled circles),  $z-E_{\text{iso}}$  (no energy evolution, green open squares), and  $z-E'$  ( $\delta_E = 1.1$ , green filled squares). The gray points show the SFR data from Hopkins (2004), Bouwens et al. (2011), Hanish et al. (2006), and Thompson et al. (2006). The black solid line denotes the SFR approximation from Li (2008). The GRBFR points have been shifted arbitrarily to match the SFR at  $(1+z) \sim 3.5$ .

the two KW Type I GRBs with available collimation data lie above 90% PI for the Type II GRB  $E_{p,i,z} - E_\gamma$  relation and, simultaneously, within the 68% PI for the  $E_{p,z} - L_\gamma$  relation (Figure 13, lower panels).

We also calculated the collimation-corrected energetics for the ultraluminous KW GRB 110918A using  $t_{\text{jet}} = 0.2 \pm 0.13$  days estimated by Frederiks et al. (2013) from an extrapolation of early  $\gamma$ -ray/late X-ray afterglow data. As can be seen in Figure 13, the implied  $E_\gamma \approx 1.1 \times 10^{51}$  erg and  $L_\gamma \approx 1.9 \times 10^{51}$  erg s $^{-1}$  nicely agree with both hardness–intensity relations for our “reliable  $t_{\text{jet}}$ ” GRB sample. This supports the correctness of the

$t_{\text{jet}}$  estimate and favors the conclusion of Frederiks et al. (2013) that a tight collimation of the jet ( $\theta_{\text{jet}} \sim 1^\circ.6$ ) must have been a key ingredient to produce this unusually bright burst.

## 6. Summary and Conclusions

We have presented the results of a systematic study of 150 GRBs with reliable redshift estimates detected in the triggered mode of the *Konus-Wind* experiment. The sample covers the period from 1997 February to 2016 June and represents the largest set of cosmological GRBs to date over a broad energy band. Among these GRBs, 12 bursts (or 8%) belong to the Type I (merger origin, short/hard) GRB population and the others are Type II (collapsar origin, long/soft) bursts.

From the temporal and spectral analyses of the sample, we provide the burst durations  $T_{100}$ ,  $T_{90}$ , and  $T_{50}$ , the spectral lags, and spectral fits with CPL and Band model functions. From the BEST spectral models, we calculated the 10 keV–10 MeV energy fluences and the peak energy fluxes on three timescales, including the GRB rest-frame 64 ms scale. Based on the GRB redshifts, which span the range  $0.1 \leq z \leq 5$ , we estimated the rest-frame, isotropic-equivalent energies ( $E_{\text{iso}}$ ) and peak luminosities ( $L_{\text{iso}}$ ). For 32 GRBs with reasonably constrained jet breaks we provide the collimation-corrected values of the energetics.

We analyzed the influence of instrumental selection effects on the GRB parameter distributions and found that the regions above the limits, corresponding to the bolometric fluence  $S_{\text{lim}} \sim 3\text{--}4 \times 10^{-6}$  erg cm $^{-2}$  (in the  $E_{\text{iso}}-z$  plane) and bolometric peak energy flux  $F_{\text{lim}} \sim 1\text{--}2 \times 10^{-6}$  erg cm $^{-2}$  s $^{-1}$  (in the  $L_{\text{iso}}-z$  plane) may be considered free from selection biases. For the bursts in our sample we calculated the KW GRB detection horizon,  $z_{\text{max}}$ , which extends to  $z \sim 16.6$ , stressing the importance of GRBs as probes of the early universe. Among the KW short/hard GRBs the highest  $z_{\text{max}}$  is  $\approx 5.3$ .



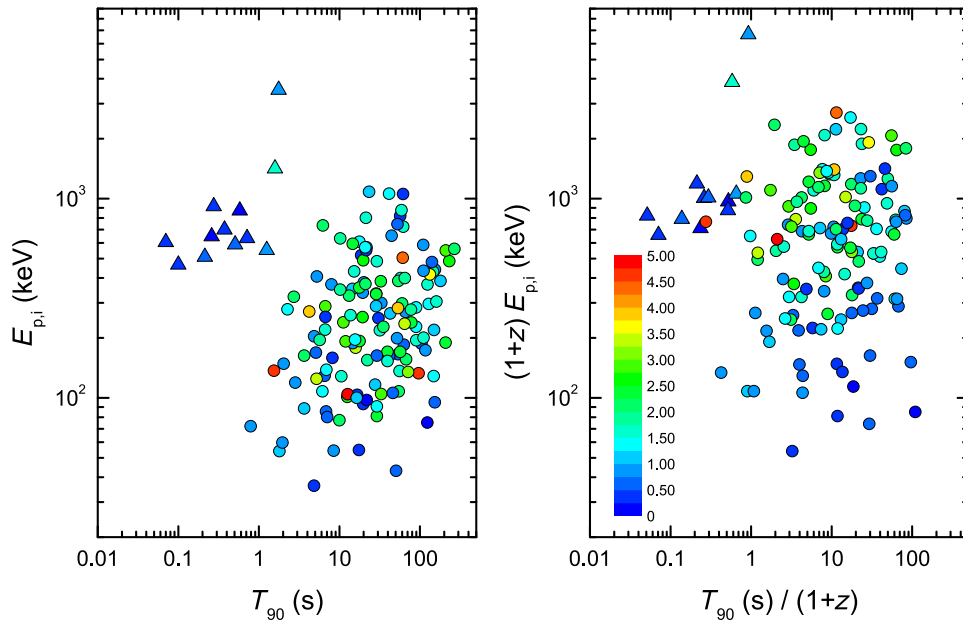


**Figure 12.**  $E_{p,i}$ – $T_{90}$  diagram in the observer (left panel) and rest (right panel) frames. The color of each data point (Type I: triangles, Type II: circles) represents the burst redshift.

Accounting for the instrumental biases and using the non-parametric methods of Lynden-Bell (1971) and EP, we estimated the GRB luminosity evolution, luminosity and isotropic-energy functions, and the evolution of the GRB formation rate. The derived luminosity evolution and isotropic energy evolution indices  $\delta_L \sim 1.7$  and  $\delta_E \sim 1.1$  are more shallow than those reported in previous studies, albeit within errors. The shape of the derived LF is best described by the broken PL function with low- and high-luminosity slopes  $\sim -0.5$  and  $\sim -1$ , respectively. The EF is better described by the exponentially cutoff PL with the PL index  $\sim -0.3$  and a cutoff isotropic energy of  $\sim (2-4) \times 10^{54}$  erg. The derived GRBFR features an excess over the SFR at  $z < 1$  and nearly traces the SFR at higher redshifts.

We considered the behavior of the rest-frame GRB parameters in the hardness–duration and hardness–intensity planes, and confirmed the “Amati” and “Yonetoku” relations for Type II GRBs. We found that the correction for the jet collimation does not improve these correlations for the KW sample. Using the KW sample, we confirm a finding of Heussaff et al. (2013) that the lower right boundary of the Amati correlation (the lack of luminous soft GRBs) is an intrinsic GRB property, while the top left boundary may be due to selection effects. This conclusion may also be extended to the Yonetoku correlation.

Plots of the GRB light curves and spectral fits can be found at the Ioffe Web site.<sup>11</sup> We hope this catalog will encourage further investigations of GRB physical properties and will contribute to other related studies.

The authors are grateful to the anonymous referee for careful reading and constructive comments that improved the manuscript. We thank Maria Giovanna Dainotti for a stimulating discussion and Vahé Petrosian for helpful comments. This work was supported by RSF (grant 17-12-01378). We

acknowledge the use of the public data from the *Swift* data archive<sup>12</sup> and the use of the data from the Gamma-Ray Burst Online Index (“GRBOX”).<sup>13</sup>

*Facility:* Wind(Konus).

## Appendix Non-parametric Statistical Techniques for a Truncated Data Sample

Here, we describe the details of the the non-parametric statistical techniques used to obtain the unbiased parameter distributions for a sample subject to selection effects in the  $z$ – $L_{\text{iso}}$  plane implying that the same methodology can be applied to the  $z$ – $E_{\text{iso}}$  plane.

The  $z$ – $L_{\text{iso}}$  sample suffers from a selection effect due to the detection limit of the instrument (see Section 5.3 for details), which results in the data truncation seen in Figure 8. Although it is a common practice to estimate the trigger sensitivity as a “characteristic” energy flux that could trigger a detector, the trigger threshold flux can actually depend on some parameters, e.g., the burst spectral shape, the background count rate, the incident angle, and the calibration; the  $k$ -corrected flux also depends on the redshift. Therefore, while deriving LF and GRBFR from the KW data we used the individual  $k$ -corrected trigger threshold fluxes  $F_{\text{lim}}$  (see Section 5.3) as a proxy for the instrumental selection effect. The results obtained using a “monolithic” truncation curve, however, are very similar to those obtained with the first method.

The parent distributions can be obtained from the biased  $z$ – $L_{\text{iso}}$  sample using the non-parametric Lynden-Bell  $C$ -techniques (Lynden-Bell 1971) further advanced by Efron & Petrosian (1992). Moreover, as shown by Petrosian (1992), all non-parametric methods for determining the underlying distributions reduce to the Lynden-Bell (1971) method in case

<sup>11</sup> <http://www.ioffe.ru/LEA/zGRBs/triggered/>

<sup>12</sup> <http://swift.gsfc.nasa.gov>

<sup>13</sup> <http://www.astro.caltech.edu/grbox/grbox.php>

**Table 8**  
Hardness–Intensity Correlations

Correlation	$N$	$\rho_S$	$P_{\rho_S}$	$a$	$b$	$a_{\sigma_{\text{int}}}$	$b_{\sigma_{\text{int}}}$	$\sigma_{\text{int}}$
Type I GRBs								
$E_{p,i}$ versus $S$	12	0.74	$5.8 \times 10^{-3}$	$0.408 \pm 0.043$	$4.98 \pm 0.22$	$0.496 \pm 0.117$	$5.52 \pm 0.62$	0.135
$E_{p,i,z}$ versus $E_{\text{iso}}$	12	0.83	$9.5 \times 10^{-4}$	$0.364 \pm 0.030$	$-15.70 \pm 1.53$	$0.266 \pm 0.068$	$-10.61 \pm 3.47$	0.181
$E_{p,p}$ versus $F_{\text{peak}}$	12	0.54	$7.1 \times 10^{-2}$	$0.340 \pm 0.045$	$4.39 \pm 0.19$	$0.349 \pm 0.161$	$4.52 \pm 0.74$	0.188
$E_{p,p,z}$ versus $L_{\text{iso}}$	12	0.67	$1.7 \times 10^{-2}$	$0.396 \pm 0.034$	$-17.68 \pm 1.78$	$0.243 \pm 0.078$	$-9.61 \pm 4.07$	0.200
Type II GRBs								
$E_{p,i}$ versus $S$	137	0.59	$3.7 \times 10^{-14}$	$0.418 \pm 0.002$	$4.06 \pm 0.01$	$0.295 \pm 0.031$	$3.66 \pm 0.14$	0.227
$E_{p,i,z}$ versus $E_{\text{iso}}$	137	0.70	$1.4 \times 10^{-21}$	$0.469 \pm 0.003$	$-22.35 \pm 0.14$	$0.338 \pm 0.026$	$-15.27 \pm 1.37$	0.229
$E_{p,p}$ versus $F_{\text{peak}}$	136	0.58	$2.2 \times 10^{-13}$	$0.453 \pm 0.004$	$4.68 \pm 0.02$	$0.363 \pm 0.041$	$4.31 \pm 0.21$	0.253
$E_{p,p,z}$ versus $L_{\text{iso}}$	136	0.73	$1.6 \times 10^{-23}$	$0.494 \pm 0.005$	$-23.32 \pm 0.26$	$0.347 \pm 0.029$	$-15.52 \pm 1.51$	0.251
Type II GRBs with $t_{\text{jet}}$ estimates								
$E_{p,i,z}$ versus $E_{\text{iso}}$	30	0.82	$4.1 \times 10^{-08}$	$0.536 \pm 0.004$	$-27.34 \pm 0.21$	$0.418 \pm 0.053$	$-19.62 \pm 2.82$	0.233
$E_{p,i,z}$ versus $E_{\gamma}$	30	0.76	$1.1 \times 10^{-06}$	$0.604 \pm 0.008$	$-27.93 \pm 0.42$	$0.499 \pm 0.077$	$-22.69 \pm 3.90$	0.266
$E_{p,p,z}$ versus $L_{\text{iso}}$	30	0.75	$1.5 \times 10^{-06}$	$0.529 \pm 0.008$	$-25.12 \pm 0.43$	$0.373 \pm 0.063$	$-16.91 \pm 3.30$	0.282
$E_{p,p,z}$ versus $L_{\gamma}$	30	0.61	$3.1 \times 10^{-04}$	$0.731 \pm 0.016$	$-33.87 \pm 0.78$	$0.376 \pm 0.097$	$-16.14 \pm 4.86$	0.343

**Note.**  $N$  is the number of bursts in the fit sample,  $\rho_S$  is the Spearman correlation coefficient,  $P_{\rho_S}$  is the corresponding chance probability,  $a$  ( $a_{\sigma_{\text{int}}}$ ) and  $b$  ( $b_{\sigma_{\text{int}}}$ ) are the slope and the intercept for the fits without (with) intrinsic scatter  $\sigma_{\text{int}}$ .

of a one-sided truncation. Initially developed for a truncated QSO sample, this procedure was first applied to the truncated GRB data by Lloyd-Ronning et al. (2002).

Since the Lynden-Bell  $C^-$  approach is applicable only if the luminosity and redshift distributions are independent, the dependence of  $L$  on  $z$  should be tested and rejected (if present). For this purpose one can use the methodology developed by Efron & Petrosian (1992). The EP method uses a modified version of the Kendall rank correlation coefficient (the Kendall  $\tau$  statistic) to test the independence of variables in truncated data. Instead of calculating the ranks of each data points among all observed objects, which is normally done for untruncated data, the rank of each data point is determined among its “associated set” which include all objects that could have been observed given the observational limits.

Consider a set of observables  $L_i$  and  $z_i$ , where  $i$  is the burst index. For each burst from the sample we construct an associated set of

$$J_i = \{j | L_j > L_i, L_i > L_{\text{lim},j}\},$$

where  $L_i$  is the  $i$ th GRB luminosity, and  $L_{\text{lim},j}$  is the minimum observable luminosity at  $z_j$ . Another commonly used definition of the associated set is

$$J_i = \{j | L_j > L_i, z_j < z_{\text{lim},i}\},$$

where  $z_{\text{lim},i}$  is the maximum redshift at which a GRB with luminosity  $L_i$  can be observed, and produces the same subsample of bursts as the foregoing definition if the truncation effect is a monotonic function. An example of the associated set for the  $i$ th burst is shown in Figure 15.

Let  $N_i$  be the number of bursts in the  $i$ th associated set (that is the same as  $C^-$  in Lynden-Bell 1971) and  $R_i$  the number of events that have redshift  $z_j$  less than  $z_i$  (that is an analog of the  $i$ th burst rank in the associated set):

$$N_i = \text{Number}\{J_i\},$$

$$R_i = \text{Number}\{j \in J_i: z_j < z_i\}.$$

Then the degree of correlation between  $L$  and  $z$  can be estimated via the test statistic  $\tau$  parametrized as

$$\tau = \frac{\sum_i (R_i - E_i)}{\sqrt{\sum_i V_i}},$$

where  $E_i = (N_i + 1)/2$  is the expected mean, and  $V_i = (N_i^2 - 1)/12$  is the variance of the uniform distribution. In the non-truncated case, this  $\tau$  statistic is equivalent to the Kendall’s non-parametric correlation coefficient. If  $z_i$  and  $L_i$  are independent of each other, then  $R_i$  is uniformly distributed between 1 and  $N_i$ , therefore the samples  $R_i \leq E_i$  and  $R_i \geq E_i$  should be nearly equal, and the  $\tau$  statistic will be close to 0. Since the  $\tau$  statistic is normalized by the square root of variance, the correlation coefficient between  $z$  and  $L$  is measured in units of the standard deviation.

Next, the index of the luminosity evolution  $\delta$  should be varied to adjust the test statistic to  $\tau(\delta) = 0$  for the luminosity  $L' = L/(1 + z)^\delta$  and thus removing the effect of luminosity evolution. The  $1\sigma$  confidence interval on  $\delta$  is obtained when  $\tau = \pm 1$  (Figure 14, left panel) and the luminosity evolution is rejected at the  $\tau_0 \equiv \tau(\delta = 0)$  level. In case the “monolithic” truncation curve is used, the resulting evolution index  $\delta$  is strongly dependent on the limiting flux (or fluence). We investigated the dependency of the luminosity and energy evolution indices  $\delta_L$  and  $\delta_E$  on the corresponding truncation limits  $F_{\text{lim}}$  and  $S_{\text{lim}}$  for the KW sample (Figure 14, right panel) and determined the limits  $F_{\text{lim}} \gtrsim 2 \times 10^{-6} \text{ erg cm}^{-2} \text{ s}^{-1}$  and  $S_{\text{lim}} \gtrsim 4.3 \times 10^{-6} \text{ erg cm}^{-2}$  above which  $\delta_L$  and  $\delta_E$  do not vary much with the truncation limit change and fluctuate around the “settled” values  $\delta_L \sim 1.7$  and  $\delta_E \sim 1.1$ . Interestingly, a similar value of  $\delta_L$  ( $\sim 1.7$ ) is obtained when the individual truncation limits are used for each burst.

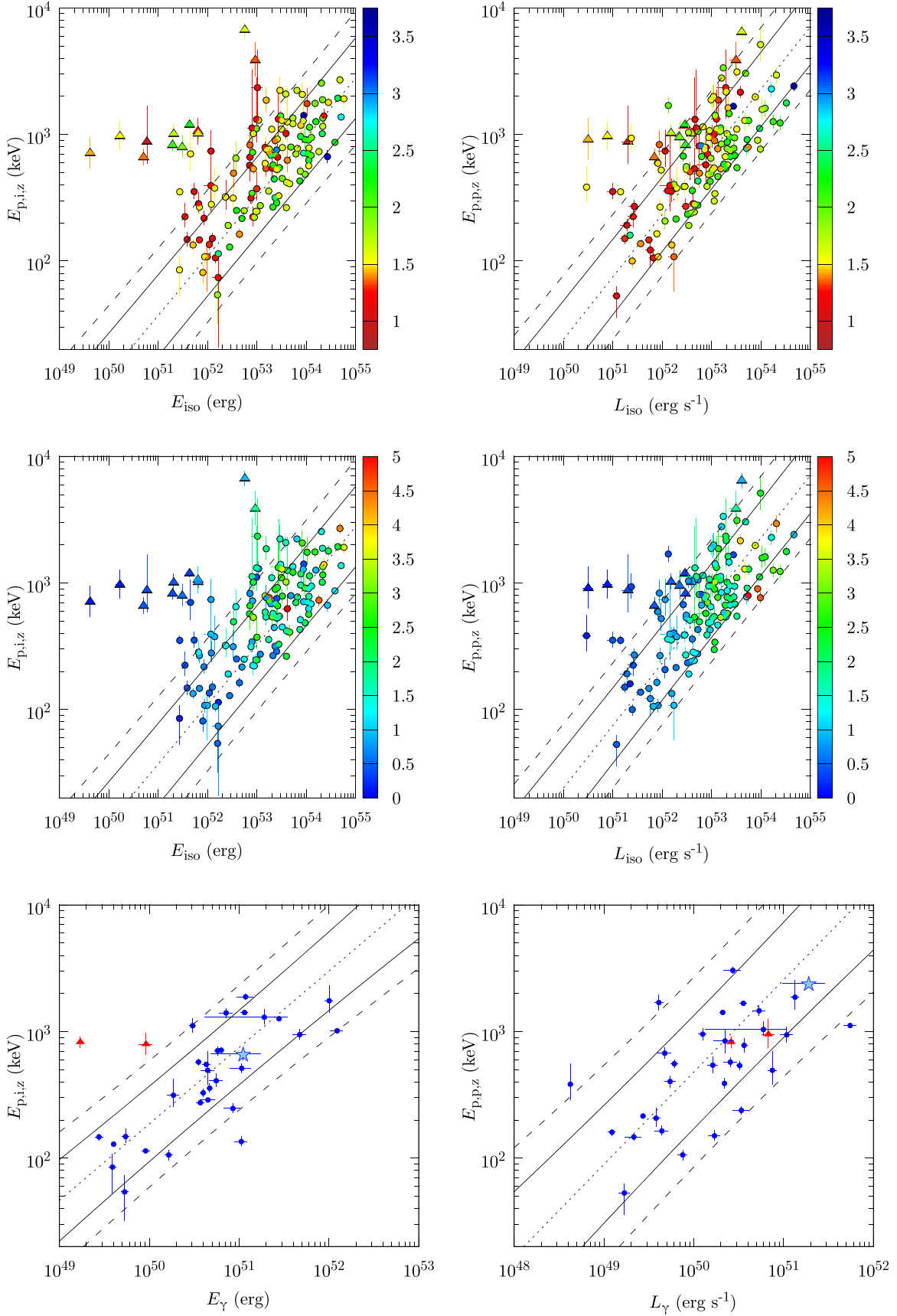


**Figure 13.** Rest-frame energetics in the  $E_{\text{iso}} - E_{p,i,z}$  (left) and  $L_{\text{iso}} - E_{p,p,z}$  (right) planes. The color of each data point (Type I: triangles, Type II: circles) represents the log of the burst’s trigger significance (upper panels) and the GRB redshift (middle panels). The “Amati” and “Yonetoku” relations calculated without internal scattering for Type II GRBs are plotted with dotted lines; the solid and dashed lines show their 68% and 90% PI’s, respectively. The lower panels present these relations for collimation-corrected energetics where the ultraluminous GRB 110918A is shown with the star.

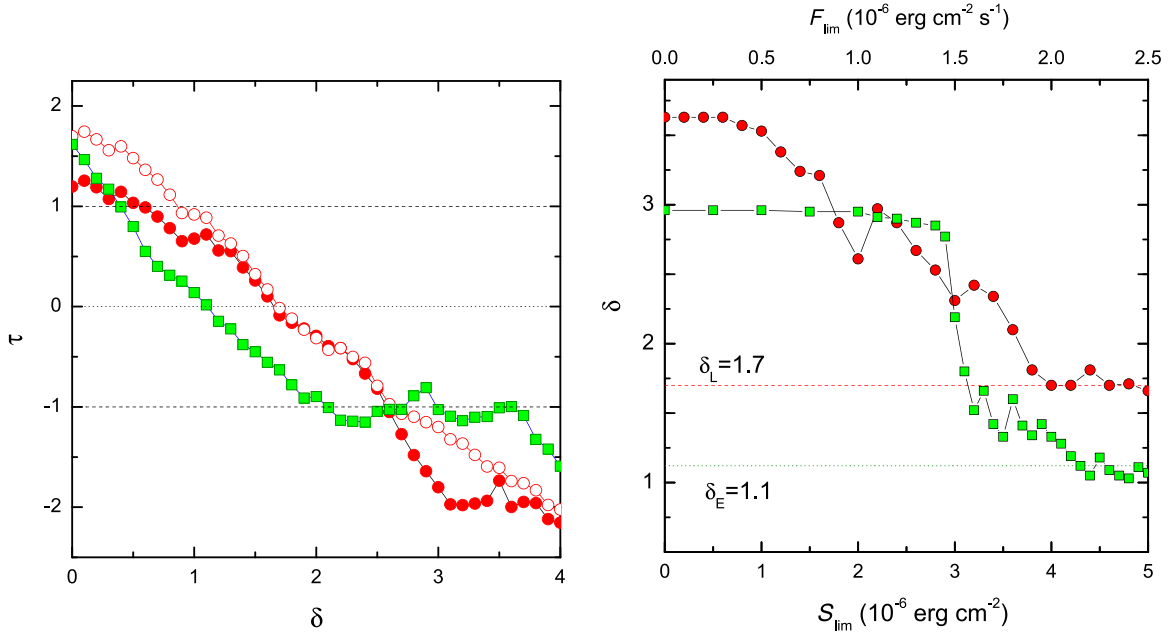


**Figure 14.** Left: modified Kendall statistic  $\tau$  vs. luminosity and isotropic-energy evolution indices  $\delta_L$  (per-burst truncation flux  $F_{\text{lim}}$ , red open circles; monolithic  $F_{\text{lim}} = 2 \times 10^{-6} \text{ erg cm}^{-2} \text{ s}^{-1}$ , red filled circles) and  $\delta_E$  (green squares, monolithic  $S_{\text{lim}} = 4.3 \times 10^{-6} \text{ erg cm}^{-2}$ ). The values of  $\delta$  for which  $\tau = 0$  and  $\tau = \pm 1$  give the best value and one sigma range for independence. Right: dependency of the best values of  $\delta_L$  and  $\delta_E$  (red circles and green squares, respectively) on the monolithic truncation limits  $F_{\text{lim}}$  and  $S_{\text{lim}}$ . The dashed and dotted lines denote the “settled” values of  $\delta_L$  and  $\delta_E$ , which correspond to  $F_{\text{lim}} \gtrsim 2 \times 10^{-6} \text{ erg cm}^{-2} \text{ s}^{-1}$  and  $S_{\text{lim}} \gtrsim 4.3 \times 10^{-6} \text{ erg cm}^{-2}$ , respectively.

Once obtained, the luminosity evolution index  $\delta_L$ , the observed luminosity  $L_{\text{iso}}$  can be converted into the local (non-evolving) luminosity space  $L' = L_{\text{iso}} / (1 + z)^{\delta_L}$ . Then, following Lynden-Bell (1971), the local cumulative LF  $\psi(L')$  can be non-parametrically derived as a function of univariate  $L'$ :

$$\ln \psi(L'_i) = \sum_{j=2}^i \ln \left( 1 + \frac{1}{N'_j} \right),$$

where  $N'_j$  is the number of points in the  $i$ th associated set for the local luminosities.

To estimate the cosmic GRBFR from the  $z$ - $L'$  sample, we produce a cumulative number distribution  $\psi(z)$ . First, we generate an associated set

$$J'_i = \{j | z_j < z_i, L_j > L_{\text{lim},i}, L_i > L_{\text{lim},j}\}$$

with  $M_i$  points in each associated set (see Figure 15 for an example of an associated set obtained for a truncation curve). The condition  $L_j > L_{\text{lim},i}$  can be expressed as  $z_{\text{lim},j} > z_i$ , but the  $z_{\text{lim}}$  estimation is complicated in case of a non-analytic truncation boundary. In the case where we used a set of threshold luminosities instead of a monotonic truncation curve, we applied an additional criterion of  $L_i > L_{\text{lim},j}$  to ensure that all the bursts of the associated set are not being subject to selection effect. Then we calculate the cumulative function

$$\ln \psi(z_i) = \sum_{j=2}^i \ln \left( 1 + \frac{1}{M_j} \right).$$

Since the differential form of the GRBFR is more useful for comparison with the SFR, we convert  $\psi(z_i)$  into a

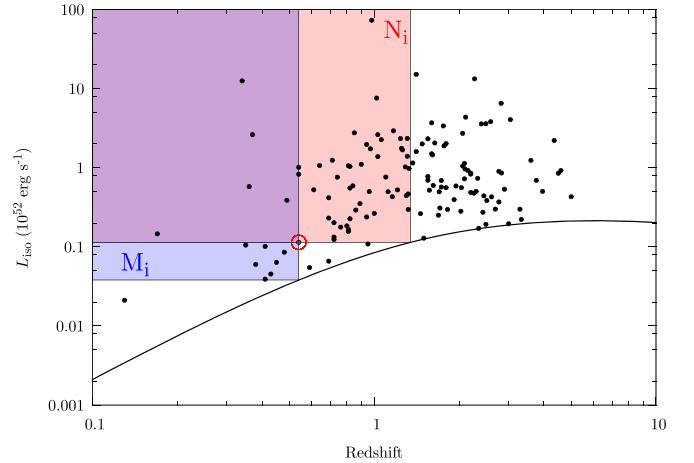


**Figure 15.** Example of the associated set for the non-evolving luminosity sample. The line represents the truncation limit corrected for the  $L_{\text{iso}}$  evolution. The “ $N_i$ ” and “ $M_i$ ” denote the LF and GRBFR associated sets for the  $i$ th burst, correspondingly. See the text for details.

differential form:

$$\rho(z) = \frac{d\psi}{dz} (1 + z) \left( \frac{dV(z)}{dz} \right)^{-1}$$

where the additional factor  $(1 + z)$  comes from the cosmological time dilation, required when measuring a rate, and  $dV(z)/dz$  is the differential comoving volume:

$$\frac{dV(z)}{dz} = \frac{4\pi D_H D_M^2}{E(z)},$$

where  $D_M$  is the transverse comoving distance,  $D_H = c/H_0$  is the Hubble distance, and  $E(z) = \sqrt{\Omega_M(1 + z)^3 + \Omega_\Lambda}$  is the normalized Hubble parameter.



## ORCID iDs

A. Tsvetkova  <https://orcid.org/0000-0003-0292-6221>  
 D. Frederiks  <https://orcid.org/0000-0002-1153-6340>  
 A. Lysenko  <https://orcid.org/0000-0002-3942-8341>  
 D. Svinkin  <https://orcid.org/0000-0002-2208-2196>  
 M. Ulanov  <https://orcid.org/0000-0002-0076-5228>  
 K. Hurley  <https://orcid.org/0000-0003-3315-1975>

## References

- Abdo, A. A., Ackermann, M., Arimoto, M., et al. 2009, *Sci*, **323**, 1688  
 Ackermann, M., Ajello, M., Asano, K., et al. 2013, *ApJS*, **209**, 11  
 Agostinelli, S., Allison, J., Amako, K., et al. 2003, *NIMPA*, **506**, 250  
 Amati, L., Frontera, F., Tavani, M., et al. 2002, *A&A*, **390**, 81  
 Andersen, M. I., Hjorth, J., Pedersen, H., et al. 2000, *A&A*, **364**, L54  
 Aptekar, R. L., Frederiks, D. D., Golenetskii, S. V., et al. 1995, *SSRv*, **71**, 265  
 Arnaud, K. A. 1996, in ASP Conf. Ser. 101, *Astronomical Data Analysis Software and Systems V*, ed. G. H. Jacoby & J. Barnes (San Francisco, CA: ASP), 17  
 Atteia, J.-L. 1997, *A&A*, **328**, L21  
 Atteia, J.-L. 2003, *A&A*, **407**, L1  
 Atteia, J.-L., Heussaff, V., Dezalay, J.-P., et al. 2017, *ApJ*, **837**, 119  
 Band, D., Matteson, J., Ford, L., et al. 1993, *ApJ*, **413**, 281  
 Band, D. L. 1997, *ApJ*, **486**, 928  
 Band, D. L. 2003, *ApJ*, **588**, 945  
 Barth, A. J., Sari, R., Cohen, M. H., et al. 2003, *ApJL*, **584**, L47  
 Berger, E., & Becker, G. 2005, *GCN*, **3520**  
 Berger, E., Fox, D. B., Price, P. A., et al. 2007a, *ApJ*, **664**, 1000  
 Berger, E., Kulkarni, S. R., Fox, D. B., et al. 2005, *ApJ*, **634**, 501  
 Berger, E., Morrell, N., & Roth, M. 2007b, *GCN*, **7154**  
 Berger, E., & Rauch, M. 2008, *GCN*, **8542**  
 Berger, E., Sari, R., Frail, D. A., et al. 2000, *ApJ*, **545**, 56  
 Berger, E., Zauderer, B. A., Levan, A., et al. 2013, *ApJ*, **765**, 121  
 Björnsson, G., Hjorth, J., Jakobsson, P., Christensen, L., & Holland, S. 2001, *ApJ*, **552**, L121  
 Blinnikov, S. I., Novikov, I. D., Perevodchikova, T. V., & Polnarev, A. G. 1984, *SvAL*, **10**, 177  
 Bloom, J. S., Berger, E., Kulkarni, S. R., Djorgovski, S. G., & Frail, D. A. 2003a, *AJ*, **125**, 999  
 Bloom, J. S., Djorgovski, S. G., & Kulkarni, S. R. 2001a, *ApJ*, **554**, 678  
 Bloom, J. S., Frail, D. A., & Sari, R. 2001b, *AJ*, **121**, 2879  
 Bloom, J. S., Morrell, N., & Mohanty, S. 2003b, *GCN*, **2212**  
 Blustin, A. J., Band, D., Barthelmy, S., et al. 2006, *ApJ*, **637**, 901  
 Bouwens, R. J., Illingworth, G. D., Labbe, I., et al. 2011, *Natur*, **469**, 504  
 Cano, Z., Bersier, D., Guidorzi, C., et al. 2011, *MNRAS*, **413**, 669  
 Castro, S., Djorgovski, S. G., Kulkarni, S. R., et al. 2001, *GCN*, **999**  
 Castro, S. M., Diercks, A., Djorgovski, S. G., et al. 2000a, *GCN*, **605**  
 Castro, S. M., Djorgovski, S. G., Kulkarni, S. R., et al. 2000b, *GCN*, **851**  
 Castro-Tirado, A. J., Fatkhullin, T. A., Moskvitin, A. S., et al. 2016, *GCN*, **19632**  
 Castro-Tirado, A. J., Sanchez-Ramirez, R., Lombardi, G., & Rivero, M. A. 2015, *GCN*, **17758**  
 Cenko, S. B., Bloom, J. S., Morgan, A. N., & Perley, D. A. 2009a, *GCN*, **9053**  
 Cenko, S. B., Bloom, J. S., Perley, D. A., et al. 2010, *GCN*, **10389**  
 Cenko, S. B., Fox, D. B., Penprase, B. E., et al. 2008, *ApJ*, **677**, 441  
 Cenko, S. B., Frail, D. A., Harrison, F. A., et al. 2011, *ApJ*, **732**, 29  
 Cenko, S. B., Kasliwal, M., Harrison, F. A., et al. 2006, *ApJL*, **652**, 490  
 Cenko, S. B., Perley, D. A., Jankkarinen, V., et al. 2009b, *GCN*, **9518**  
 Chandra, P., Cenko, S. B., Frail, D. A., et al. 2008, *ApJ*, **683**, 924  
 Chornock, R., & Berger, E. 2009, *GCN*, **10176**  
 Chornock, R., & Berger, E. 2011a, *GCN*, **11544**  
 Chornock, R., & Berger, E. 2011b, *GCN*, **11518**  
 Chornock, R., Perley, D., Cenko, S. B., & Bloom, J. S. 2009a, *GCN*, **9028**  
 Chornock, R., Perley, D. A., Cenko, S. B., & Bloom, J. S. 2009b, *GCN*, **9243**  
 Cohen, E., & Piran, T. 1997, *ApJL*, **488**, L7  
 Coward, D. M., Howell, E. J., Branchesi, M., et al. 2013, *MNRAS*, **432**, 2141  
 Crew, G., Villaseñor, J., Vanderspek, R., et al. 2002, *GCN*, **1734**  
 Cucchiara, A. 2014, *GCN*, **15652**  
 Cucchiara, A., & Cenko, S. B. 2013, *GCN*, **14687**  
 Cucchiara, A., & Fox, D. B. 2010, *GCN*, **10606**  
 Cucchiara, A., Fox, D. B., Cenko, S. B., & Berger, E. 2008, *GCN*, **8713**  
 Cucchiara, A., Fox, D. B., Cenko, S. B., Tanvir, N., & Berger, E. 2009, *GCN*, **10031**  
 Cucchiara, A., Levan, A. J., Fox, D. B., et al. 2011, *ApJ*, **736**, 7  
 Cucchiara, A., & Perley, D. 2013, *GCN*, **15144**  
 Cucchiara, A., & Prochaska, J. X. 2012, *GCN*, **12865**  
 Dainotti, M. G., & Del Vecchio, R. 2017, *NewAR*, **77**, 23  
 de Ugarte Postigo, A., Campana, S., Thoene, C. C., et al. 2013a, *A&A*, **557**, 18D  
 de Ugarte Postigo, A., Castro-Tirado, A. J., & Gorosabel, J. 2011a, *GCN*, **11978**  
 de Ugarte Postigo, A., Castro-Tirado, A. J., Guziy, S., et al. 2006, *ApJL*, **648**, L83  
 de Ugarte Postigo, A., Castro-Tirado, A. J., Tello, J. C., Cabrera Lavers, A., & Reverte, D. 2011b, *GCN*, **11993**  
 de Ugarte Postigo, A., Fynbo, J. P. U., Thoene, C., et al. 2015a, *GCN*, **17583**  
 de Ugarte Postigo, A., Gorosabel, J., Castro-Tirado, A. J., & Thoene, C. C. 2011c, *GCN*, **12375**  
 de Ugarte Postigo, A., Gorosabel, J., Fynbo, J. P. U., Wiersema, K., & Tanvir, N. 2009a, *GCN*, **9771**  
 de Ugarte Postigo, A., Gorosabel, J., Xu, D., et al. 2014a, *GCN*, **16310**  
 de Ugarte Postigo, A., Jakobsson, P., Malesani, D., et al. 2009b, *GCN*, **8766**  
 de Ugarte Postigo, A., Malesani, D., & Xu, D. 2015b, *GCN*, **18426**  
 de Ugarte Postigo, A., Thoene, C. C., Gorosabel, J., et al. 2013b, *GCN*, **15470**  
 de Ugarte Postigo, A., Thoene, C. C., Gorosabel, J., et al. 2014b, *GCN*, **17198**  
 de Ugarte Postigo, A., Thoene, C. C., & Sanchez-Ramirez, R. 2016, *GCN*, **18966**  
 de Ugarte Postigo, A., Thöne, C. C., Rowlinson, A., et al. 2014c, *A&A*, **563**, A62  
 de Ugarte Postigo, A., Xu, D., Malesani, D., et al. 2013c, *GCN*, **15187**  
 de Ugarte Postigo, A., Xu, D., Malesani, D., & Tanvir, N. R. 2015c, *GCN*, **17822**  
 D'Elia, V., Goldoni, P., Xu, D., et al. 2012, *GCN*, **13494**  
 D'Elia, V., Kruehler, T., Wiersema, K., et al. 2015, *GCN*, **18187**  
 Della Valle, M., Benetti, S., Malesani, D., et al. 2003, *GCN*, **1809**  
 Della Valle, M., Chincarini, G., Panagia, N., et al. 2006, *Natur*, **444**, 1050  
 Diaferio, A., Ostorero, L., & Cardone, V. 2011, *JCAP*, **10**, 8  
 Dirirsa, F., Racusin, J., McEnery, J., & Desiante, R. 2016, *GCN*, **19580**  
 Djorgovski, S. G., Dierks, A., Bloom, J. S., et al. 1999, *GCN*, **481**  
 Djorgovski, S. G., Frail, D. A., Kulkarni, S. R., et al. 2001, *ApJ*, **562**, 654  
 Efron, B., & Petrosian, V. 1992, *ApJ*, **399**, 345  
 Eichler, D., Livio, M., Piran, T., & Schramm, D. N. 1989, *Natur*, **340**, 126  
 Fenimore, E. E., Ricker, G., Atteia, J.-L., et al. 2004, *GCN*, **2735**  
 FERMIGBRST—Fermi GBM Burst Catalog. 2016, NASA Goddard Space Flight Center, <http://heasarc.gsfc.nasa.gov/W3Browse/fermi/fermigbrst.html>  
 Fermi-LAT Collaboration 2013, arXiv:1303.2908  
 Filgas, R., Greiner, J., Schady, P., et al. 2011, *A&A*, **535**, A57  
 Flores, H., Covino, S., Xu, D., et al. 2013, *GCN*, **14491**  
 Foley, R. J., Chen, H.-W., Bloom, J., & Prochaska, J. X. 2005, *GCN*, **3483**  
 Foley, S., Watson, D., Gorosabel, J., et al. 2006, *A&A*, **447**, 891  
 Fong, W., Berger, E., Metzger, B. D., et al. 2014, *ApJ*, **780**, 118  
 Fox, A. J., Ledoux, C., Vreeswijk, P. M., Smette, A., & Jaunsen, A. O. 2008, *A&A*, **491**, 189  
 Frail, D. A., Kulkarni, S. R., Sari, R., et al. 2001, *ApJL*, **562**, L55  
 Frederiks, D., Golenetskii, S., Aptekar, R., et al. 2016, *GCN*, **19554**  
 Frederiks, D. D., Hurley, K., Svinkin, D. S., et al. 2013, *ApJ*, **779**, 151  
 Friedman, A. S., & Bloom, J. S. 2005, *ApJ*, **627**, 1  
 Frontera, F., Guidorzi, C., Montanari, E., et al. 2009, *ApJS*, **180**, 192  
 Fynbo, J. P. U., Jakobsson, P., Prochaska, J. X., et al. 2009, *ApJS*, **185**, 526  
 Fynbo, J. P. U., Tanvir, N. R., Jakobsson, P., et al. 2014, *GCN*, **16217**  
 Fynbo, J. P. U., Watson, D., Thöne, C. C., et al. 2006, *Natur*, **444**, 1047  
 Galama, T. J., Reichart, D., Brown, T. M., et al. 2003, *ApJ*, **587**, 135  
 Galassi, M., Ricker, G., Atteia, J.-L., et al. 2004, *GCN*, **2770**  
 Gal-Yam, A., Berger, E., Fox, D. B., et al. 2005, *GCN*, **4156**  
 Gal-Yam, A., Fox, D. B., Price, P. A., et al. 2006, *Natur*, **444**, 1053  
 Gehrels, N., Norris, J. P., Barthelmy, S. D., et al. 2006, *Natur*, **444**, 1044  
 Ghirlanda, G., Ghisellini, G., & Lazzati, D. 2004, *ApJ*, **616**, 331  
 Ghirlanda, G., Nava, L., Ghisellini, G., & Firmani, C. 2007, *A&A*, **466**, 127  
 Ghisellini, G., Haardt, F., Campana, S., Lazzati, D., & Covino, S. 1999, *ApJ*, **517**, 168  
 Goldstein, A., Burgess, J. M., Preece, R. D., et al. 2012, *ApJS*, **199**, 19  
 Goldstein, A., Preece, R. D., Mallozzi, R. S., et al. 2013, *ApJS*, **208**, 21  
 Golenetskii, S. V., Mazets, E. P., Aptekar, R. L., & Ilinskii, V. N. 1983, *Natur*, **306**, 451  
 Gotz, D., Mereghetti, S., Bozzo, E., et al. 2016, *GCN*, **19621**  
 Graham, J. F., Fruchter, A. S., Levan, A. J., et al. 2009, *ApJ*, **698**, 1620  
 Greiner, J., Clemens, C., Krühler, T., et al. 2009, *A&A*, **498**, 89  
 Gruber, D., Goldstein, A., Weller von Ahlefeld, V., et al. 2014, *ApJS*, **211**, 12  
 Hanish, D. J., Meurer, G. R., Ferguson, H. C., et al. 2006, *ApJ*, **649**, 150

- Heussaff, V., Atteia, J.-L., & Zolnierowski, Y. 2013, *A&A*, **557**, A100
- Hjorth, J., Melandri, A., Malesani, D., Kruehler, T., & Xu, D. 2013, GCN, 14365
- Hopkins, A. M. 2004, *ApJ*, **615**, 209
- Hurley, K. 1999, GCN, 450
- Hurley, K., Cline, T., Mitrofanov, I., et al. 2007, GCN, 6024
- Hurley, K., Cline, T., & Mazets, E. 2000a, GCN, 642
- Hurley, K., Cline, T., Mazets, E., & Golenetskii, S. 2000b, GCN, 791
- Hurley, K., Goldsten, J., Golenetskii, S., et al. 2012, GCN, 13487
- Hurley, K., Golenetskii, S., Aptekar, R., et al. 2011, GCN, 12357
- Hurley, K., Mazets, E., Golenetskii, S., & Cline, T. 2000c, GCN, 801
- Hurley, K., Pal'shin, V. D., Aptekar, R. L., et al. 2013, *ApJS*, **207**, 39
- IBAS: Results, 2012, Table with all the GRBs localized with IBAS, [http://ibas.iasf-milano.inaf.it/IBAS\\_Results.html](http://ibas.iasf-milano.inaf.it/IBAS_Results.html)
- Infante, L., Garnavich, P. M., Stanek, K. Z., & Wyrzykowski, L. 2001, GCN, 1152
- Jakobsson, P., Fynbo, J. P. U., Andersen, M. I., et al. 2007, GCN, 6398
- Jakobsson, P., Fynbo, J. P. U., Ledoux, C., et al. 2006, *A&A*, **460**, L13
- Kann, D. A., Laux, U., Filgas, R., et al. 2007, GCN, 6935
- Kann, D. A., Schmidl, S., Stecklum, B., & Hoegner, C. 2011, GCN, 12010
- Kippen, R. M. 2000, GCN, 530
- Kocevski, D., & Arimoto, M. 2015, GCN, 17816
- Kouveliotou, C., Meegan, C. A., Fishman, G. J., et al. 1993, *ApJL*, **413**, L101
- Kovács, A., Bagoly, Z., Balázs, L. G., Horváth, I., & Veres, P. 2011, *AcPol*, **51**, 68
- Krimm, H. A., Yamaoka, K., Sugita, S., et al. 2009, *ApJ*, **704**, 1405
- Kruehler, T., Greiner, J., & Kann, D. A. 2013, GCN, 14500
- Kruehler, T., Xu, D., Fynbo, J. P. U., et al. 2015, GCN, 17420
- Krühler, T., Malesani, D., Fynbo, J. P. U., et al. 2015, *A&A*, **581**, A125
- Krühler, T., Malesani, D., Milvang-Jensen, B., et al. 2012, *ApJ*, **758**, 46
- Kuin, N. P. M., Landsman, W., Page, M. J., et al. 2009, *MNRAS*, **395**, L21
- Kulkarni, S. R., Djorgovski, S. G., Odewahn, S. C., et al. 1999, *Natur*, **398**, 389
- Kulkarni, S. R., Djorgovski, S. G., & Ramaprakash, A. N. O. 1998, *Natur*, **393**, 35
- Lamb, D. Q., & Reichart, D. E. 2001, in AIP Conf. Ser. 586, 20th Texas Symp. on Relativistic Astrophysics, ed. J. C. Wheeler & H. Martel (Melville, NY: AIP), 605
- Le Floch, E., Duc, P.-A., Mirabel, I. F., et al. 2002, *ApJL*, **581**, L81
- Levan, A. J., Jakobsson, P., Hurkett, C., et al. 2007, *MNRAS*, **378**, 1439
- Levesque, E. M., Kewley, L. J., Graham, J. F., & Fruchter, A. S. 2010, *ApJL*, **712**, L26
- Li, L.-X. 2008, *MNRAS*, **388**, 1487
- Li, Z.-Y., & Chevalier, R. A. 2003, *ApJ*, **589**, L69
- Lipunov, V. M., Gorosabel, J., Pruzhinskaya, M. V., et al. 2016, *MNRAS*, **455**, 712
- Lloyd-Ronning, N. M., Fryer, C. L., & Ramirez-Ruiz, E. 2002, *ApJ*, **574**, 554
- Longo, F., Bissaldi, E., Vianello, G., et al. 2016, GCN, 19413
- Lynden-Bell, D. 1971, *MNRAS*, **155**, 95
- MacFadyen, A. I., & Woosley, S. E. 1999, *ApJ*, **524**, 262
- Malesani, D., de Ugarte Postigo, A., De Pasquale, M., et al. 2016, GCN, 19708
- Malesani, D., Goldoni, P., Fynbo, J. P. U., et al. 2009, GCN, 9942
- Maselli, A., Melandri, A., Nava, L., et al. 2014, *Sci*, **343**, 48
- Masetti, N., Palazzi, E., Pian, E., et al. 2000, *A&A*, **354**, 473
- Masetti, N., Palazzi, E., Pian, E., et al. 2002, GCN, 1330
- Metzger, M. R., Djorgovski, S. G., Kulkarni, S. R., et al. 1997, *Natur*, **387**, 878
- Milne, P. A., & Cenko, S. B. 2011, GCN, 11708
- Milvang-Jensen, B., Goldoni, P., Tanvir, N. R., et al. 2010, GCN, 10876
- Nappo, F., Pescalli, A., Oganessyan, G., et al. 2017, *A&A*, **598**, A23
- Narayana Bhat, P., Meegan, C. A., von Kienlin, A., et al. 2016, *ApJS*, **223**, 28
- Narayan, R., Paczynski, B., & Piran, T. 1992, *ApJL*, **395**, L83
- Nava, L., Salvaterra, R., Ghirlanda, G., et al. 2012, *MNRAS*, **421**, 1256
- Norris, J. P., Marani, G. F., & Bonnell, J. T. 2000, *ApJ*, **534**, 248
- O'Meara, J., Chen, H.-W., & Prochaska, J. X. 2010, GCN, 11089
- Paczynski, B. 1986, *ApJL*, **308**, L43
- Paczynski, B. 1991, *AcA*, **41**, 257
- Paczynski, B. 1998, *ApJL*, **494**, L45
- Page, K. L., Willingale, R., Osborne, J. P., et al. 2007, *ApJ*, **663**, 1125
- Palazzi, E., Fugazza, D., & Piranomonte, S. 2011, GCN, 12765
- Pal'shin, V. D., Hurley, K., Svinkin, D. S., et al. 2013, *ApJS*, **207**, 38
- Perley, D. A., Cao, Y., Kasliwal, M., & Kirby, E. 2014, GCN, 16365
- Perley, D. A., & Cenko, S. B. 2015, GCN, 17616
- Perley, D. A., Cenko, S. B., Bloom, J. S., et al. 2009, *AJ*, **138**, 1690
- Perley, D. A., Hillenbrand, L., & Prochaska, J. X. 2015, GCN, 18487
- Perley, D. A., Levan, A. J., Tanvir, N. R., et al. 2013, *ApJ*, **778**, 128
- Perley, D. A., Li, W., Chornock, R., et al. 2008, *ApJ*, **688**, 470
- Perley, D. A., & McConnell, N. J. 2015, GCN, 17745
- Petrosian, V., Kitanidis, E., & Kocevski, D. 2015, *ApJ*, **806**, 44
- Petrosian, V. 1992, in Statistical Challenges in Modern Astronomy, ed. E. D. Feigelson & G. J. Babu (New York: Springer), 173
- Piranomonte, S., Vergani, S. D., Malesani, D., et al. 2011, GCN, 12164
- Piro, L., Frail, D. A., Gorosabel, J., et al. 2002, *ApJ*, **577**, 680
- Planck Collaboration, Ade, P. A. R., Aghanim, N., et al. 2014, *A&A*, **571**, A16
- Preece, R. D., Briggs, M. S., Giblin, T. W., et al. 2002, *ApJ*, **581**, 1248
- Preece, R. D., Briggs, M. S., Mallozzi, R. S., et al. 1998, *ApJL*, **506**, L23
- Press, W. H., Teukolsky, S. A., Vetterling, W. T., & Flannery, B. P. 1992, Numerical Recipes in C. The Art of Scientific Computing (Cambridge: Cambridge Univ. Press)
- Price, P. A., Berger, E., Kulkarni, S. R., et al. 2002a, *ApJ*, **573**, 85
- Price, P. A., Kulkarni, S. R., Berger, E., et al. 2002b, *ApJL*, **571**, L121
- Price, P. A., Kulkarni, S. R., Schmidt, B. P., et al. 2003, *ApJ*, **584**, 931
- Price, P. A., Roth, K., Rich, J., et al. 2004, GCN, 2791
- Prigozhin, G., Ricker, G., Atteia, J.-L., et al. 2006, GCN, 4551
- Prochaska, J. X., Sheffer, Y., Perley, D. A., et al. 2009, *ApJL*, **691**, L27
- Pugliese, V., Xu, D., Tanvir, N. R., et al. 2015, GCN, 17672
- Quimby, R., Fox, D., Hoefflich, P., Roman, B., & Wheeler, J. C. 2005, GCN, 4221
- Racusin, J. L., Karpov, S. V., Sokolowski, M., et al. 2008, *Natur*, **455**, 183
- Racusin, J. L., Zhu, S., Kocevski, D., et al. 2013, GCN, 15464
- Rapisarda, M., Costa, E., Del Monte, E., et al. 2008, GCN, 7715
- Rau, A., McBreen, S., & Kruehler, T. 2009, GCN, 9353
- Remillard, R., Wood, A., Smith, D., & Levine, A. 1997, *IAUC*, **6726**, 1
- Resmi, L., Ishwara-Chandra, C. H., Castro-Tirado, A. J., et al. 2005, *A&A*, **440**, 477
- Rhoads, J. E. 1997, *ApJL*, **487**, L1
- Rossi, A., de Ugarte Postigo, A., Ferrero, P., et al. 2008, *A&A*, **491**, L29
- Sakamoto, T., Barthelmy, S. D., Barbier, L., et al. 2008, *ApJS*, **175**, 179
- Sakamoto, T., Barthelmy, S. D., Baumgartner, W. H., et al. 2009, GCN, 10180
- Sakamoto, T., Barthelmy, S. D., Baumgartner, W. H., et al. 2011a, *ApJS*, **195**, 2
- Sakamoto, T., Pal'shin, V., Yamaoka, K., et al. 2011b, *PASJ*, **63**, 215
- Salvaterra, R., Campana, S., Vergani, S. D., et al. 2012, *ApJ*, **749**, 68
- Salvaterra, R., Della Valle, M., Campana, S., et al. 2009, *Natur*, **461**, 1258
- Sari, R., Piran, T., & Halpern, J. P. 1999, *ApJL*, **519**, L17
- Schmidt, M., Higdon, J. C., & Hueter, G. 1988, *ApJL*, **329**, L85
- Schulze, S., Klose, S., Björnsson, G., et al. 2011, *A&A*, **526**, A23
- Schulze, S., Wiersema, K., Xu, D., & Fynbo, J. P. U. 2014, GCN, 15831
- Selsing, J., Vreeswijk, P. M., Japelj, J., et al. 2016, GCN, 19274
- Singer, L. P., Kasliwal, M. M., Cenko, S. B., et al. 2015, *ApJ*, **806**, 52
- Smith, D. A. 2000, GCN, 568
- Soderberg, A. M., Berger, E., Kasliwal, M., et al. 2006, *ApJ*, **650**, 261
- Sonbas, E., Racusin, J. L., Kocevski, D., & McEnery, J. 2013, GCN, 15640
- Sparre, M., Hartoog, O. E., Krühler, T., et al. 2014, *ApJ*, **785**, 150
- Starling, R. L. C., Rol, E., van der Horst, A. J., et al. 2009, *MNRAS*, **400**, 90
- Stern, D., Perley, D. A., Reddy, N., et al. 2007, GCN, 6928
- Stratta, G., D'Avanzo, P., & Piranomonte, S. 2007, *A&A*, **474**, 827
- Svinkin, D., Golenetskii, S., Aptekar, R., et al. 2016a, GCN, 19604
- Svinkin, D. S., Frederiks, D. D., Aptekar, R. L., et al. 2016b, *ApJS*, **224**, 10
- Swift GRB Table. 2016, NASA Goddard Space Flight Center, [http://swift.gsfc.nasa.gov/docs/swift/archive/grb\\_table/](http://swift.gsfc.nasa.gov/docs/swift/archive/grb_table/)
- Table of HETE Burst Data. 2006, Massachusetts Institute of Technology, <http://space.mit.edu/HETE/Bursts/Data/>
- Tanvir, N. R., Levan, A. J., Cenko, S. B., et al. 2016, GCN, 19419
- Tanvir, N. R., Levan, A. J., Cucchiara, A., Perley, D., & Cenko, S. B. 2014, GCN, 16125
- Tanvir, N. R., Levan, A. J., Fruchter, A. S., et al. 2015, GCN, 18100
- Tanvir, N. R., Levan, A. J., & Matulonis, T. 2012a, GCN, 14009
- Tanvir, N. R., Levan, A. J., Matulonis, T., & Smith, A. B. 2013, GCN, 14567
- Tanvir, N. R., Rol, E., Levan, A. J., et al. 2010a, *ApJ*, **725**, 625
- Tanvir, N. R., Vergani, S., Hjorth, J., et al. 2010b, GCN, 11230
- Tanvir, N. R., Wiersema, K., & Levan, A. J. 2010c, GCN, 11230
- Tanvir, N. R., Wiersema, K., Levan, A. J., et al. 2012b, GCN, 13441
- Tanvir, N. R., Wiersema, K., Levan, A. J., Cenko, S. B., & Geballe, T. 2011, GCN, 12225
- Terekhov, M. M., Aptekar, R. L., Frederiks, D. D., et al. 1998, in AIP Conf. Ser. 428, Gamma-Ray Bursts, 4th Hunstville Symp., ed. C. A. Meegan, R. D. Preece, & T. M. Koshut (Melville, NY: AIP), 894
- Thoene, C. C., Goldoni, P., Covino, S., et al. 2009, GCN, 10233
- Thompson, R. I., Eisenstein, D., Fan, X., et al. 2006, *ApJ*, **647**, 787
- Tremaine, S., Gebhardt, K., Bender, R., et al. 2002, *ApJ*, **574**, 740
- Turpin, D., Heussaff, V., Dezalay, J.-P., et al. 2016, *ApJ*, **831**, 28

- Vianello, G., Dirrsa, F., Omodei, N., et al. 2016, GCN, [19553](#)
- Volnova, A. A., Pozanenko, A. S., Gorosabel, J., et al. 2014, [MNRAS](#), [442](#), [2586](#)
- Vreeswijk, P. M., Fruchter, A., Kaper, L., et al. 2001, [ApJ](#), [546](#), [672](#)
- Vreeswijk, P. M., Smette, A., Fruchter, A., et al. 2006, [A&A](#), [447](#), [145](#)
- von Kienlin, A., Meegan, C. A., Paciesas, W. S., et al. 2014, [ApJS](#), [211](#), [13](#)
- Watson, D., Fynbo, J. P. U., Ledoux, C., et al. 2006, [ApJ](#), [652](#), [1011](#)
- Waxman, E., Kulkarni, S. R., & Frail, D. A. 1998, [ApJ](#), [497](#), [288](#)
- Wiersema, K., Levan, A., Kamble, A., Tanvir, N., & Malesani, D. 2009, GCN, [9673](#)
- Wiersema, K., Starling, R. L. S., Rol, E., Vreeswijk, P., & Wijers, R. A. M. J. 2004, GCN, [2800](#)
- Wiersema, K., Tanvir, N., Levan, A., & Karjalainen, R. 2014, GCN, [16231](#)
- Woosley, S. E. 1993, [ApJ](#), [405](#), [273](#)
- Woosley, S. E., & Bloom, J. S. 2006, [ARA&A](#), [44](#), [507](#)
- Wu, S.-W., Xu, D., Zhang, F.-W., & Wei, D.-M. 2012, [MNRAS](#), [423](#), [2627](#)
- Xu, D., de Ugarte Postigo, A., Malesani, D., et al. 2013a, GCN, [14956](#)
- Xu, D., Fynbo, J. P. U., Jakobsson, P., et al. 2013b, GCN, [15407](#)
- Xu, D., Fynbo, J. P. U., Tanvir, N. R., et al. 2009, GCN, [10053](#)
- Xu, D., Malesani, D., Fynbo, J. P. U., et al. 2016, GCN, [19600](#)
- Xu, D., Malesani, D., Tanvir, N., Kruehler, T., & Fynbo, J. 2013c, GCN, [15450](#)
- Yonetoku, D., Murakami, T., Nakamura, T., et al. 2004, [ApJ](#), [609](#), [935](#)
- Yu, H., Wang, F. Y., Dai, Z. G., & Cheng, K. S. 2015, [ApJS](#), [218](#), [13](#)
- Zeh, A., Klose, S., & Kann, D. A. 2006, [ApJ](#), [637](#), [889](#)
- Zhang, B., Zhang, B.-B., Virgili, F. J., et al. 2009, [ApJ](#), [703](#), [1696](#)
- Zhang, B.-B., Zhang, B., Castro-Tirado, A. J., et al. 2016, arXiv:[1612.03089](#)